Naval Research Laboratory
Washington, DC 20375-5320

NRL/6043/MR—2023/1

Interaction of Hypersonic Vehicles with Liquid Hydrometeors

CAMILO AGUILERA

JONATHAN SOSA

EVAN HYDE

GABRIEL GOODWIN

Design and Verification Branch
Spacecraft Engineering Division

ANDREW HESS

DAVID KESSLER

Laboratory for Multiscale Reactive Flow Physics Branch
Laboratories for Computational Physics and Fluid Dynamics Division

March 8, 2023

REPORT DOCUMENTATION PAGE

Form Approved
OMB No. 0704-0188

1. REPORT DATE *(DD-MM-YYYY)* 08-03-2023	**2. REPORT TYPE** NRL Memorandum Report	**3. DATES COVERED** *(From - To)* 10/1/2019 – 9/30/2022

4. TITLE AND SUBTITLE

Interaction of Hypersonic Vehicles with Liquid Hydrometeors

5a. CONTRACT NUMBER

5b. GRANT NUMBER

5c. PROGRAM ELEMENT NUMBER

6. AUTHOR(S)

Camilo Aguilera, Jonathan Sosa, Evan Hyde, Gabriel Goodwin, Andrew Hess, and David Kessler

5d. PROJECT NUMBER

5e. TASK NUMBER

5f. WORK UNIT NUMBER

6B88

7. PERFORMING ORGANIZATION NAME(S) AND ADDRESS(ES)

Naval Research Laboratory
4555 Overlook Avenue, SW
Washington, DC 20375-5320

8. PERFORMING ORGANIZATION REPORT NUMBER

NRL/6043/MR--2023/1

9. SPONSORING / MONITORING AGENCY NAME(S) AND ADDRESS(ES)

Naval Research Laboratory
4555 Overlook Avenue, SW
Washington, DC 20375-5320

10. SPONSOR / MONITOR'S ACRONYM(S)

NRL 6.2 Base Program

11. SPONSOR / MONITOR'S REPORT NUMBER(S)

12. DISTRIBUTION / AVAILABILITY STATEMENT

DISTRIBUTION STATEMENT A: Approved for public release; distribution is unlimited.

13. SUPPLEMENTARY NOTES

14. ABSTRACT

During the terminal dive phase of a hypersonic flight trajectory, the vehicle is at risk of encountering atmospheric weather particles, including cloud droplets, ice, snow, and rain drops. These interactions could result in significant levels of erosive damage to the vehicle that could lead to mission failure. In general, the fate and transport of these liquid hydrometeors through the severe and complex aerothermal environment encountered in the shock layer between the vehicle's leading bow shock and its surface is not well understood. Much of the existing body of knowledge was generated from normal shock tube experiments, which are not fully representative of a realistic hypersonic flow field. In this report, we present an overview of the state-of-the-art in modeling hydrometeor-induced erosion and then discuss alternative approaches that have the potential to more accurately track hydrometeor demise. We show that the spread in existing models give rise to a large degree of uncertainty regarding the likelihood of liquid hydrometeor impact. We present a series of experiments and resolved two-fluid simulations that provide a more detailed picture of the trajectories and demise processes over a range of droplet sizes and operating conditions.

15. SUBJECT TERMS

16. SECURITY CLASSIFICATION OF:			**17. LIMITATION OF ABSTRACT**	**18. NUMBER OF PAGES**	**19a. NAME OF RESPONSIBLE PERSON** David Kessler
a. REPORT U	**b. ABSTRACT** U	**c. THIS PAGE** U	U	91	**19b. TELEPHONE NUMBER** *(include area code)* (202) 767-3196

Standard Form 298 (Rev. 8-98)
Prescribed by ANSI Std. Z39.18

This page intentionally left blank.

CONTENTS

FIGURES

TABLES

INTERACTION OF HYPERSONIC VEHICLES WITH LIQUID HYDROMETEORS

1. INTRODUCTION

1.1 Background

1.1.1 Clouds and Hydrometeors

About 99% of the water content in the atmosphere is contained within its lowest layer which extends from the surface to an altitude of about 8 *km* above the poles and approximately 18 *km* over the equator. [1] Condensation of water vapor in this layer known as the troposphere creates clouds which cover the planet and play a key role in atmospheric weather. Satellite imaging of clouds over the years has demonstrated that the global cloud fraction is approximately 55% over land and around 72% over the ocean with some seasonal variation. [2]. Figure 1 displays the mean spatial distribution of cloud fraction over the planet during 2019 derived from satellite observations. [3]

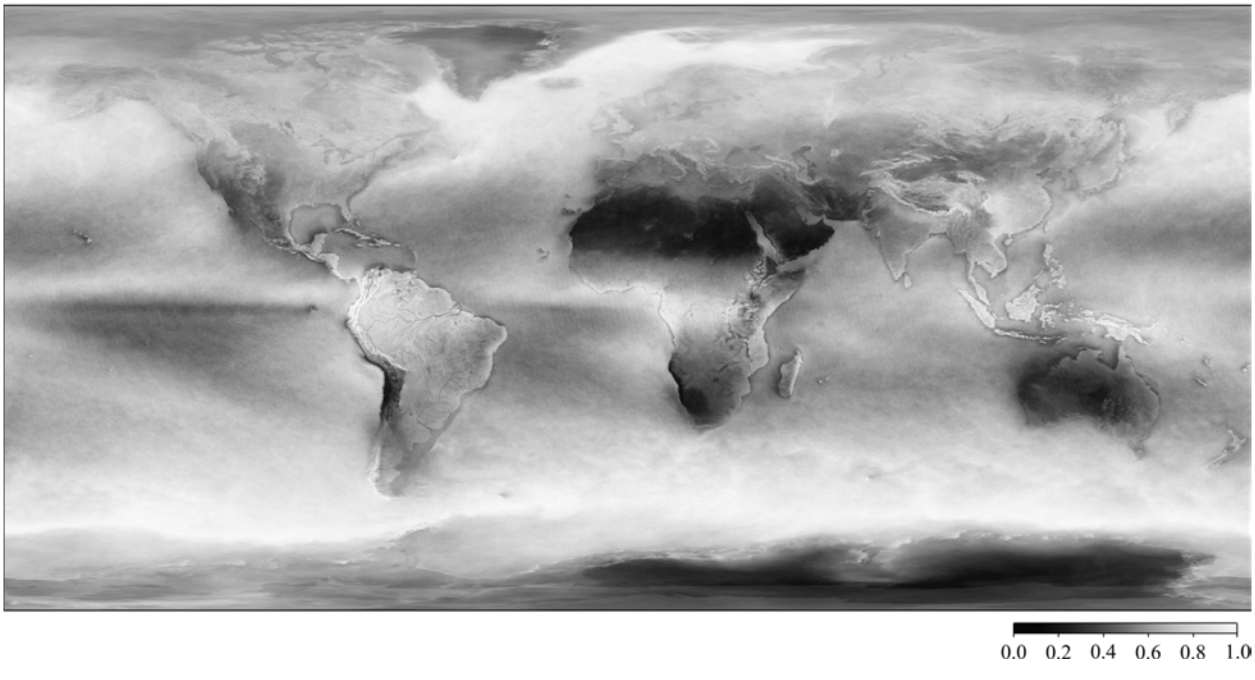

Fig. 1—Yearly mean cloud fraction generated from measurements recorded by the Moderate Resolution Imaging Spectroradiometer onboard Aqua satellite during 2019. Cloud fraction is defined as the portion of each pixel that is covered by clouds. Colors range from dark (no clouds, cloud fraction of 0) to white (totally cloudy, cloud fraction of 1).

Condensed water particles in clouds are known as hydrometeors and exist in liquid, solid, or mixed phase. [1, 4] The distribution of hydrometeors within a cloud is a function of altitude, with liquid particles exclusively

---

Manuscript approved February 28, 2023..

existing between the surface and 4.5 *km*, a mixture of liquid, solid, and two-phase particles appearing in a transition region between 4.5 - 7 *km*, and nearly only solid particles surviving at altitudes between 7 - 18 *km*. [5, 6]

Hydrometeors can be further classified as *cloud* or *precipitating* particles depending on their size and motion behavior. Cloud particles are relatively small and are constantly suspended by updrafts in the atmosphere. Precipitating particles on the other hand are much larger and cannot be supported by updrafts so they fall to the ground. [4] Examples of cloud particles include cloud droplets, which have a characteristic diameter of about 20 microns, and ice crystals which tend to be tens of microns to a few hundred microns. [4] Raindrops, snowflakes, graupel, and hail are all examples of precipitating particles and range in size from a few hundred microns to a few centimeters. [4]

1.1.2 Formation of Hydrometeors

When warm and unsaturated moist air rises to regions of lower pressure in the atmosphere, it expands adiabatically and cools down. In this process, damp air becomes saturated initially but if the ascent is continued to sufficient altitudes, supersaturation[1]occurs and water vapor condensation takes place. [7, 8] Condensation proceeds through a process known as nucleation in which molecules aggregate to form clusters. [9] Nucleation is *heterogeneous* when the agglomeration of molecules occurs onto an existing surface or impurity and *homogeneous* when the grouping only involves gas molecules. [9, 10]

Condensation of water in the atmosphere happens exclusively through heterogeneous nucleation and occurs onto aerosol particles such as clay, sea salt, sulfate, and organic matter. [7, 9, 11] These particles are known as cloud condensation nuclei and exist in varying number concentrations from 2,000-5,000 per cubic meter and have diameters between 0.02 - 0.2 microns. [7, 9] Small cloud droplets are therefore born around small impurities in the atmosphere and upon birth have a characteristic diameter of approximately 20 microns. [12]

After their initial formation, cloud droplets may increase in size and become raindrops through coagulation and/or gas-to-particle conversion processes. [9] Coagulation involves more than one particle and occurs when droplets collide and coalesce to form larger particles. One example of a gas-to-particle conversion process that results in droplet growth is water vapor diffusing to its surface and condensing. [9] From the initial condensation nucleus all the way to the formation of a raindrop, droplet size and terminal velocity increase considerably as shown in Table 1. [12]

Table 1—Typical sizes and terminal velocities of liquid particles in clouds. [12]

Particle	**Diameter, μm**	**Terminal Velocity, *m/s***
Typical Condensation Nucleus	0.2	0.000001
Typical Cloud Drop	20	0.01
Cloud Drop/Raindrop Conventional Borderline	100	0.27
Typical Raindrop	2000	6.50

Ice particle generation in the atmosphere requires air to be saturated and can occur through homogenous or heterogenous nucleation depending on temperature. [10, 13] Homogenous nucleation of ice particles will

---

[1] Supersaturation is defined as the ratio of actual vapor pressure to the equilibrium saturation value corresponding to the local temperature.

occur in the atmosphere at temperatures below $-35°C$. Heterogenous nucleation takes place at warmer temperatures up to $0°C$ but requires the assistance of insoluble aerosols such as biological particles, minerals, and soot. [12, 13] These aerosols known as "ice nuclei", have a molecular spacing and crystallographic arrangement similar to the hexagonal structure of ice which facilitates the ice phase initiation in water. [8, 12] Once initial ice particles have formed through nucleation, they can grow to become crystals, snowflakes, and other forms of solid precipitation through different mechanisms described elsewhere. [8, 14]

1.1.3 Hydrometeor Size Distributions

Cloud drops are essentially spherical but raindrops have shapes ranging from oblate to asymmetric spheroids. [15] This is a natural consequence of cloud drops being gently suspended by atmospheric updrafts and raindrops experiencing significant aerodynamic forces as they accelerate towards the ground. Despite having different shapes, the main parameter used by researchers to characterize cloud drop and raindrop size is droplet diameter.

The typically accepted size demarcation between cloud drops and raindrops is 0.1 *mm*, with raindrops having diameters larger than that benchmark value. [6, 16] Raindrop measurements have shown these hydrometors can reach diameters up to 5 *mm* but larger sizes are not observed because they are torn apart prior to reaching the ground. [6, 16]

Within that 0.1 - 5 *mm* diameter range, raindrop size distributions have been extensively characterized by researchers using meteorological data and mathematical models. [6, 17–20] Among those, Tattelman and Willis developed and validated a model for droplet size distributions applicable up to 20 *km* in the atmosphere based on high-intensity rainfall measurements obtained during aircraft research of Atlantic hurricanes and tropical storms. [6] The basis of their model was the gamma distribution function shown in Eq. (1) where D is the droplet diameter, N_O is the concentration parameter, α is the curvature parameter, and Λ is the slope parameter. [20] Expressions for these parameters are provided in Eq.(2-4) below and were established by Tattelman and Willis by fitting a normalized distribution which included the entire data set collected at four flight altitudes (150, 450, 1500, and 3000 *m*). As shown in Eq.(2) and Eq.(4), the concentration and slope parameters are a function of the median volume diameter D_O which is obtained for a given liquid water content M (g/m^3) as shown in Eq.(5). If the liquid water content at a certain altitude is known, Eq.(1) can be used to predict the corresponding droplet size distribution at that altitude.

$$N(D) = N_O D^{\alpha} exp\left(-\Lambda D\right) \qquad 0 < D < D_{max} \tag{1}$$

$$N_O = \frac{512.85 M \cdot 10^{-6}}{D_O^4} \left(\frac{1}{D_O}\right)^{2.16} \tag{2}$$

$$\alpha = 2.16 \tag{3}$$

$$\Lambda = 5.588/D_O \tag{4}$$

$$D_O = 0.1571 M^{0.1681} \tag{5}$$

Strict guidelines on climatic information are provided in the MIL-STD-210C standard to determine design and test requirements for military systems and equipment that must operate at altitude. [5] Specifically, this standard establishes that military equipment must be designed to operate at all rainfall conditions aside from extreme conditions occurring less than 0.5% of the time. [5] The highest rainfall rate observed at this reference frequency is reported by the military standard to be 0.6 mm/min based on surface measurements recorded in northeast Brazil and east India. [5]

Research on vertical radar reflectivity with altitude has shown that when high precipitation rates reach the ground, rainfall rate and precipitation water content are reasonably constant from the surface up to about 6 *km* and decrease above that altitude. [21, 22] For the extreme surface rainfall rate of 0.6 mm/min occurring 0.5% of the time, the corresponding precipitation water content is 1.6 gm/m^3. [5] Using this reference value to define the liquid water content M in Eq.(5), the correlation developed by Tattelman and Willis presented above can be used to determine a relevant and characteristic droplet size distribution a military vehicle may encounter in the lower troposphere.

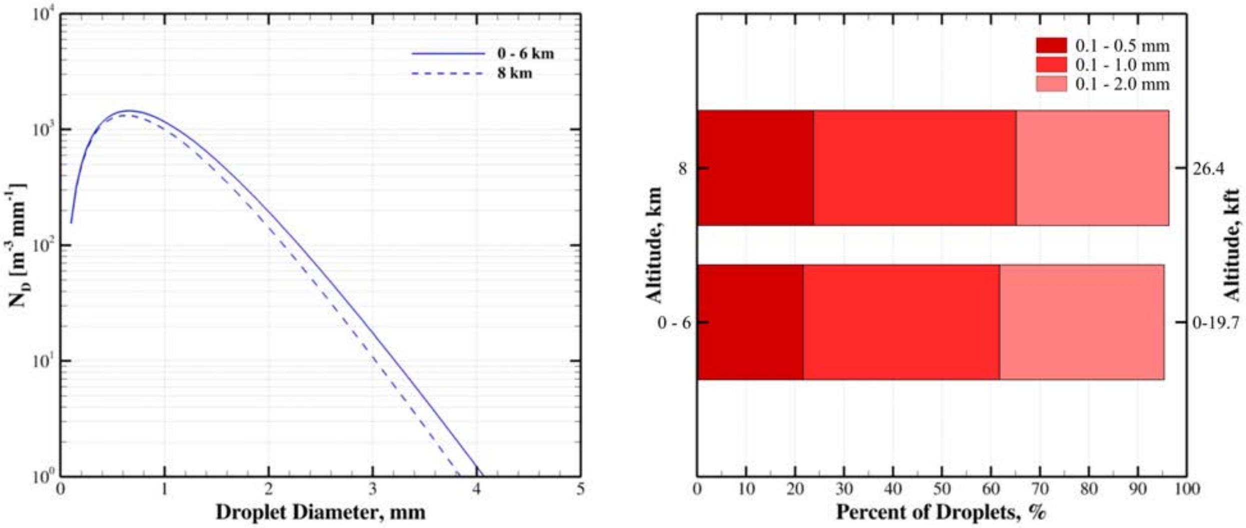

Fig. 2—Droplet size distributions predicted using correlation by Tattelman and Willis for altitudes between 0 - 8 *km* (*left*), percentile statistics for predicted droplet size distributions (*right*).

Figure 2 displays the droplet size distributions predicted with Eq.(1) for altitudes between 0 - 8 *km*. This altitude range was carefully selected based on the available data to avoid higher altitudes where the atmospheric temperature drops below $-10°\mathrm{C}$ and any condensation transitions to ice exclusively. Note also that the results presented in this figure are provided in number of droplets N_D per m^3 per *mm* size.

As expected, the droplet size distributions obtained at altitudes between 0 - 6 *km* in Figure 2 are identical because the precipitation water content remains constant in that altitude range. At a slightly higher altitude of 8 *km*, the droplet size distribution obtained is qualitatively very similar to the results obtained for the 0 - 6 *km* range but shows a slight decrease in the droplet population for every droplet size as a result of a modest decrease in precipitation water content. Both distributions presented in Figure 2 however peak at around the same droplet size (0.5 - 1 *mm*). Finally, note that the smallest raindrop size in these distributions is 0.1 *mm* because the model by Tattelman and Willis is only applicable for raindrops larger than that threshold value and any droplets smaller than that value are non-precipitating cloud drops.

Additional insight from the droplet size distributions can be obtained by visualizing the results in terms of percentiles. The bar chart in Figure 2 provides this information and shows how for altitudes between 0 - 6 *km*, droplets with sizes between 0.1 - 0.5 *mm* comprise 22% of the total droplet population. Similarly, 62% of the droplet population has diameters between 0.1 - 1.0 *mm* and 95% has diameters between 0.1 - 2.0 *mm*. The percentile results obtained for the droplet size distribution at 8 *km* altitude shows a very similar behavior.

1.2 Motivation

1.2.1 Hypersonic Glide Vehicle Trajectories

Transatmospheric boost-glide weapons are rocket-propelled to orbital and suborbital altitudes and then glide at hypersonic speeds through the atmosphere to impact a ground target. [23] A representative boost-glide trajectory calculated using HOTSHOT[2]for a 500 kg blunted cone launched from the ground using a two-stage booster is shown in Figure 3 below. [24]

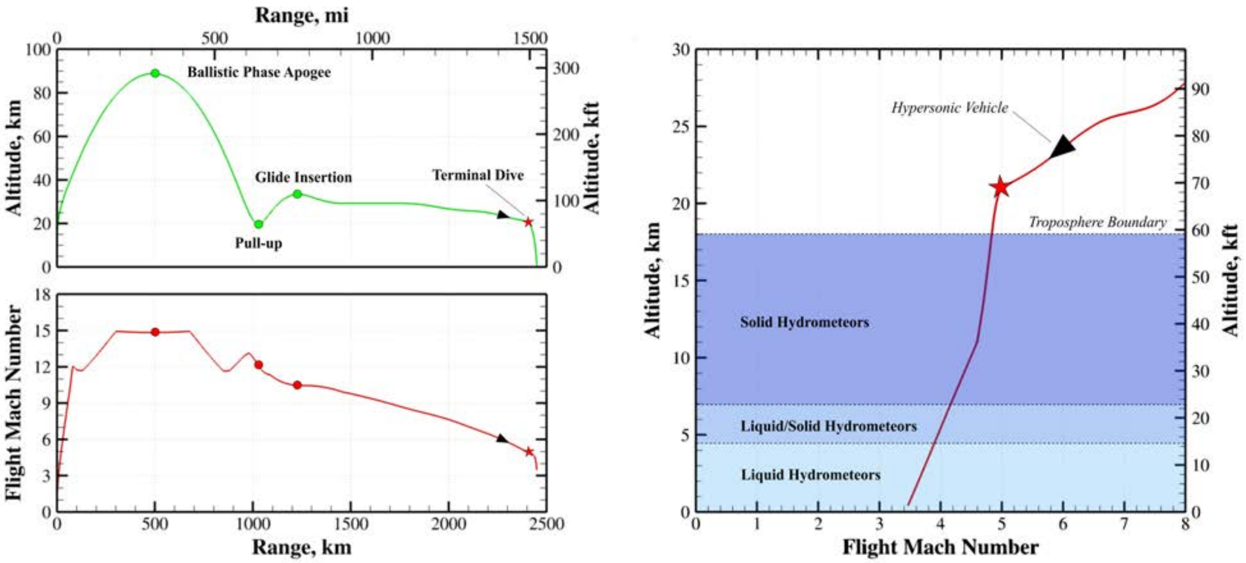

Fig. 3—Altitude and flight Mach number versus range for an exemplar boost-glide vehicle trajectory (*left*), close up view of hypersonic vehicle terminal dive through troposphere (*right*). Red star indicates start of terminal dive.

---

[2] High-Order Thermal Simulation for Hypersonics with Optimization of Trajectories (HOTSHOT) is a boost-glide trajectory simulation tool with full 3-D transient thermal analysis capability developed at the U.S. Naval Research Laboratory.

The first phase of the sample boost-glide trajectory illustrated in Figure 3 is a relatively short rocket-propelled stage which ends with booster burnout and blunted cone (payload) separation at an altitude of approximately 40 *km*. After this initial flight segment, the blunted cone enters a ballistic phase with a Mach 15 apogee at an altitude of approximately 90 *km* followed by a Mach 12 perigee at about 20 *km*. At this point, the vehicle performs a pull-up maneuver to enter into a glide phase at an altitude of about 33 *km* and Mach 10.5. The final flight phase is a terminal dive which begins very close to its target at an altitude of 20 *km* and Mach 5. As shown in the close up view of the trajectory in Figure 3, in this final flight segment the vehicle enters the troposphere and decelerates sharply before impacting its ground target at approximately Mach 3.5. Based on this notional BGV flight trajectory, note how atmospheric weather encounters with liquid hydrometeors would therefore occur at flight Mach numbers in the 3.5 - 5 range at altitudes between 0 - 7 *km*.

1.2.2 Weather Encounters of Hypersonic Glide Vehicles

A large number of scientific and engineering efforts have sought to develop thermal protection technologies for hypersonic vehicle surfaces which are subject to extreme aerothermal heating during flight[3]. However, the vast majority of those studies have been conducted under “ideal” weather conditions, i.e. without considering the interaction of these surfaces and materials with atmospheric water particles found specifically in clouds.

For a boost-glide hypersonic vehicle entering into the lower atmosphere prior to reaching its target, hydrometeor encounters are a realistic mission threat because they can lead to undesirable vehicle surface erosion with detrimental consequences ranging from reduced flight control to catastrophic failure. Although it is safe to assume the likelihood of mission failure is high when collisions occur with large hydrometeors such as snowflakes, graupel or hail, a more thorough analysis is required to evaluate the risk associated with encounters involving smaller particles such as cloud droplets, raindrops, and ice crystals.

The main motivation of this work is therefore to improve our understanding of the fundamental physics of droplet/shock layer interactions as shown in Figure 4. Liquid hydrometeors undergo deformation, mass stripping, evaporation, and possibly shattering as they transit through this layer prior to reaching the vehicle surface. [25] Understanding and characterizing these events is important because they will ultimately affect key impact parameters such as hydrometer final mass, velocity, and shape. All of these are critical to predicting the level of erosion a vehicle surface may suffer and additional knowledge about them will aid the design of more robust hypersonic vehicles capable of being deployed in a wider range of weather conditions.

---

[3] The most recent Department of Defense effort on this front is the ongoing Materials Architecture and Characterization for Hypersonics (MACH) program by the Defense Advanced Research Projects Agency (DARPA).

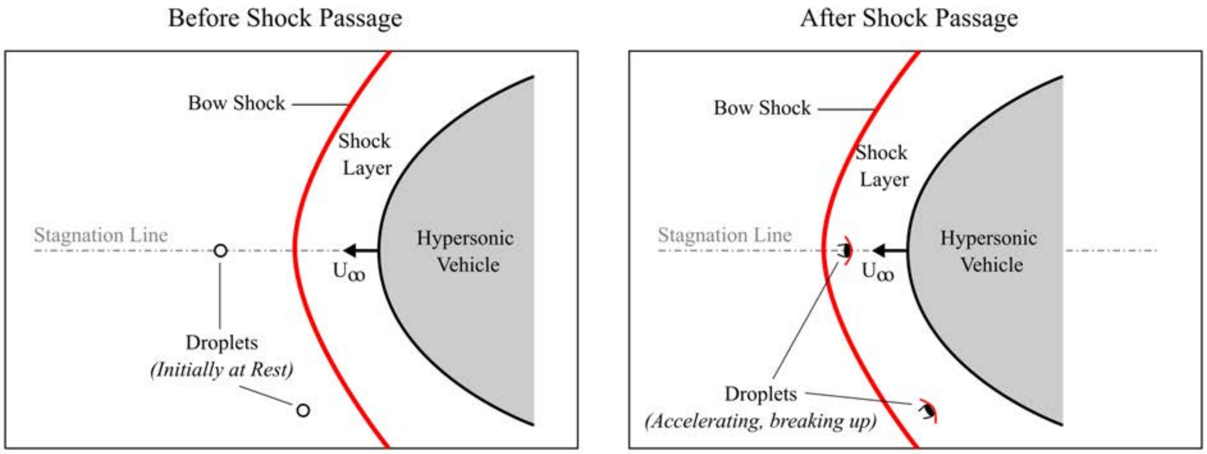

Fig. 4—Schematic of atmospheric droplets interacting with bow shock of a hypersonic vehicle along the stagnation line and below it.

1.3 Technical Objective and Approach

The overall objective of this work was to investigate the interaction of liquid-phase hydrometeors found in clouds with a hypersonic vehicle flow field to help predict surface erosion and extrapolate possible aerodynamic performance degradation. For this purpose, the technical approach undertaken is summarized as follows:

- Provide an assessment as to current state-of-the-art in the modeling of hydrometeor-induced erosion,
- Identify best practices for characterizing the interaction of droplets with curved shock waves,
- Generate a data set of relevant water droplet trajectories and demise in supersonic and hypersonic flows generated in a laboratory environment,
- Demonstrate the ability of high-resolution numerical simulations to reproduce droplet demise in a hypersonic environment.

These issues will be discussed in greater detail throughout the remainder of this report.

2. THEORY AND PREVIOUS WORK

Prior to impacting the surface of a hypersonic vehicle, liquid hydrometeors interact with a shock layer and are subject to deformation and breakup. A discussion of vehicle surface erosion due to atmospheric weather encounters must therefore begin by analyzing that complex droplet/shock layer interaction. This chapter starts with a brief summary of droplet breakup theory, provides an overview of previous experimental efforts on droplet interactions with planar and non-planar shocks, and concludes with a section on physics of droplet-induced erosion.

2.1 Droplet Aerobreakup

2.1.1 Weber Number

Liquid droplet deformation and shattering due to the sudden exposure to a high speed gas flow is known as “aerobreakup” and has been thoroughly investigated in the literature. [26–31] Most of the experimental work in this field has been performed using shock tubes which generate a moving normal shock and allow for the assumption of one-dimensional flow. In that facility, after being traversed by a planar shock, an initially stationary droplet experiences a large aerodynamic force due to the high dynamic pressure of the post-shock flow. [32] The Weber number is a nondimensional parameter useful to quantify the magnitude of that aerodynamic force relative to the tension force keeping the droplet together and is given by

$$We = \frac{\rho_2 (U_2 - U_{d,0})^2 D_0}{\sigma} \tag{6}$$

where

ρ_2 is the gas density behind the shock
U_2 is the gas flow velocity behind the shock
$U_{d,0}$ is the initial droplet velocity before being traversed by the shock
D_0 is the initial droplet diameter before being traversed by the shock
σ is the surface tension of the droplet evaluated at conditions upstream of the shock.

For a water droplet in a flowfield where the Weber number is larger than one but less than a critical value, the droplet will deform as a result of the aerodynamic force exerted by the flow but will not break. [33] Experimental research of droplets exposed to high velocity gas flows has shown that the critical Weber number for droplet breakup is governed by the Ohnesorge number which relates droplet viscous forces to inertial and surface tension forces as shown in Eq. (7). [29]

$$On = \frac{\mu_d}{\sqrt{\rho_d D \sigma}} \tag{7}$$

Here, μ_d is the dynamic viscosity of the droplet, ρ_d is the droplet density, and D is the droplet diameter. The critical Weber number We_c has been found to correlate well with the Ohnesorge number through Eq.(8)

below. [34] Water droplets with diameters between 0.1 and 2 *mm* have Ohnesorge numbers between 0.0027 and 0.0118 and corresponding critical Weber numbers between 12.001 and 12.011.

$$We_c = 12\left(1 + 1.077 \cdot On^{1.6}\right) \tag{8}$$

At Weber numbers larger than this critical value, five distinct droplet breakup modes have been identified experimentally for water. Figure 5 summarizes these modes and includes the Weber number range typically associated with each of them. [29, 33]

Breakup Mode	Weber Number	Description	Schematic (time →)
Vibrational	We ≤ 12	Under certain conditions, drop oscillates then breaks up into two smaller droplets, however this does not necessarily occur in every instance.	
Bag	12 < We ≤ 50	Hollow bag is formed spanning a ring of fluid but then bursts into smaller droplets. Ring disintegrates a short time later.	
Bag-and Stamen	50 < We ≤ 100	Similar to bag breakup but with formation of central liquid stamen prior to bursting. Stamen disintegrates with ring after bag.	
Sheet Stripping	100 < We ≤ 350	Droplet flattens and a thin sheet is continuously drawn and stripped from the droplet poles, disintegrating into a mist of small droplets in its wake.	
Wave Crest Stripping plus Catastrophic Breakup	We > 350	Large-amplitude and long-wavelength waves form along the windward surface of the droplet. Penetration of these waves into the droplet before mass reduction by stripping tear the droplet apart.	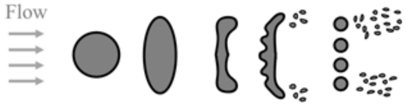

Fig. 5—Breakup modes of water droplets observed experimentally. [29, 33] Schematics from Bergeles. [35]

2.1.2 Interfacial Instabilities

There are two main interfacial instabilities involved in droplet aerobreakup: Rayleigh-Taylor (RT)[4]and Kelvin-Helmholtz (KH)[5]instability. [31] The interface between the forward stagnation point of a droplet or equator and the high speed air is susceptible to RT instability, while the KH instability plays a more dominant role away from the stagnation point and closer to the droplet poles. Droplet breakup modes in Figure 5 are governed by those instabilities and can be divided into two main regimes based on whether gas flow goes *through* the droplet or *around* the droplet. [31] Breakup modes where droplet flattening occurs followed by unstable wave penetration belong to the Rayleigh-Taylor Piercing (RTP) regime while modes involving droplet surface peeling or shedding are associated with the Shear-Induced Entrainment (SIE) regime. [31] Various analytical droplet breakup models have been formulated in the literature based on RT and KH instabilities. [36]

2.2 Interaction of Droplets with Vehicle Shock Layers

Droplet encounters with a hypersonic vehicle can occur at the nose, along a planform surface, or an afterbody leading edge. Droplet interactions can therefore occur with a planar shock at the stagnation region of the nosetip or a non-planar shock everywhere else. Due to the non-uniform shock layer flowfield surrounding the vehicle, the range of Weber numbers of interest is large. Factor in different droplet sizes and that range becomes even broader.

To illustrate this point consider an analysis similar to the one performed by Reinecke el al. where droplets with diameters of 0.1 and 2.0 *mm* interact with the hypersonic shock layer of a blunt cone at the nose and afterbody regions. [33] Assuming this vehicle is flying at Mach 4 at an altitude of 5.39 *km* and the cone half-angle is 5°, the corresponding Weber numbers for each droplet at each shock layer region are summarized in Table 2.

Table 2—Sample Weber numbers for droplets interacting with hypersonic vehicle shock layers.

	Nose Shock Layer		**Afterbody Shock Layer**	
Droplet Size	Normal Shock Mach Number	Weber Number	Equival. Normal Shock Mach Number	Weber Number
mm	-	-	-	-
0.1	4.00	4,235	1.03	0.3
2.0	4.00	84,702	1.03	6

From the above, notice the large Weber number difference between droplets interacting with the shock layer in the nose and the afterbody region of the cone. More importantly, note how this range of Weber number encompasses values both below and well above the critical Weber number for droplet breakup ($We_c \sim 12$).

Research on droplet interactions with vehicle shock layers has therefore considered a large range of Weber numbers and interactions with both planar and non-planar shocks. The following sections highlight some of the experimental work performed in those areas.

2.2.1 Interactions with Planar Shocks

Multiple research efforts have experimentally investigated droplet breakup behind normal shocks for a range of Weber numbers and shock Mach numbers. [26, 27, 30, 33, 37, 38] Most of those studies however

---

[5] Interfacial instability found when a light or less dense fluid is accelerated into a heavy or denser fluid. [31]

[6] Interfacial instability in parallel flows with different densities and velocities. [31]

have been fundamental in nature and have focused on characterizing droplet breakup modes using the Weber number as a main parameter. Less work has been performed on droplet interactions with normal shocks from the perspective of weather encounters with the stagnation region of a hypersonic vehicle.

The Weber number is a useful tool to make an assessment of droplet breakup downstream of a shocked flowfield, but it does not provide any temporal information about the demise process which is key to the problem of weather encounters in hypersonics. The droplet break-up sequence in Figure 6 from the work by Joseph et al. illustrates this point. Based on the Weber number modes summarized in Figure 5, for the given Weber number of 43,330 in the experiments, wave crest stripping is predicted and is indeed observed in the visualizations, but the expected full breakup (defined as absolute loss of droplet coherence) has not occurred after 190 μs of test time.

In the context of a droplet penetrating a shock layer of a hypersonic vehicle, knowing how much progress into the breakup process occurs prior to impact is critical to study the physics of the encounter and make any erosion potential assessments. Specifically, it is important to determine the droplet break-up time and mass history as it transits through the shock layer. Research on droplet interactions with planar shocks applied to hypersonics have therefore concentrated on predicting droplet breakup time, mass history, and impact time as summarized next.

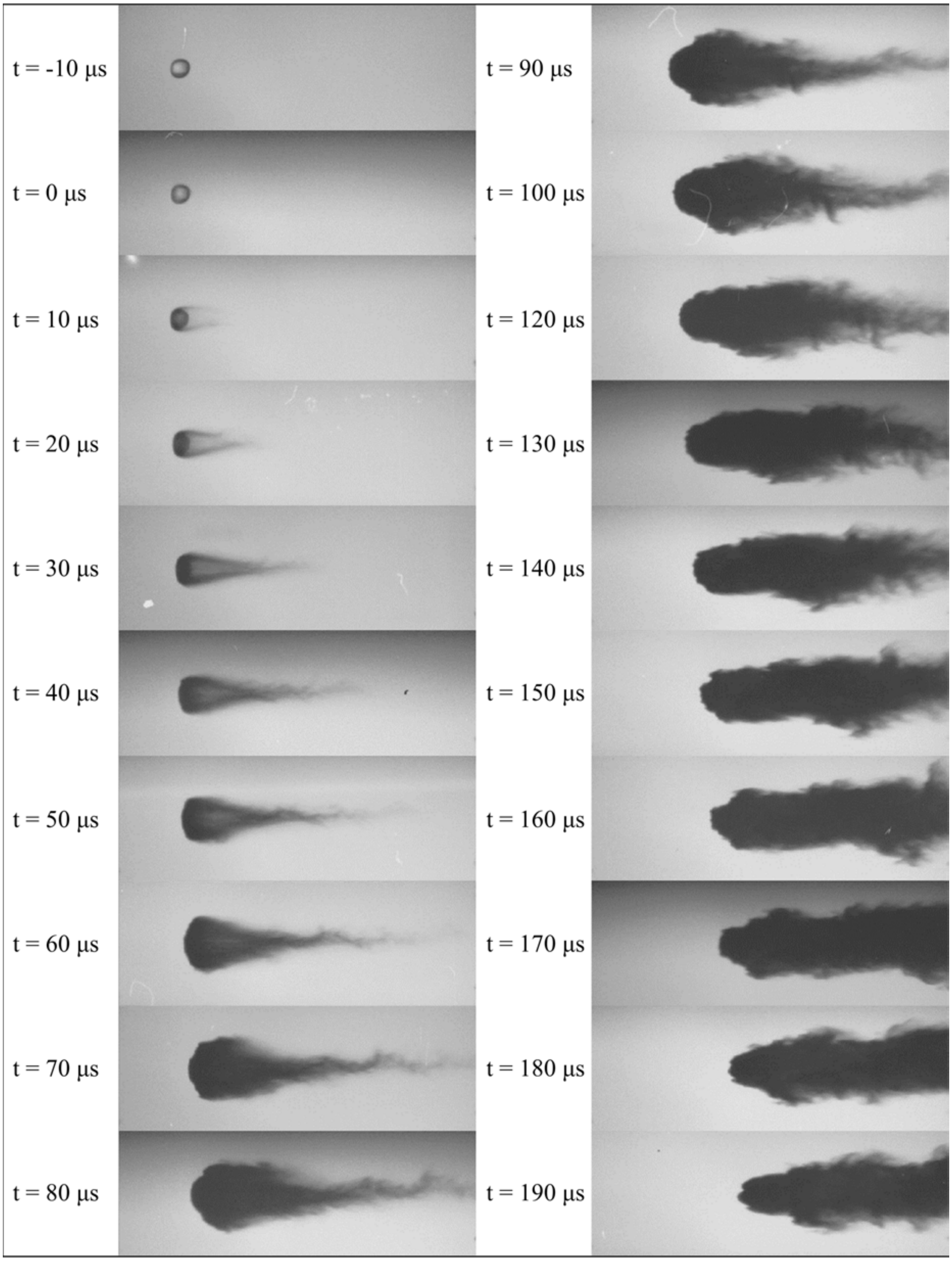

Fig. 6—Breakup sequence of a 2.5 *mm* water droplet exposed to the flow behind a Mach 3 shockwave. Weber number = 43,330. Image sequence generated from data made public from [38].

Droplet Break-up Time

The experimental work performed by Reinecke and Waldman in the early to mid 1970's is to this day one of the main references in the study of droplet behavior across shocks for application to hypersonic vehicles. [25, 33]. In their initial work, they performed a series of shock tube tests where spherical droplets with diameters between 0.5 and 2.5 *mm* were traversed by shocks moving at Mach 3, 6, 9 and 11 at pressure altitudes of sea level, 20 kft, and 40 kft.[25] Qualitative observations of droplet behavior after shock passage were gathered from shadowgraphs and quantitative assessments of droplet mass loss with time were obtained using X-radiographs. The data collected was used to develop correlations to predict droplet breakup time and mass history.

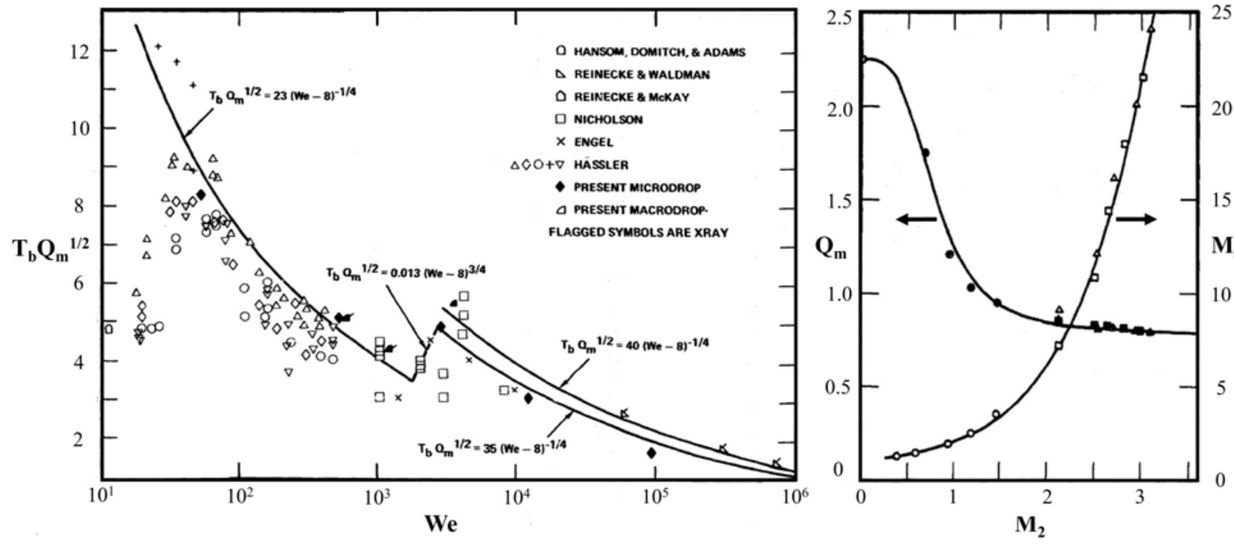

Fig. 7—Droplet breakup time data with correlations proposed by Reinecke *(left)*, maximum dynamic pressure factor Q_m and shock Mach number M_s as a function of flow Mach number M_2 behind the shock *(right)*. Plots adapted from [33].

Shadowgraphs from their experiments showed how upon initial exposure to the flow behind the shock wave, spherical water droplets were flattened by the pressure differential between their stagnation point (equator) and the top and bottom of the droplet (poles). [25] Following this initial deformation, mass stripping and catastrophic droplet breakup were both observed throughout the tests.

Reinecke and Waldman described material stripping as a process which starts by air moving over the surface of the droplet and dragging some fluid along with it. As this fluid reaches the poles of the droplet, it separates and is swept away by the wake of the droplet as a fine mist. [25] Water particles removed in this stripping process are very small and either evaporate or are absorbed by local streamlines moving away from the vehicle body. [33]

Catastrophic droplet breakup is identified by a rapid growth of surface waves on the windward side of the droplet which turns unstable when the amplitude of the waves becomes comparable to the dimensions of the drop and ultimately tears the droplet apart. [25] Droplet fragments that remain after the droplet shatters may be large enough to continue on a collision course with the vehicle or may continue to catastrophically break until they reach a Weber number below the critical value. [33]

Droplet mass histories after shock passage obtained from X-radiographs in their experiments indicated that mass stripping occurred for all the test conditions evaluated and always preceded catastrophic droplet breakup. Examination of droplet breakup times for Weber numbers between 60,000 - 700,000 showed that mass stripping progressed further prior to catastrophic breakup with decreasing Weber number. Using flow properties behind the passing shock, the initial droplet diameter $D_{d,0}$, and the droplet density ρ_l, Reinecke et al. defined a nondimensional time T as shown in Eq.(9) and used this parameter to define a nondimensional breakup time T_b occurring when $t = t_b$.

$$T = \frac{U_2}{D_0}\sqrt{\frac{\rho_2}{\rho_d}} \cdot t \tag{9}$$

With their experimental data, they then developed a correlation for T_b as a function of Weber number shown in Eq.(10).

$$T_b = 45 \cdot We^{-0.25} \tag{10}$$

Additional work performed by Reinecke a few years later tested water droplets with diameters between 50 - 300 microns and 500 - 2500 microns with shocks traveling between Mach 1.3 - 12.6 and Weber numbers in the 50 - 95,000 range. [33] The droplet breakup time results from this investigation and the extensive examination of experimental results obtained by other researchers led Reinecke to the conclusion that more than one correlation for droplet breakup time was required to better fit low Weber number ranges and that his initial correlation could be revised. He therefore proposed three new correlations for droplet breakup time using the Weber number and a new nondimensional parameter Q_m defined as the maximum value of the ratio between the dynamic pressure of air at the droplet surface and the air flow dynamic pressure ahead of the droplet. These three correlations and their ranges of applicability defined by Reinecke based on Weber number are summarized below. [33] Note here that Reinecke used 8 as the critical Weber for breakup in his correlations and therefore the breakup time predicted grows as the Weber number approaches this value.

$$\begin{aligned} T_b \cdot {Q_m}^{1/2} &= 22\,(We-8)^{-1/4} && We \leq 1700 \\ T_b \cdot {Q_m}^{1/2} &= 0.013\,(We-8)^{3/4} && 1700 < We \leq 2700 \\ T_b \cdot {Q_m}^{1/2} &= 35\,(We-8)^{-1/4} && We > 2700 \end{aligned} \tag{11}$$

A plot showing these correlations and the experimental data Reinecke used to develop them is shown in Figure 7 *(left)*. [33] A figure illustrating the variation of Q_m as a function of flow Mach number M_2 behind the shock is also provided in this figure *(right)*. As a reference, note that for a hypersonic vehicle entering the troposphere at Mach 4 such as the one described earlier for the analysis in Table 2, the flow Mach number

M_2 behind the shock in the nose region is approximately 1.55, which corresponds to a Q_m value from Figure 7 of about 0.93. At higher flight Mach numbers and therefore higher shock Mach numbers M_s in this figure, the approximate value of this parameter approaches 0.8 and its variation is relatively small.

In general, the results summarized in Figure 7 show that the nondimensional breakup time has a $We^{-1/4}$ dependence, except for a small section of the Weber number range between 1000 and 5000 where T_b increases with Weber number. No physical explanation for this behavior has been found in the literature although two separate experimental studies have reported similar observations in this regime. [26, 33]

Droplet Mass History

A mathematical expression for droplet mass history after shock passage was also suggested by Reinecke et al. to be used with the breakup time correlations above and is provided in Eq.(12). [25] This relation shows droplet mass m normalized by initial droplet mass m_0 as a function of time t. According to the author, Eq.(12) has no theoretical foundation but provides a reasonably accurate representation of the experimental data obtained. [25]

$$\frac{m}{m_0} = \frac{1}{2}\left(1 + \cos \pi \frac{t}{t_b}\right) \tag{12}$$

Droplet Impact Time

Application of the droplet breakup time correlations and mass history equation to the analysis of hydrometeer encounters with hypersonic vehicles requires a prediction of the droplet impact time t_i. This parameter is defined as the time it would take a droplet to reach the vehicle after entering the shock layer. Knowledge of this parameter is important because a comparison between t_i and t_b can provide additional insight into the type of collision to take place. If $t_i < t_b$, the droplet will impact the vehicle before shattering and Eq.(12) can be used to determine the final droplet mass at the time of impact (effective mass capable of inducing surface erosion). Conversely, if $t_i > t_b$, catastrophic droplet breakup will occur before the encounter. In this scenario, remnants from the shattered droplet may or may not pose a collision threat depending on their size and how close to the surface the catastrophic breakup took place.

Estimating the droplet impact time t_i requires knowledge of the droplet trajectory and the shock layer thickness which is equal to the shock standoff distance, δ, if the analysis is performed using the stagnation point as a reference. Droplet displacement measurements performed in shock tubes have shown that the constant acceleration formula in Eq. (13) is applicable to this problem. [27, 28]

$$X = A \cdot T^2 \tag{13}$$

From the equation above, X is the nondimensional droplet displacement defined by $X = x/D_{d,0}$, T is the nondimensional time from Eq. (9), and A is a coefficient with a value defined differently by researchers. [27, 33, 39] Reinecke at al. suggested this coefficient could be related to the droplet Weber number based on the examination of data found in the literature and provided the following formulas:

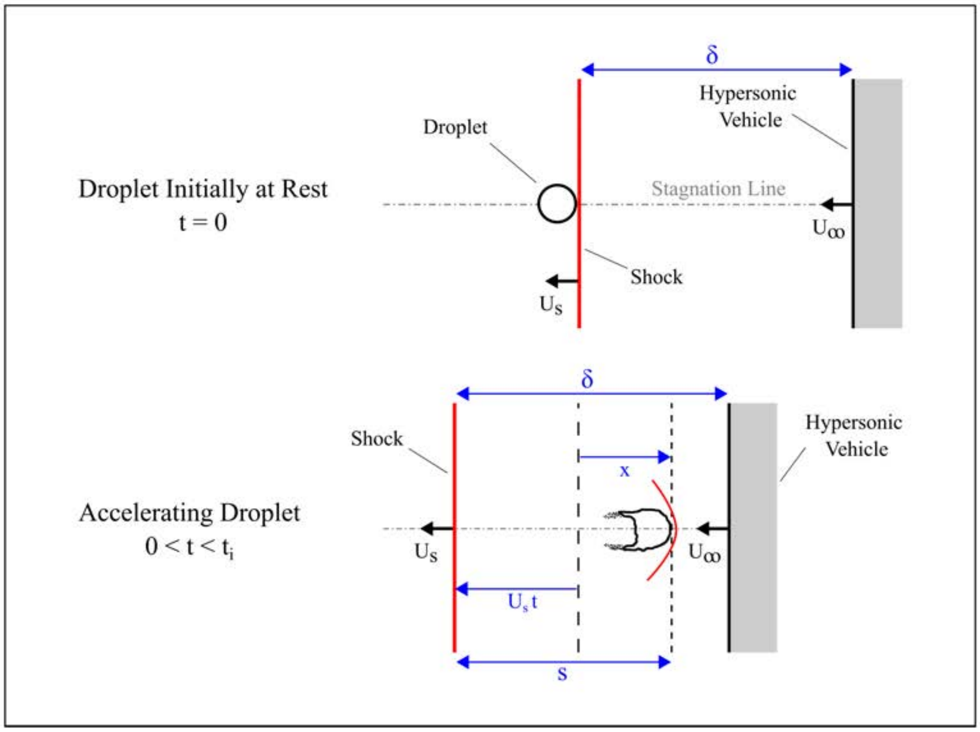

Fig. 8—Graphical representation of droplet transit through shock layer at stagnation point used for impact time calculations.

$$\begin{aligned} A &= 0.252 \ln We && 12 \le We \le 300 \\ A &= 2.966 - 0.268 \ln We && 300 \le We \le 8000 \\ A &= 0.062 \ln We && We \ge 8000 \end{aligned} \tag{14}$$

If the droplet displacement through the shock layer is obtained with Eq.(13) and the shock standoff distance δ is estimated using a validated correlation such as the one recently proposed by Sinclair and Cui in [40], the distance s between the moving shock and the accelerating droplet moving towards the vehicle shown graphically in Fig.8 can be predicted using Eq.(15). From this last equation, note that U_s is the shock speed which is equal to the vehicle flight speed, U_∞.

$$s = U_s \cdot t - x \tag{15}$$

At the time of droplet impact with the vehicle, $s = \delta$, $t = t_i$, and $x = x_i$ in Eq.(15). The correlation for droplet displacement provided in Eq.(13) can then be written in dimensional form at the time of impact as shown in Eq.(16). This result can then be substituted into Eq.(15) as shown in Eq.(17), which can then be used to solve for t_i.

$$\frac{x_i}{D_0} = A \cdot \left(\frac{U_2}{D_0} \sqrt{\frac{\rho_2}{\rho_d}} \cdot t_i \right)^2 \tag{16}$$

$$\delta = U_s \cdot t_i - \frac{A}{D_0} \cdot \left(U_2 \sqrt{\frac{\rho_2}{\rho_d}} \cdot t_i \right)^2 \tag{17}$$

2.2.2 Interactions with Non-Planar Shocks

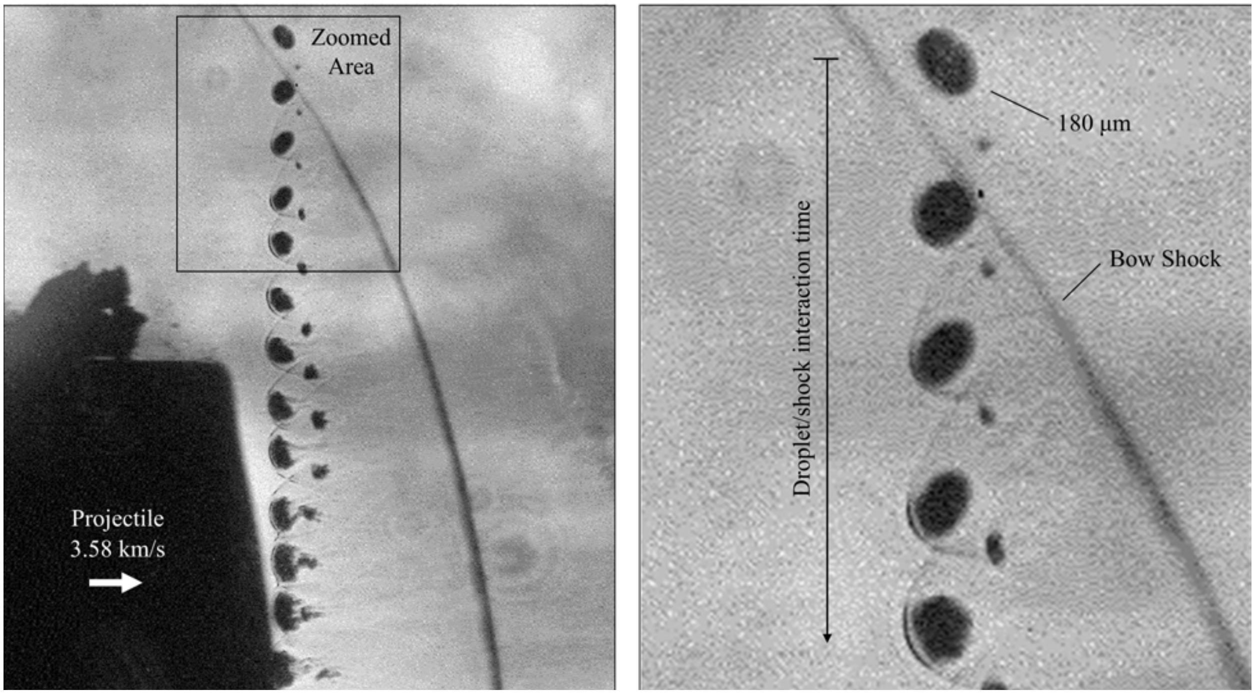

Fig. 9—Photographs of water droplets interacting with a projectile flying at 3.58 km/s *(left)* and zoomed in view of droplets traversed by curved shock *(right)*. Images adapted from [41].

Up to this point, the discussion of droplet breakup in hypersonic shock layers has only considered interactions with planar shocks and is therefore only applicable to weather encounters with the stagnation region of a vehicle i.e. nosetip or leading edge (when flying at a zero angle of attack). Downstream of the stagnation region however, droplets will interact with a curved shock or a conical shock prior to impacting a planform surface.

Key differences in the flowfield behind non-planar shocks in comparison to normal shocks influence droplet demise aft of the vehicle stagnation region. Gradients across non-planar shocks are significantly more benign in comparison to normal shocks and will generate reduced aerodynamic loads on droplets. Three dimensional flow relaxation downstream of a conical shock will also favor droplet survivability. On the other hand, droplet transit times across shock layers downstream of the nosetip or leading edge are much longer, allowing the droplet breakup process to advance further before a potential impact. Characterizing the breakup behavior of a droplet across this complex flowfield is also important to determine the collision conditions just before impact on vehicle surfaces other than the stagnation region.

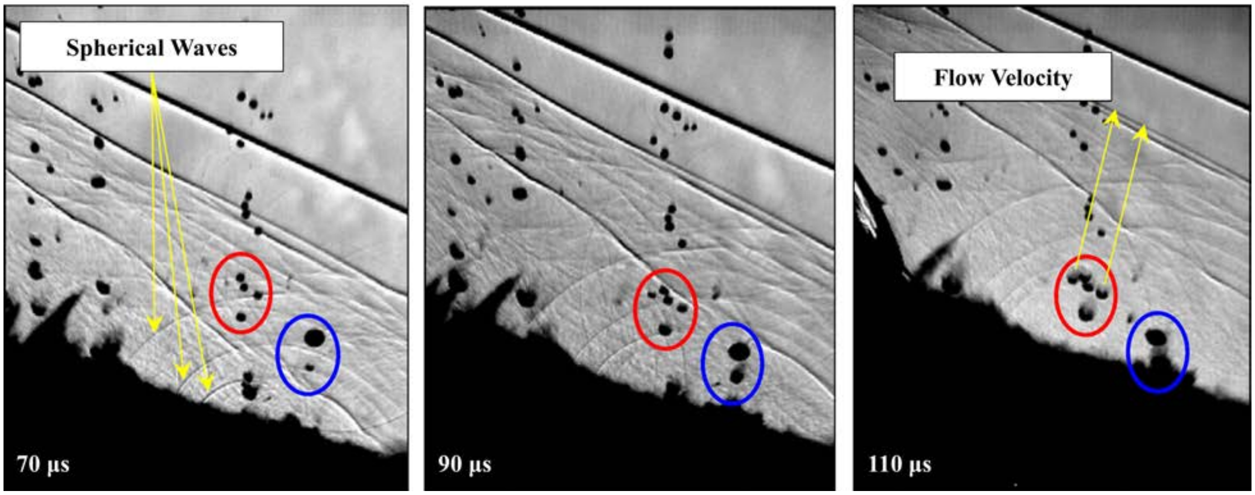

Fig. 10—Droplet transit through conical shock layer of a projectile traveling at 990 m/s. Images adapted from [42].

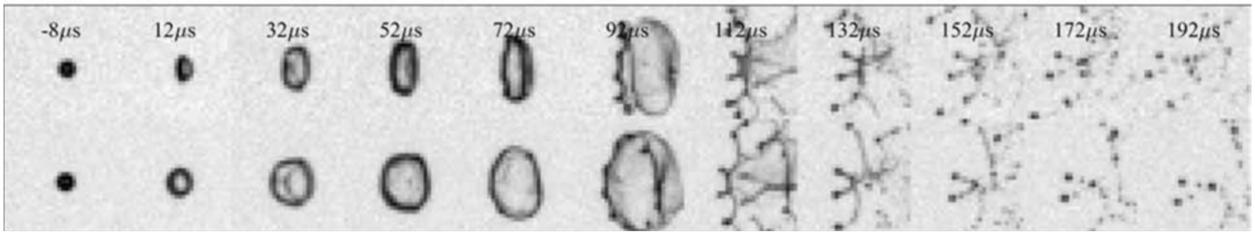

Fig. 11—Stereo views of droplet deformation and breakup due to interaction with conical shock. Images adapted from [43].

From the experimental research on droplet encounters with non-planar shocks in the literature, the work performed by Barber et al. provides some of the best high resolution visualizations of droplet interaction with a curved shock. [41] In their work, the authors used a light gas gun to launch projectiles through streams of falling drops with diameters in the 20 - 200 μm range. Using a Q-spoiled laser with a microscope camera system, they collected observations in two projectile speed regimes: low speed (~ 1 km/s) and high speed (3.7 - 4.3 km/s). Figure 9 provides a sample image obtained by Barber of water droplets penetrating the curved region of the bow shock for one of their high-speed projectiles.

When capturing high-speed images of a projectile collision with a column of droplets, the speed difference between the projectile and the falling droplets is so large that the droplets appear to be stationary or frozen in time as the projectile flies through them. From the zoomed in view of the droplets traversed by the curved section of the bow shock, notice how some droplet flattening begins to occur but no apparent mass stripping is observed. Individual droplet shocks also appear in the image indicating supersonic droplet velocities within the shock layer.

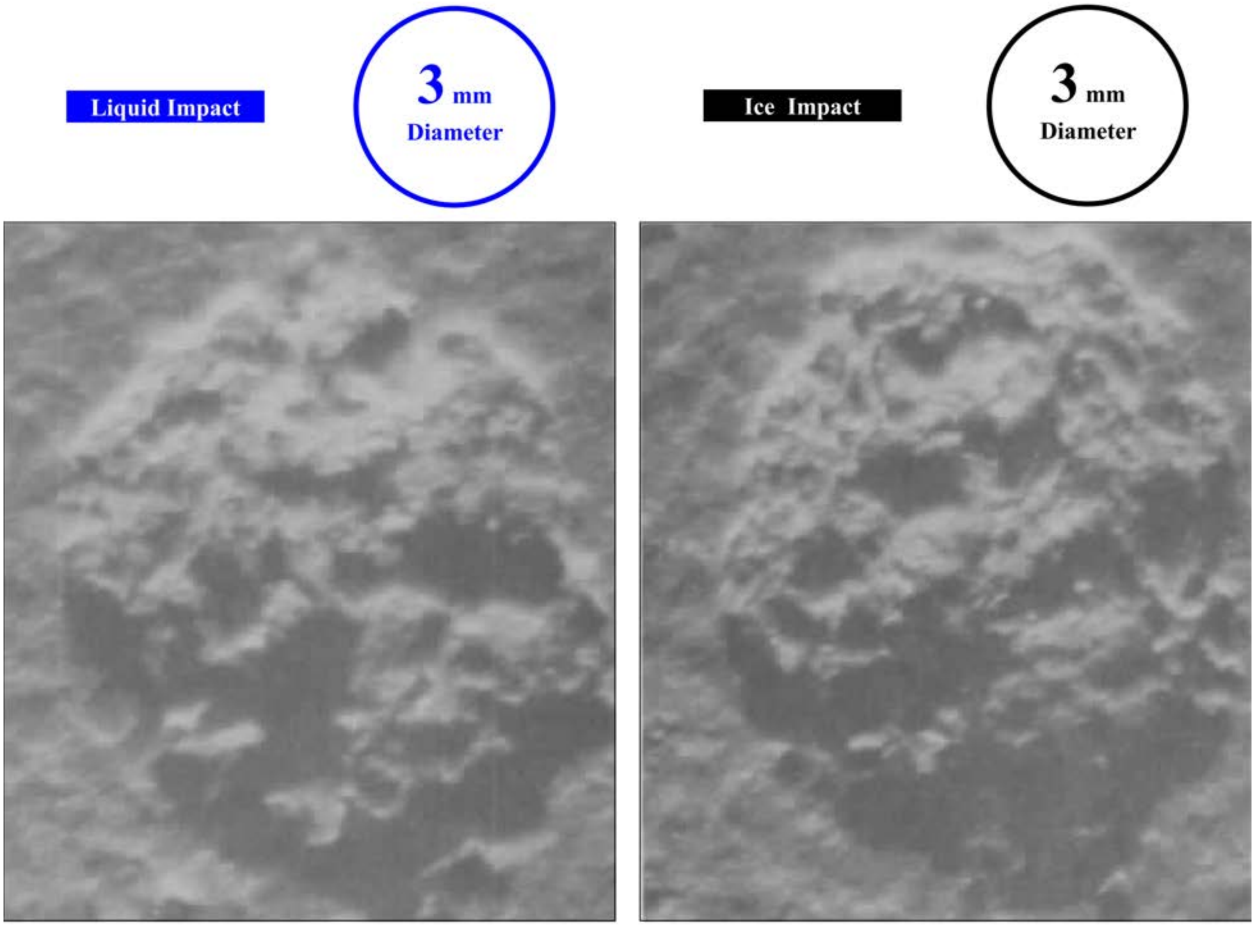

Fig. 12—Impact craters from liquid an solid hydrometeors from sled test experiments at Holloman Air Force Base. The circles depict the size of the hydrometeors relative to the craters. Adapted from [48].

More recent experimental work on droplet interactions with non-planar shock flowfields was performed by Moylan et al. at the University of Alabama ballistics range. [42] For their tests, a 12° cone with a 0.63 *cm* nosetip radius was accelerated to 990 m/s before colliding with a simulated rain field with 1-2 *mm* droplets generated with a custom-made dripper system. Figure 10 shows a sequence of high speed images capturing droplet transit through the conical shock layer prior to surface impact. A distinct feature mentioned by the author of these results is the expansion of droplet diameter with transit time. [42] Mass stripping is observed in the last frame for a small cluster of droplets highlighted in a red circle. Post-impact droplet mist and spherical waves are clearly seen emanating from the surface of the projectile. [42]

The most recent research performed on droplet interactions with non-planar shocks was conducted by Daniel et al. at Sandia National Laboratories, who experimentally investigated water droplet deformation and breakup behind conical shocks generated by 0.22 caliber bullets flying at Mach 4.5. [43] A comparison done by the author of measured droplet break-up time against predictions from literature correlations was in great disagreement, suggesting previous derived correlations using shock tubes and planar shocks is inadequate for conical shocks. One of the main conclusions from their study was that the three dimensional relaxation of flow properties behind a conical shock causes a significantly different droplet response in comparison to the flow step-change and no relaxation that occurs across a normal shock. [43] Figure 11 shows time-synchronized image sequences of droplet breakup captured by Daniel et al. for droplets with a mean diameter of 192 μm traversed by the conical shock from their experiments.

2.3 Weather-Induced Erosion Studies

Droplet impacts on the nosetip or leading edge of a hypersonic vehicle can cause surface shape changes that generate an undesirable drag increase or the development of hotspots that overwhelm the thermal management system. Aft of the vehicle stagnation region, continuous droplet impacts may cause surface roughness changes and material loss that increase frictional drag affecting flight control or cause earlier boundary layer transition. Understanding and predicting weather-induced erosion is therefore crucial to ensure the airworthiness and mission success of a hypersonic vehicle are not compromised during flight.

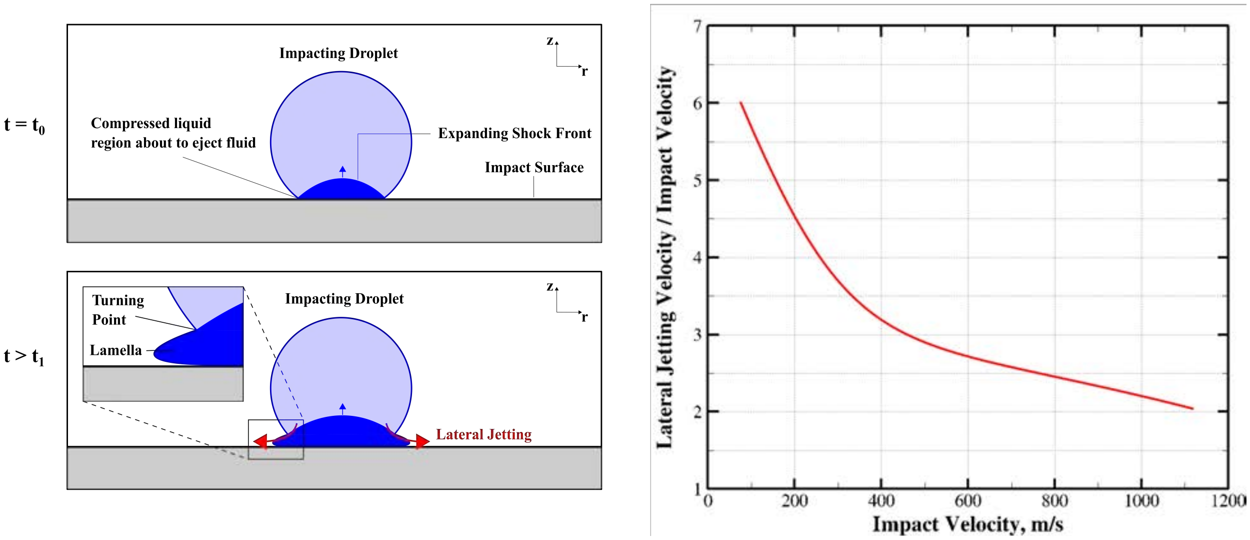

Fig. 13—Schematic of droplet impact showing formation of compressed liquid region within droplet an instant prior to lamella formation *(top left)*, fluid ejection with lamella formation and detail showing turning point *(bottom left)*, redrawn plot with experimental data showing ratio of lateral jetting to impact velocity as a function of impact velocity *(right)*. Schematics adapted from [44, 49–51]

Droplet impact erosion is strongly dependent on multiple parameters that fall into two main categories: impact conditions (collision speed, droplet size, impact angle) and surface characteristics (geometry and material-specific properties). [44] Surface erosion is also a function of number of impacts, so its a time-dependent phenomenon that proceeds in phases.[7] [45, 46] Variable impact conditions, surface design, and time dependency make characterizing erosion using metrics such as surface roughness increase and/or mass loss rate extremely challenging.

An ideal test facility to study weather-induced erosion of hypersonic vehicles would allow accurate reproduction of flight conditions, simulate liquid and solid hydrometeors of relevant size, accommodate long and variable model exposures, fit full scale models, enable impact surface heating, and allow post-test specimen

---

[7] The three phases of erosion are incubation (stress accumulation period), steady state mass loss (linear surface mass loss period), and final erosion (significant mass loss period). [45, 46]

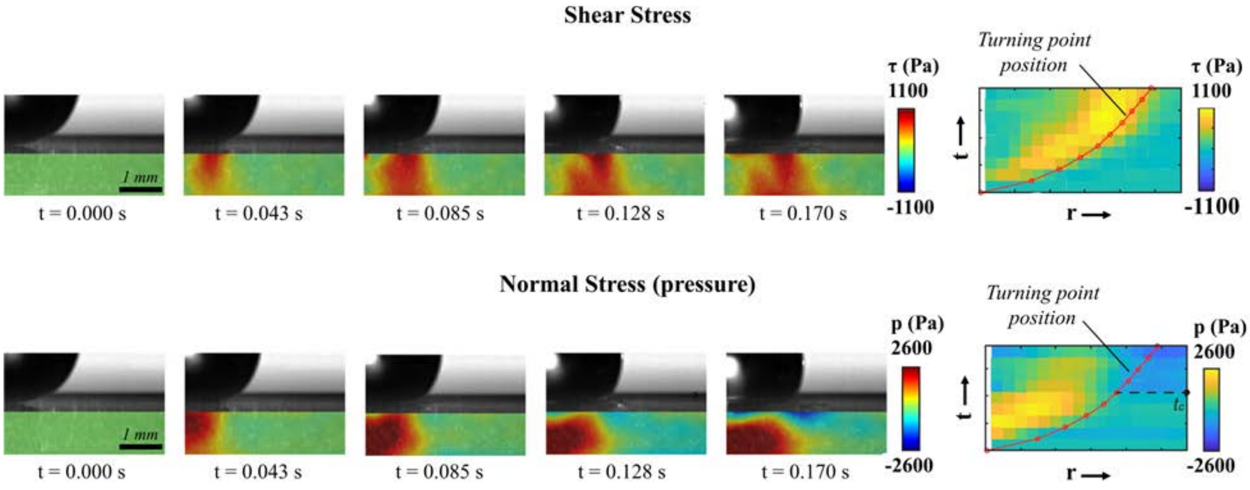

Fig. 14—Shear stress *(top)* and normal stress *(bottom)* distributions as a function of time for liquid droplet impact. Correlation of turning point location with stress maxima *(right)*. Droplet diameter was 3.49 *mm* and impact speed 2.97 m/s. Adapted from [51].

recovery. Unfortunately, there is no test facility available that can achieve all of these requirements and therefore compromises must be made when attempting to investigate erosion experimentally. Among the test approaches used in the literature, researchers have performed single drop impact testing using projectiles in ballistic ranges, rocket sled experiments where a specimen is accelerated to high speeds through a stream of droplets, and in-flight testing where an aircraft is flown through precipitating clouds. [15, 47] Each one of these experimental methods has advantages and limitations as outlined by Gohardani and should be used according to the desired level of evaluation (initial, extended, or complete) as recommended by Fields. [15, 47]

Among the limited experimental data publicly available, one study of interest was a rocket sled campaign performed at Holloman Air Force Base where erosion damage from high speed impacts of liquid and solid particles was done for an ablative material being screened for a radome. [48] The test specimen was accelerated by the sled to 655 m/s and collided head-on with water particles in liquid and solid phase with a diameter of 3 *mm*. Sample images of the surface craters induced by the impacts from both hydrometeors are shown in Figure 12. One of the key findings from that study was that water drops and ice particles of equal mass produced equivalent damage to the test sample.

Experiments like the sled test performed at Holloman Air Force Base provide valuable surface damage data which is useful to inform the material selection for a hypersonic vehicle. However, no insight regarding the liquid-solid interaction and the physical mechanism that drives the surface damage is available from those experiments or has been documented in the literature for hydrometeor impacts at hypersonic speeds.

Given the absence of that key information, perhaps a reasonable starting point is to at least describe the known physics of droplet impact at lower speeds from published research. The main mechanism known to play a key role in the initiation of surface erosion from low speed droplet impacts is lateral jetting as shown schematically in Figure 13. [44] Upon impact, a compressed liquid region is formed within the droplet and an expanding shock front propagates away from the contact zone. [44] Pressure release from that compressed region occurs through the lateral outflow or "jetting" of liquid parallel to the collision surface, a droplet feature known as the lamella. [44] For droplet impact velocities between 100 to 1140 m/s, spreading velocity measurements of the lamella as it emerges have been found to be several times the impact velocity as shown in Figure 13. [49, 50] The shear stress that results from this ejected fluid moving along the impact surface at high speeds is responsible for the onset of surface erosion. [44] Shear stress measurements of droplet impact have shown that the maximum shear stress propagates radially with the spreading lamella and its position correlates well with the position of the turning point [8]as shown in Figure 14. [51] Similar to the shear stress, the peak normal stress induced by an impacting droplet (peak impact pressure) also propagates radially with the spreading drop. [51] The key implication from these results is that the propagation of the shear and normal stress maxima act to "scrub" and "press" the contact surface causing damage. [51]

---

[8] The point within the droplet where the liquid flow direction changes from the -z direction (perpendicular to the contact surface) to the +r direction (radial direction parallel to the contact surface).

3. ASSESSMENT OF THE POTENTIAL FOR EROSION MEASUREMENTS IN WIND TUNNEL FACILITIES

Experimentally investigating encounters of hypersonic vehicles with atmospheric hydrometeors to evaluate surface erosion and its effect on aerodynamic performance is an extremely difficult task. The main challenge is accurately replicating the conditions of the encounter while simultaneously quantifying its effects. Unfortunately, no single hypersonic facility today can achieve this but different experimental approaches have been used by researchers, each with distinct advantages and limitations. Shock tubes for example have been employed to investigate breakup mechanisms of droplets and ice crystals in simulated shock layers but they cannot be used to study any type of particle-surface impact. High-speed projectiles striking hydrometeors in a gun range provide the most realistic simulation of the hypersonic encounter with a weather particle and have been used in surface erosion studies. However, projectile recovery after testing may result in additional and spurious surface degradation. Furthermore, no assessments can be made about the effect of erosion on the aerodynamic performance of the projectile. Finally, wind tunnel testing has the advantage of measuring aerodynamic performance of a body in a controlled setting and for a relatively long duration but generating the appropriate hydrometeor environment that will induce erosion in the first place is not trivial.

This research program initially proposed to use the brand new Naval Center for Space Technology (NCST) hypersonic wind tunnel to perform a set of experiments to characterize hydrometeor encounters with hypersonic vehicles and quantify the effect of surface erosion on aerodynamic performance. Prior to designing and conducting the wind tunnel tests, the implications and challenges associated with this experimental approach were carefully examined and the results of this effort are summarized next.

3.1 Preliminary Analyses

3.1.1 Artificial Hydrometeor Generation

Water vapor condensation occurring in the atmosphere can be simulated inside a supersonic or hypersonic wind tunnel to generate hydrometeors if it is operated with moist air as opposed to dry air. As the flow Mach number increases through the nozzle and the static pressure and temperature drop, the relative humidity[9] of the moist air increases rapidly and a state of high supersaturation is reached. [52] At this point, condensation in the flow ensues, but in contrast to the *heterogeneous* nucleation process that takes place high up in the atmosphere, condensation in a wind tunnel proceeds via *homogeneous* nucleation. This occurs because in comparison to air in the atmosphere, wind tunnel flows typically have a low concentration of impurities and therefore a reduced number of sites available as condensation nuclei. [11]

Condensation via homogeneous nucleation in a wind tunnel nozzle will produce particles with diameters between 0.1 and 20 μm. [48, 53] These particles are a few orders of magnitude smaller in comparison to raindrop sizes of interest for this study. The main challenge that arises when using a wind tunnel however is that the time scale of the high speed flow downstream of the nozzle is extremely short for these very small particles to grow and achieve raindrop sizes. Coagulation and gas-to-particle conversion processes responsible for transforming small cloud drops into precipitating ones in the atmosphere occur over length scales which are significantly larger. These processes are also facilitated by the effect of convection currents

---

[9] Relative humidity is defined as the ratio of the amount of water vapor present in air to the maximum amount of water vapor that can be contained by air at the same air temperature.

and large water contents in clouds which are obviously impossible to replicate in a wind tunnel. Generating liquid and solid hydrometeors in a wind tunnel test section with characteristic diameters between 0.5 - 2 *mm* is not possible through condensation alone and therefore an alternative strategy must be employed.

3.1.2 Artificial Hydrometeor Fluid Selection

Generating liquid hydrometeors in the test section of a cold hypersonic wind tunnel such as the NCST facility is not possible by simply injecting water into its settling chamber. Due to the low stagnation temperature of this facility ($\sim 295K$) and the adiabatic flow expansion that occurs through the nozzle, the flow reaches static temperatures at the test section that are well below the freezing point of water. Consequently, small water droplets that achieve thermal equilibrium with the flow cannot remain in liquid state and an alternative fluid must be used to generate *artificial* hydrometeors.

In order to select a water surrogate for this purpose, fluids must be screened based on their physical properties. First, the triple point temperature[10]of the fluid needs to be lower than the minimum static temperature reached by the flow to avoid the risk of freezing. Second, the normal boiling point[11]of the fluid needs to be used to evaluate the likelihood of the fluid existing in liquid phase as opposed to gaseous phase in the tunnel. If at atmospheric pressure the boiling point of the fluid is low, at the sub-atmospheric pressure conditions through the nozzle expansion and test section the boiling point will be even lower and the fluid might only exist in the gaseous phase. Fluids with normal boiling temperatures above the static temperature of the flow in the test section are therefore desired.

Assuming the flow Mach number for a set of wind tunnel experiments is in the 2 – 4 range, the static temperatures expected at the test section can be used to establish the ideal triple point temperature and normal boiling point requirements used for fluid screening. As shown in Table 3, the ideal fluid needs to have a triple point temperature below 68 *K* (flow static temperature at Mach 4) and a normal boiling point above 155 *K* (flow static temperature at Mach 2).

Table 3—Ideal screening requirements for fluid selection to produce artificial hydrometeors in wind tunnel.

Fluid Property	**Test Section Requirement**	**Desired Physical Behavior**
Triple Point Temperature	$< 68K$	Fluid will not freeze
Normal Boiling Point	$> 155K$	Fluid will not evaporate

To identify potential fluid candidates with the desired properties outlined above, a systematic fluid search was conducted through the extensive database of industrial substances compiled in REFPROP 10.0.[12]As part of this exercise, fluids were initially ranked based on their triple point and normal boiling point. Toxic, flammable, corrosive, health, and environmental hazards associated with the handling of these substances in a laboratory setting were also taken into consideration in the screening process.

From this analysis, no single fluid exists that full fills the fluid property requirements listed in Table 3 and does not pose a significant handling or operational hazard in a laboratory setting. Relaxing one constraint and considering fluids with triple point temperatures slightly above 68 *K*, two possible options are propane

---

[10] The triple point of a fluid is unique temperature and pressure condition at which liquid, solid, and gaseous phases exist in equilibrium.

[11] The normal boiling point is the temperature at which the vapor pressure of a liquid equals one atmosphere.

(85.5 *K*) and butene (87.8 *K*). Using these fluids does not necessarily imply droplet freezing is inevitable because liquid droplets being accelerated through the wind tunnel must be in thermal equilibrium with the flow at the test section for this to occur and thermal equilibrium may or may not be reached for a specific fluid depending on droplet size.

Without being able to ascertain the level of thermal equilibrium that may exist between propane or butene droplets and the wind tunnel flow, it is important to at least consider the worst case scenario which assumes equilibrium in order to predict what is the earliest in the wind tunnel flow path that freezing may occur. Similarly, on account of propane and butene being liquefied gases, it is also of interest to evaluate the possibility of flashing occurring upon injection into the stagnation tank of the wind tunnel and if that is the case, where along the flow path gaseous propane will liquefy.

For this purpose, the static pressure and temperature flow conditions of the wind tunnel obtained using a quasi-one-dimensional analysis and assuming a stagnation temperature of 300 *K* for a Mach 2 and 4 test section were superimposed on a phase diagram for propane and butene obtained from REFPROP 10.0. The results from this exercise in Figures 15 and 16 show how for a Mach 2 flow, both propane and butene would indeed flash upon injection into the wind tunnel given the stagnation tank pressure-temperature conditions. However, as the flow expands through the nozzle and both temperature and pressure drop, liquefaction would occur prior to reaching the test section. For the Mach 4 flow conversely, none of these candidate fluids would flash inside the stagnation tank but both fluids would reach their triple point approximately 2 *m* upstream of the test section.

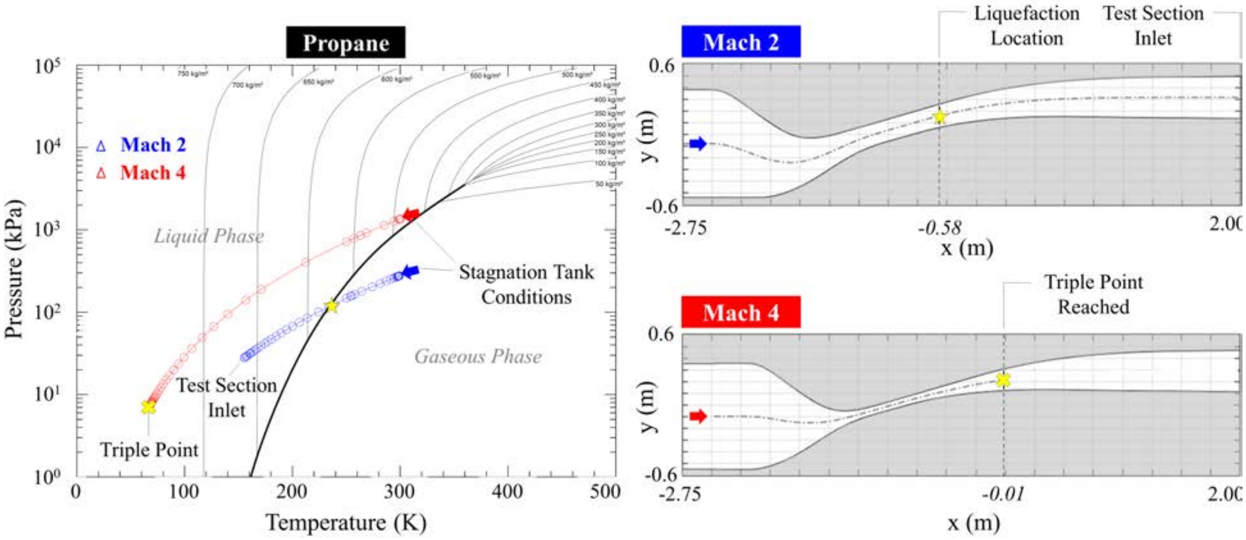

Fig. 15—Pressure-temperature flow conditions through the NCST hypersonic wind tunnel for Mach 2 and Mach 4 overlaid on a propane phase diagram (*left*). Locations along the Mach 2 and Mach 4 flow paths where propane fluid would reach liquefaction or solidification assuming thermal equilibrium with the flow (*right*).

As a final comment on fluid selection, from the experimental setup standpoint, propane and butene are commercially available liquefied gases that aside from being flammable, are not toxic or corrosive. Propane however has a higher vapor pressure at room temperature so it is typically stored at a much higher pressure [54]. This is extremely advantageous when designing a liquid delivery system that would be necessary to

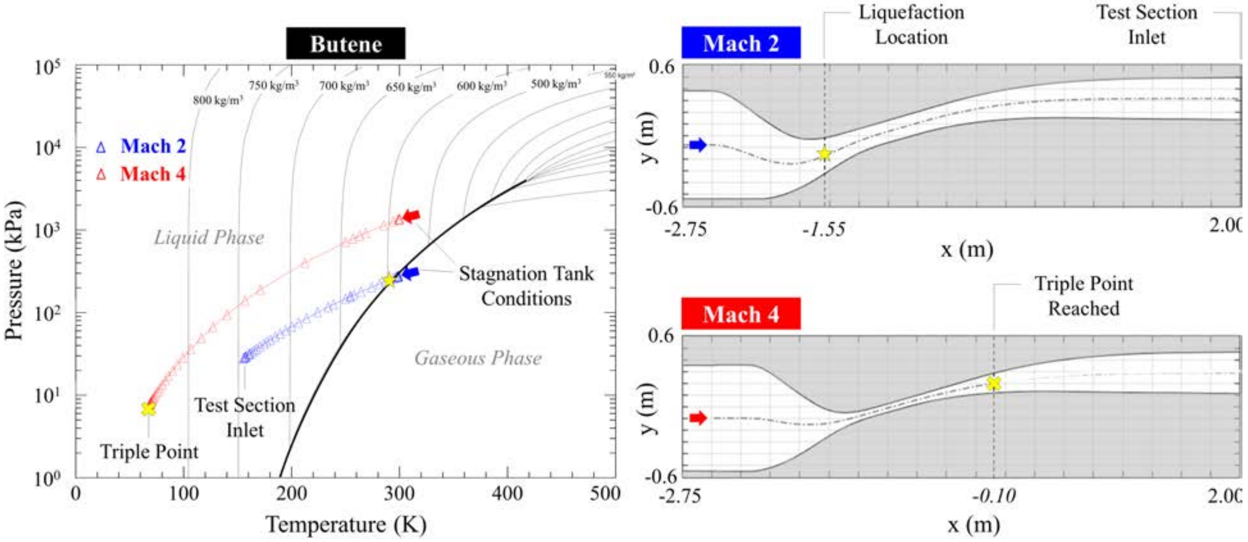

Fig. 16—Pressure-temperature flow conditions through the NCST hypersonic wind tunnel for Mach 2 and Mach 4 overlaid on a butene phase diagram (*left*). Locations along the Mach 2 and Mach 4 flow paths where butene fluid would reach liquefaction or solidification assuming thermal equilibrium with the flow (*right*).

seed the wind tunnel airflow. Preliminary flammability calculations not presented here have shown that the maximum propane injection flow rates required for the experiments correspond to 24 - 40% of the necessary flow rates required to achieve mixture concentrations at 50% of the Lower Flammability Limit (LFL). These results demonstrate that propane injection into the wind tunnel would not pose a flammable hazard for the facility.

---

[12] Reference Fluid Thermodynamic and Transport Properties (REFPROP) is a computer program and database developed by the National Institute of Standards and Technology (NIST) to provide thermophysical properties for a variety of industrial fluids over a wide range of conditions and fluid phases.

[13] PubChem is an open chemistry database at the National Institutes of Health (NIH) that collects scientific data from government agencies, chemical vendors, and journal publishers.

3.1.3 Hydrometeor Velocity Deficit and Droplet Survival

Simulating hydrometeor encounters with a hypersonic vehicle using a wind tunnel facility requires accelerating liquid or solid particles to vehicle flight speeds before they collide with a stationary model. Calculations of particle drag acceleration performed by researchers have shown that having particles achieve free stream speeds would require prohibitively long flow paths upstream of the test section that no practical facility can accommodate. [48, 55] Consequently, for a typical wind tunnel, drag accelerated particles are expected to have a significant velocity deficit upon reaching the test section. Quantifying that deficit is important prior to performing any experiments.

Drag acceleration of particles in a hypersonic wind tunnel can be analytically predicted if the particles are assumed to be small solid spheres that do not rotate or interact with one another as they are accelerated. Under these assumptions, viscous effects dominate the kinetic behavior of the particles and their acceleration profile can be computed by solving the following differential equation, which is a result of applying Newton's Second Law of motion to a particle subjected to aerodynamic forces. [48]

$$\frac{dU_p}{dt} = \frac{3}{4} C_D \frac{\rho_\infty}{\rho_p} \frac{1}{D_p} (U_\infty - U_p)^2 \tag{18}$$

where

C_D	is the particle drag coefficient
ρ_p	is the particle density
D_p	is the spherical particle diameter
U_p	is the particle velocity
ρ_∞	is the flow density
U_∞	is the flow velocity.

Several expressions have been proposed in the literature to model the drag coefficient C_D of a spherical particle in Eq.(18). [56–59] One of the most recent works on this topic was performed by Loth who developed and validated a model for the drag coefficient of spherical particles in flow regimes dominated by compressibility ($Re_p > 45$) or rarefaction ($Re_p < 45$), where Re_p is the Reynolds number based on particle diameter. [59] Using Loth's model for the C_D and the flow properties along the flow path of the NCST hypersonic wind tunnel calculated with a quasi-1D analysis for a Mach 4 condition, Eq.(18) was integrated between the stagnation tank and the test section using four sample particle sizes to predict particle velocity as a function of axial location.

Figure 17 (*center*) shows a comparison of the calculated flow speed and the expected particle velocities. Note that the smallest particle size considered in this analysis corresponds to the reference diameter for the smallest possible raindrop and the largest corresponds to the typical raindrop diameter as presented earlier in this report. The results clearly show how the particles accelerate through the Mach 4 flow path but none of them reach the flow speed at the wind tunnel test section. Figure 18 (*left*) shows particle velocity deficit as a percent of the flow speed at the test section for the four droplet sizes modeled. As expected, note how the velocity deficit increases with increasing particle size and ranges between 7 - 38% in this analysis.

The main implication of particles lagging the wind tunnel flow is that the collision speed simulated in the experiments will be lower in comparison to the actual collision speed with a vehicle in flight. A slower moving particle will have a lower kinetic energy which decreases its erosion potential upon impact. As a result, for a single impact with a test model, any surface erosion occurring in a wind tunnel environment will underestimate the actual damage that may occur on a flight system.

Particles with large velocity deficits used to simulate collisions with hypersonic bodies in a wind tunnel are certainly problematic, however, another issue of commensurate experimental complexity is having droplets with sizes of interest *survive* the drag acceleration process and reach the test section. This is due to the fact that droplets undergoing acceleration are prone to breakup which is governed by the Weber number as described earlier in this report.

For water droplets introduced upstream of the nozzle and into the settling chamber of the NCST hypersonic wind tunnel, Figure 17 (*bottom*) displays the calculated Weber number as a function of axial location obtained using local flow properties and assuming a constant surface tension value of 0.075 N/m at 0.01 °C (value at the lowest possible temperature before freezing obtained from REFPROP 10.0). Figure 18 (*right*) summarizes the peak Weber numbers for the four droplet sizes considered in this analysis.

From the results in these figures, note how the maximum Weber number experienced by the water droplets is expected near the throat of the Mach 4 flow path (the dip observed just upstream of the throat is a non-physical numerical artifact of the solution discretization). More importantly however, note from Figure 18 (*right*) that the peak Weber number for droplets in the 0.1 - 2.0 *mm* range significantly exceeds the critical Weber number for breakup mentioned in a previous chapter of this report ($We_c = 12$).

This analysis therefore demonstrates that breakup is inevitable in a Mach 4 wind tunnel flow for droplets in the 0.1 - 2.0 *mm* range and that it is expected to occur early on in the flow path upstream of the test section. It is unknown however if complete demise of the initial droplets will occur before reaching the test section or if any children droplets that result from the break up process may survive. If the latter were to occur however, the size of those surviving droplets may not be relevant anymore for the study of hydrometeor-induced surface erosion.

3.1.4 Aerothermal Heating

Hypersonic glide vehicles are exposed to very intense aerothermal loads during flight that to this day continue to challenge the design of thermal protection systems. The boundary layer along the vehicle surface is very hot due to the high-kinetic energy of the hypersonic flow entering this layer and slowing down by viscous effects [60]. The gas within the shock layer but outside the surface boundary layer reaches very high temperatures due to shock-wave heating [60]. Heat transfer from both the extremely hot boundary layer and shock layer to the cooler vehicle body occurs through thermal conduction and radiation, increases with the cube of flight velocity, and causes extremely high surface temperatures specially for vehicle leading edges. [60]

From the surface erosion perspective, high surface temperatures will affect the mechanical properties of the materials which in turn influence the damage level suffered by the vehicle. [55] Ideally, a wind tunnel facility

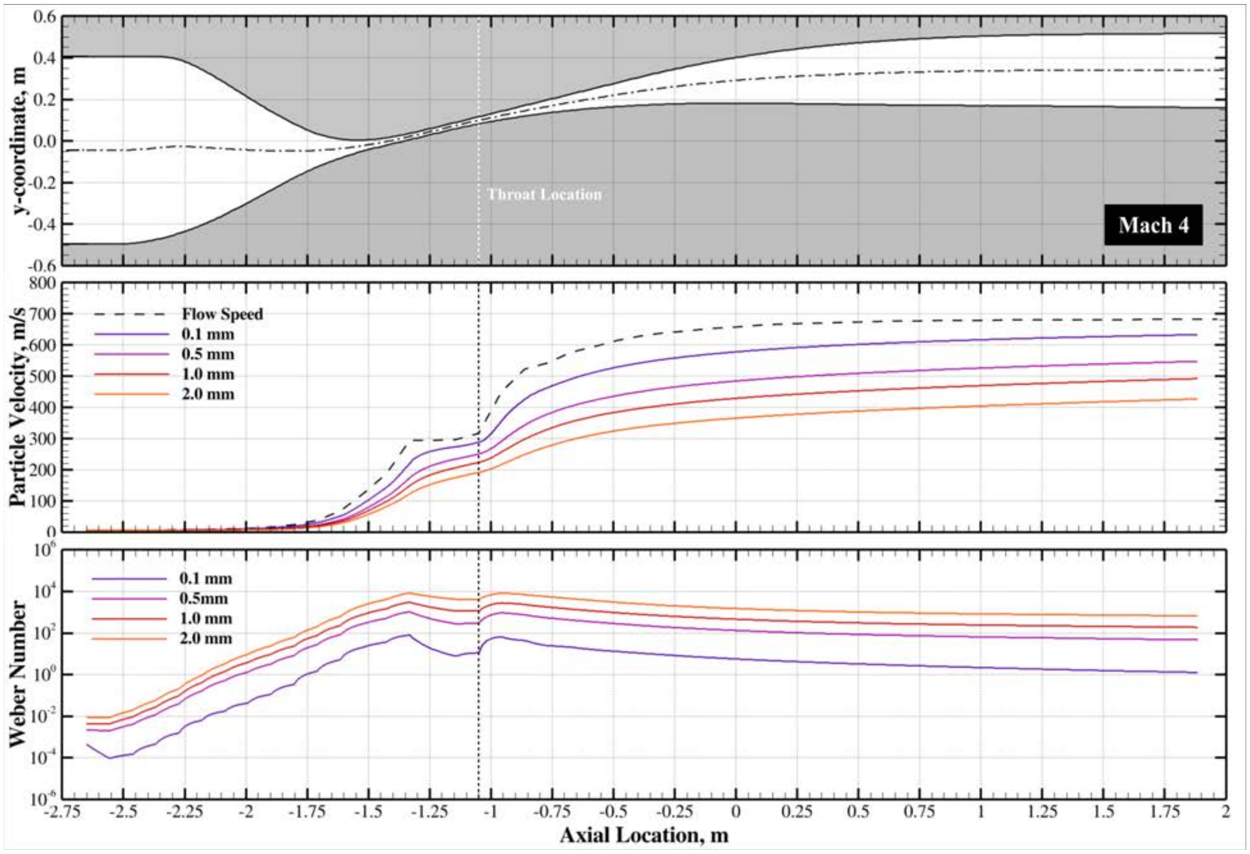

Fig. 17—NCST hypersonic wind tunnel flow path for Mach 4 flow *(top)*, particle velocity as a function of wind tunnel flow path axial location for various droplet sizes *(center)*, Weber number as a function of wind tunnel flow path axial location *(bottom)*.

used to generate the artificial erosive flight environment should simultaneously provide the high enthalpy flow conditions to simulate test specimen heating. This is not possible with the NCST hypersonic wind tunnel and therefore any model erosion assessment made from experimental results obtained in this facility must keep that in mind.

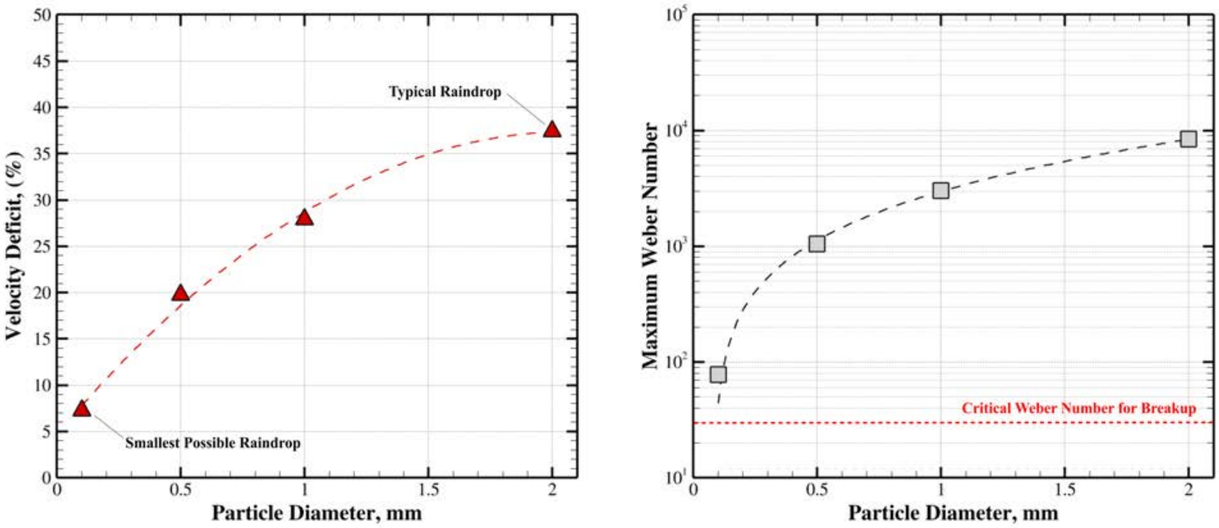

Fig. 18—Droplet velocity deficit at test section for Mach 4 flow (*left*), maximum Weber number through wind tunnel flow path for different droplet sizes (*right*).

3.2 Path Finding Experiments

Given the numerous challenges of using a wind tunnel facility to test collisions of artificial hydrometeors (droplets) with a hypersonic vehicle as discussed above, it was important to conduct a preliminary set of rapid experiments that could help de-risk the proposed NCST hypersonic wind tunnel tests as well as inform their design. Specifically, it was critical to verify artificial hydrometeors could be generated by injecting propane into the settling chamber of the wind tunnel and furthermore whether or not those droplets would survive and make it to the wind tunnel test section.

3.2.1 Experimental Setup

The prototype experiments were performed using a small scale replica of the NCST hypersonic wind tunnel, designed to generate Mach 2-4 flows in a test section with a height of 1.9 *in* and width of 1.6 *in* (roughly 2% of the NCST hypersonic wind tunnel test section area). Figure 19 shows a side view of this small scale wind tunnel assembled to its settling chamber. Just like its large NCST counterpart, the lower nozzle block of this tunnel slides back an forth to vary the test section Mach number by changing the throat size. For the set of experiments performed with this tunnel, the flow condition of interest was Mach 3.5 based on the notional vehicle trajectory discussed earlier in this report.

To supply high pressure air to the small scale wind tunnel for its operation, one of the 2800-gallon air tanks for the NCST hypersonic wind tunnel was pressurized using a SpeedAire compressor connected to an Ingersoll Rand air dryer. The tank was plumbed to the wind tunnel and a remotely activated Bonomi pneumatic valve was used to initiate the air flow for the experiments. Figure 20 shows a picture of this setup.

To seed the airflow for the tests and generate droplets, a propane injection system originally designed to be used with the large NCST hypersonic wind tunnel was modified to use water and integrated to the settling

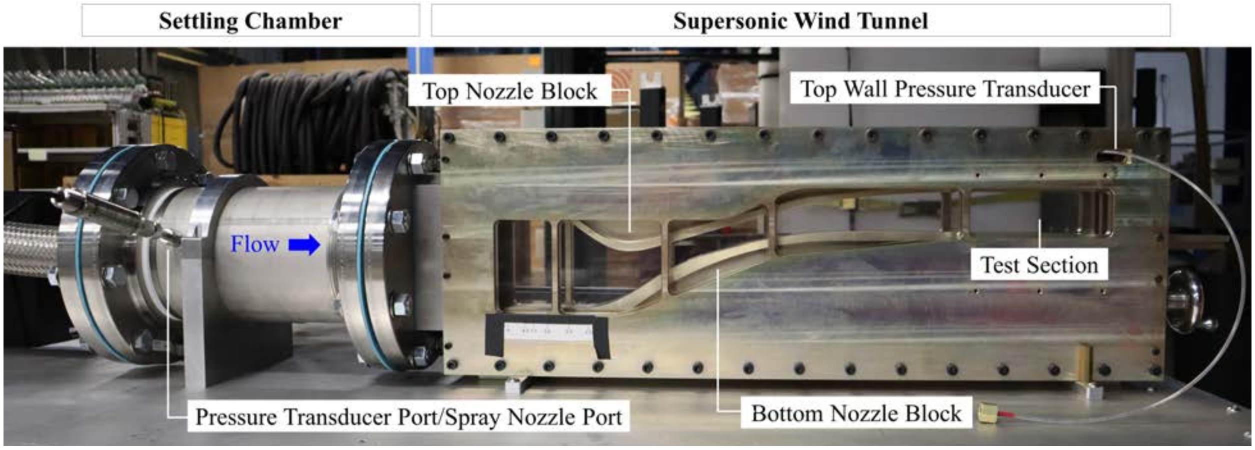

Fig. 19—Small scale wind tunnel used in path finding experiments.

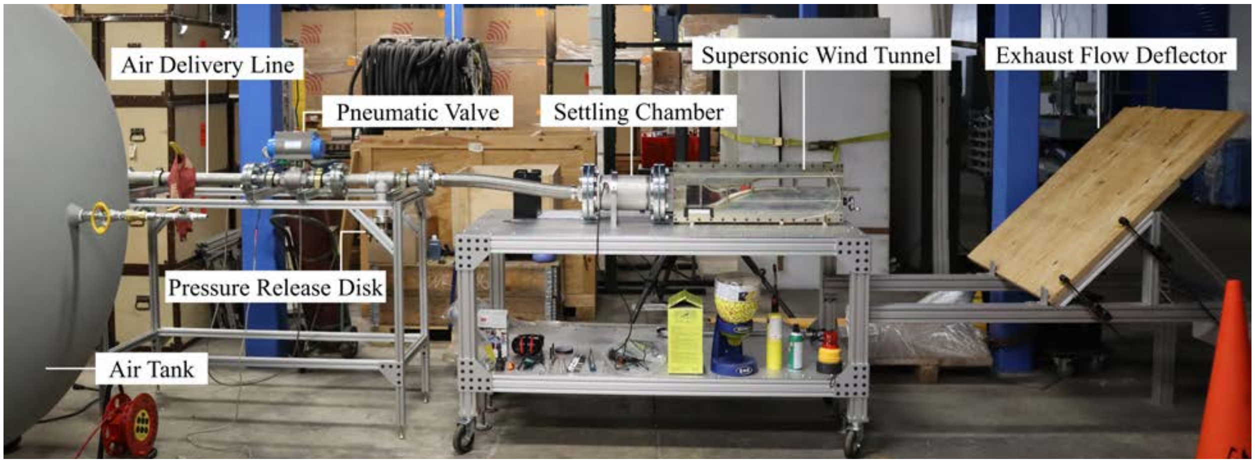

Fig. 20—Air supply system components and connection to the small scale wind tunnel.

chamber of this small scale wind tunnel. This fluid delivery system consisted of a 2.25 L high pressure cylinder used to store water, a nitrogen bottle used to pressurize the cylinder, and a spray nozzle connected to the cylinder with a high pressure braided hose. Figure 21 shows pictures of this system integrated to the settling chamber of the small scale wind tunnel.[14]

For the experiments, pressure measurements of the wind tunnel settling chamber and test section plus digital photography and shadowgraph imaging were used. The pressure measurements were used to verify the actual Mach number achieved at the test section of the wind tunnel. The optical diagnostics were used to visually corroborate the presence of droplets in the flowfield.

---

[14] Additional details about the experimental setup plus information regarding the test approach and methodology can be found in an internal document titled *Small Scale Wind Tunnel Test Description and Procedure*. A copy of this document can be requested by emailing Camilo Aguilera at camilo.aguilera@nrl.navy.mil.

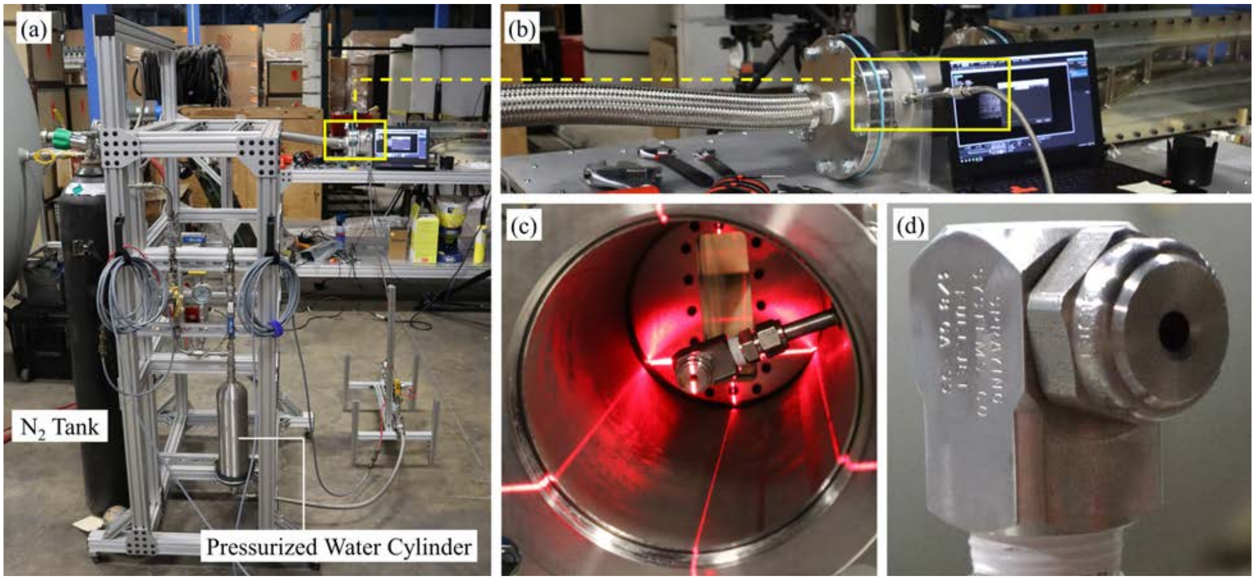

Fig. 21—Water delivery system for small scale wind tunnel. (a) Cart with nitrogen pressurization setup for water cylinder, (b) Connection to wind tunnel settling chamber, (c) View of spray nozzle inside settling chamber (flow facing for laser alignment with chamber center line), (d) Spray nozzle detail view.

3.2.2 Test Results and Discussion

There were unforeseen experimental difficulties encountered with the operation of the small scale wind tunnel which unfortunately prevented achieving the objectives set for these tests. However, several lessons were learned through this effort that should be documented to serve as a reference for other researchers that may want to use the small scale wind tunnel in the future.

Pressure Losses

As mentioned earlier, one of the NCST hypersonic wind tunnel air tanks was pressurized and connected to the small scale wind tunnel to operate it. Moving that large tank next to the SpeedAir compressor in building A-59 was not possible for the experiments due to its size and weight. As a result, a long hose had to be used to connect the tank to the compressor/dryer assembly which were approximately 100 ft away. Due to this, there was a significant pressure loss through the hose and the maximum air pressure achieved at the tank using the compressor was 125 $psia$. For the Mach 3.5 condition of interest for the tests, the minimum viable stagnation pressure required was 120 $psia$ at the wind tunnel settling chamber. Stagnation pressure measurements at the settling chamber through the side port shown in Figure 19 revealed an additional pressure loss through the air line connecting the tank to the tunnel chamber. Due to the low initial tank pressure and the additional losses through the delivery piping, the wind tunnel was not able to start. This was verified with static pressure measurements and shadowgraph visualizations of the test section which indicated the presence of subsonic flow at that location of the flow path.

Wind Tunnel Flow Quality

When it became apparent that the flow was subsonic at the test section, a set of additional experiments were performed to determine if the flow was supersonic anywhere upstream. If that were to be the case, maybe that section of the flow path could be used as a proxy test section. For this purpose, shadowgraph images of the flow were captured at a few locations downstream of the throat.

The results of this exercise showed that the flow was indeed supersonic but only for a short segment of the flow path and the flow quality was very poor as shown in Figure 22. Severe leaking from improper sealing between the tunnel windows and the lower nozzle block allowed high pressure air from upstream of the throat to enter into the flow path downstream and disturb the low pressure supersonic flow. Figure 23 shows a picture of the large gaps responsible for this and the leak path observed in the experiments. Unfortunately, those gaps between the lower nozzle block and the windows are a fundamental design flaw that has no other way of being corrected aside from machining a brand new, wider nozzle block with an o-ring groove.

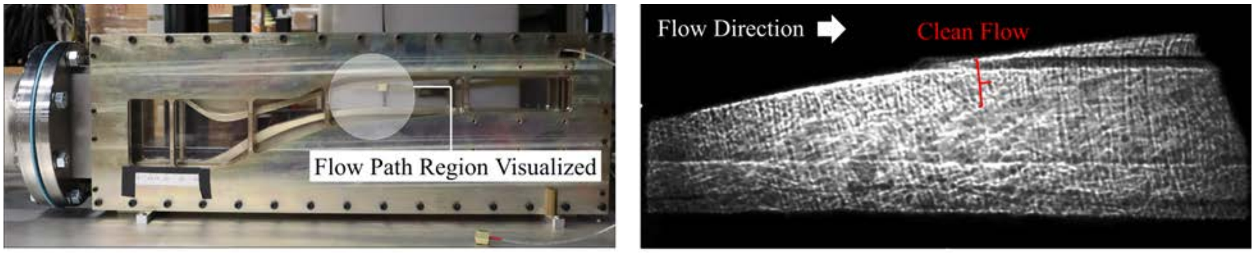

Fig. 22—Highlighted flow path region visualized using shadowgraphy upstream of the actual wind tunnel test section *(left)*, sample shadowgraph of wind tunnel flow highlighting a clean supersonic flow region observed only along the top nozzle block with subsonic flow everywhere else *(right)*. Very poor image quality observed due to plexiglass windows of small scale wind tunnel.

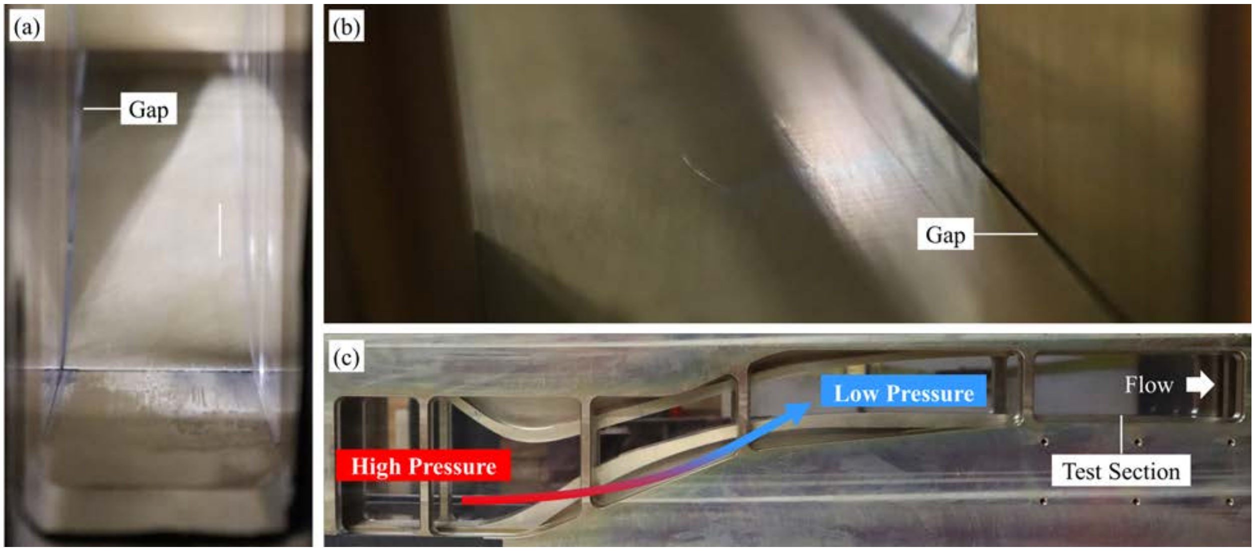

Fig. 23—Large gaps between lower nozzle block and small scale wind tunnel windows: (a) Gap seen from the wind tunnel inlet upstream of the throat, (b) Gap observed near the test section exit, (c) Leak path of high pressure air upstream of tunnel throat into low pressure region downstream responsible for heavily disturbing flow as seen in Figure 22.

Obscured Flow Visualizations

Prior to performing any wind tunnel experiments, the spray nozzle was tested offline using different back pressures to qualitatively characterize droplet size, measure spray angle, and determine injection timing.

These preliminary experiments were useful to select the operating pressure for the spray nozzle and inform the test procedure to be followed when the fluid delivery system was integrated and tested with the small scale wind tunnel.

Despite these preliminary efforts and after multiple injection experiments where nozzle back pressure and injection duration were reduced, for every single test run performed, the wind tunnel windows were soaked with water and no flow visualization was possible.

This result was not absolutely unexpected because the spray nozzle used had been originally sized (in terms of flow rate and spray characteristics) for the large stagnation chamber of the NCST hypersonic wind tunnel, which is significantly larger than the 6-in chamber of the small scale wind tunnel. Sample pictures of the wind tunnel before and right after the injection of water are shown in Figure 24.

3.2.3 Final Comments

Failure to de-risk the NCST hypersonic wind tunnel test campaign planned with the small scale wind tunnel experiments, combined with the ongoing installation delays of the new wind tunnel facility and the increasing likelihood of its commissioning occurring very close to the end of the program, forced the team to re-vector the experimental approach and look for alternative ways to obtain the requisite data. These strategies will be summarized in Chapters 6 and 7.

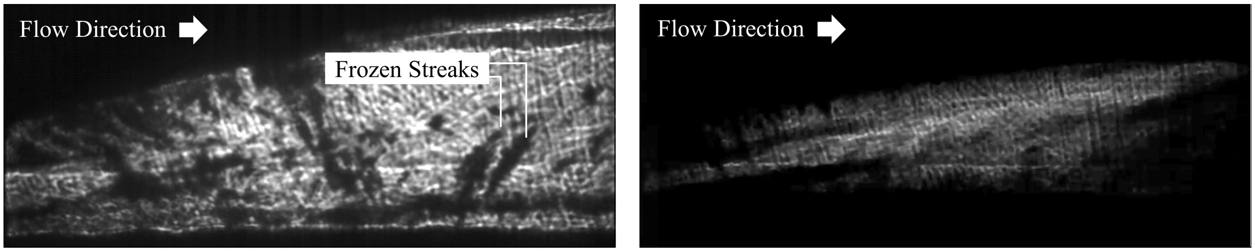

Fig. 24—Sample images of obscured flow visualization with water injection: (a) Streaks of frozen water appearing on the wind tunnel windows during a test from water that remained in the flow path from a previous run, (b) Significantly obscured flow visualization occurring with spray nozzle operation.

4. DROPLET TRAJECTORY AND DEMISE PREDICTION

The flow between the leading shock and the body of a supersonic or hypersonic vehicle has a strong interaction with cloud drops and raindrops that is fundamental to the study of droplet-induced erosion. Due to their small size, cloud drops can evaporate, undergo significant deceleration, or conform to the local streamlines in this shock layer and may never reach the surface of the vehicle. [61] The erosion potential of these small drops is therefore likely low and the shock layer effectively acts as a shield. Conversely, larger raindrops undergo a complex break-up process involving mass stripping and shattering as they transit through the shock layer but may still impact the vehicle and inflict damage. [61] Accurately predicting the erosion potential of raindrops therefore presents unique difficulties because it requires understanding this droplet/shock layer interaction to properly determine the terminal size and velocity of the droplet or its fragments before impact.

Five different modes of droplet breakup have been observed experimentally. The dynamics of these breakup processes are driven by aerodynamic forces and can be divided into regimes based on the droplet Weber number as described earlier in Chapter 2. Numerous breakup models have been proposed but typically they prove to be accurate only in a select set of regimes with no model effectively covering the whole range. Common models in the low *We* regimes of oscillation and bag include the TAB, NTAB, Clark, and DDB models. These start to breakdown in the multimode regime and above where models such as the Kelvin-Helmholtz and Rayleigh-Taylor wave models must instead be employed [62–70].

Complex flow fields around hypersonic bodies present a particular challenge as droplets will be exposed to diverse and rapidly varying Weber numbers such as when passing through a bow shock region. Correlation-based demise models, such as those given in Eqs. (10) – (11) have been calibrated using data obtained in shock tubes in which the post-shock conditions are constant and may not accurately reflect the interaction with more realistic flow fields. Thus, it is of interest to understand how the breakup models mentioned in the preceding paragraph, that are sensitive to variations in the local flow environment, behave under canonical conditions representative of a hypersonic body in the terminal phase of its flight trajectory.

To accomplish this task, we have implemented a coupled Lagrangian-Eulerian multiphase simulation algorithm within the JENRE® Multiphysics Framework that is capable of producing high-fidelity predictions of the hypersonic flow fields generated by arbitrary body shapes. We use this tool to evaluate the performance of several dynamic aerodynamic droplet breakup models for computing the demise of droplets caused under variable high-Mach number conditions.

4.1 Simulation Methodology

4.1.1 Eulerian Gas-Phase Model

The gas-phase flow field is governed by the Navier-Stokes equations for a multi-component gas,

$$\frac{\partial C_i}{\partial t} + \nabla \cdot (C_i \mathbf{u}) = \nabla \cdot (\mathscr{D}_i \nabla Y_i) + S_{C_i}, \tag{19}$$

$$\frac{\partial \rho \mathbf{u}}{\partial t} + \nabla \cdot (\rho \mathbf{u}\mathbf{u} + P) = \nabla \cdot \tau + S_{\text{mom}}, \tag{20}$$

$$\frac{\partial \rho E}{\partial t} + \nabla \cdot ((\rho E + P)\mathbf{u}) = \nabla \cdot (\tau \mathbf{u} + \mathbf{q}) + S_{\text{energy}}, \tag{21}$$

where the total gas-phase density $\rho = \sum_i C_i W_i$ is the sum of the partial densities of the constituent gas species, and C_i and W_i are the molar concentration and molecular weight, respectively, of the i^{th} species. The total energy of the gas mixture is the weighted sum of the internal energies of the species e_i and the kinetic energy of the gas according to $\rho E = \sum_i C_i W_i e_i + 1/2\rho|\mathbf{u}|^2$, where $\mathbf{u}$ is the gas-phase velocity. We assume that the gas is a mixture of thermally-perfect gases with temperature-dependent thermodynamic properties, and the pressure P can be related to the temperature T according to the ideal gas law. We use the standard Newtonian viscous stress tensor $\tau = \mu \left(\nabla\mathbf{u} + (\nabla\mathbf{u})^T - 2/3\nabla\cdot\mathbf{u}\right)$ and Fourier heat-flux vector $\mathbf{q} = -\kappa\nabla T$. Transport coefficients (μ, κ, and $\mathscr{D}_i$) are mixture-averaged values computed using standard models [71–73]. The source terms S_{C_i}, S_{mom}, and S_{energy} represent the exchange of mass, mixture-averaged momentum, and mixture-averaged energy between the gas-phase and the liquid droplet phase. These source terms will be defined in the following section.

4.1.2 Lagrangian Droplet Model

Droplets are modeled as point particles governed by the Newtonian laws of motion,

$$\frac{d\mathbf{X}_i}{dt} = \mathbf{V}_i \tag{22}$$

$$m_i\frac{d\mathbf{V}_i}{dt} = \mathbf{F}_i \tag{23}$$

where $\mathbf{X}_i$, $\mathbf{V}_i$, and m_i are the position, velocity, and mass of droplets i. For the flow conditions of interest, we assume that aerodynamic drag is the predominant force acting on the droplets, such that $\mathbf{F}_i = \mathbf{F}_{\mathrm{D}_i}$, where

$$\mathbf{F}_{\mathrm{D}_i} = \frac{1}{2}C_{Di}\frac{\pi d_i^2}{4}\rho\left(\mathbf{u} - \mathbf{V}_i\right)|\mathbf{u} - \mathbf{V}_i|. \tag{24}$$

Droplet Drag

To determine the drag coefficient, C_D, of the droplet we consider three varieties of drag models: drag on rigid spheres, drag in conjunction with time resolved droplet deformation, and rigid sphere drag with additive correction.

Rigid Sphere: Here we consider drag on a rigid sphere, ignoring the effect that droplet deformation has on the local flow field and the resulting hydrodynamic forces. The correlation appears as,

$$C_{D,\text{sphere}} = 0.36 + 5.48\text{Re}^{-0.573} + \frac{24}{\text{Re}} \tag{25}$$

and is purely a function of the droplet Reynolds number,

$$\text{Re} = \frac{\rho\mathbf{V}_i D_{o,i}}{\mu}. \tag{26}$$

Time Resolved Distortion: The droplets are assumed to be deformable oblate spheroids with cross-stream diameter D_c and mean spherical diameter D_o. We assume the drag between the droplet and background gas is a function of the droplet distortion defined as $y = D_c/D_o$ with aspect ratio $\eta = 1/y^3$ by allowing the drag coefficient to vary between that of a rigid sphere for a perfectly spherical droplet ($y = 1$) and that of a disk in the limit of large distortion ($y >> 1$),

$$C_D = fC_{D,\text{disk}} + (1-f)C_{D,\text{sphere}}. \tag{27}$$

The interpolation variable f is defined as $f = 1 - \eta^2$, and we use the correlation for a rigid sphere from above and the correlation,

$$C_{D,\text{disk}} = 1.1 + \frac{64}{\pi Re} \tag{28}$$

for disks [70].

Additive Correction: Instead of using a time resolved distortion, another option is to employ a corrective addition to the standard rigid sphere drag,

$$C_D = C_{D,\text{sphere}} + C_{D,\text{def}}. \tag{29}$$

Here the corrective term, $C_{D,\text{def}}$, is a function of droplet Weber number (We),

$$\text{We} = \frac{\rho\, |\mathbf{u} - \mathbf{V}_i|^2 D_{o,i}}{\sigma}, \tag{30}$$

and is,

$$C_{D,\text{def}} = \text{We}\left(0.2319 - 0.1579\log \text{Re} + 0.047\log^2 \text{Re} - 0.0042\log^3 \text{Re}\right), \tag{31}$$

as proposed by Wiegand [74]. The Weber number provides information about the forces acting upon the droplet allowing for a quasi-steady estimate of the droplet's distortion.

Droplet Breakup

The droplets are allowed to undergo discrete aerodynamic breakup events during which the parent droplet spawns a single or multiple child droplets. As discussed in the Introduction, a variety of models exist that are capable of describing this phenomena over various droplet Weber number regimes. In this work, we are concerned only with large-Weber-number phenomena and focus our primary attention to those models considered to be generally applicable in that flow regime.

Upon a breakup event, child parcels are initialized with the same temperature as the parent droplet at a random location within a shell between D_o and $2D_o$ from the center of mass of the parent droplet. A small random velocity perturbation is applied in the plane normal to the trajectory of the parent droplet, and the parent mass and momentum are adjusted to ensure conservation.

Taylor Analogy Breakup (TAB): The original Taylor Analogy Breakup (TAB) model, proposed by O'Rourke and Amsden [75], is a time resolved ODE that predicts a droplet deformation parameter. The aerodynamic force driving the deformation is counteracted by the restoring tendency of surface tension and viscous damping. As formulated by Schmehl [70] the governing equation for the deformation, y, appears as

$$\frac{\mathrm{d}^2 y}{\mathrm{d}\bar{t}^2} = -20\mathrm{Oh}\frac{\mathrm{d}y}{\mathrm{d}\bar{t}} - 64\,(y-1) + 2C_{2,\mathrm{TAB}}\mathrm{We}. \tag{32}$$

The droplet Ohnesorge number (Oh) is defined according to

$$\mathrm{Oh} = \frac{\mu_l}{\sqrt{\rho_l D_{o,i}\sigma}}, \tag{33}$$

where the subscript l denotes properties of the liquid droplet, $\bar{t} = t/t^*$ is the non-dimensional time variable, and σ is the surface tension at the gas-liquid interface. Equation (32) is non-dimensionalized by the characteristic time of free shape oscillations $t^* = (D_o^3\rho_l/\sigma)^{1/2}$, and the model constant $C_{2,\mathrm{TAB}} = 2/3$ as defined in the original TAB model.

In this formulation breakup is assumed to occur when the deformation reaches a critical value of $y_{c,\mathrm{TAB}} = 1.5$. The parent droplet completely breaks up into multiple child droplets with a Sauter mean diameter determined by an energy conservation model proposed by O'Rourke and Amsden [75].

Non-linear Taylor Analogy Breakup (NTAB): For large deformations, the assumption of linear perturbations to the droplet surface used in the derivation of the TAB model breaks down. Schemhl [70] proposed a non-linear model of a droplet oscillating between an oblate and prolate spheroid,

$$\frac{\pi^2 + \frac{16}{y^6}}{\pi^2 + 16}\frac{\mathrm{d}^2 y}{\mathrm{d}\bar{t}^2} = \frac{48}{\pi^2+16}\left(\frac{\mathrm{d}y}{\mathrm{d}\bar{t}}\right)^2 - 40\mathrm{Oh}\frac{1}{y^2}\frac{\mathrm{d}y}{\mathrm{d}\bar{t}} - 20\frac{1}{S_0}\frac{\mathrm{d}S}{\mathrm{d}y} + \frac{2C_{2,\mathrm{NTAB}}}{y}\mathrm{We}, \tag{34}$$

where $C_{2,\mathrm{NTAB}} = C_{2,\mathrm{TAB}} = 2/3$. The rate of surface change can be approximated by,

$$\frac{1}{S_0}\frac{\mathrm{d}S}{\mathrm{d}y} = \begin{cases} 9.98y^3 - 30.34y^2 + 33.94y - 13.58, & 0.5 < y < 1, \\ 0.67y^3 - 4.01y^2 + 9.21y - 5.67, & 1 \le y < 2.3, \end{cases} \tag{35}$$

or directly calculated from the respective expressions for surface area. Here the critical value of deformation is $y_{c,\mathrm{NTAB}} = 1.8$ which predicts breakup under identical flow conditions that result in $y_{c,\mathrm{TAB}} = 1.5$.

Kelvin-Helmholtz (KH/Wave): In the Kelvin-Helmholz (KH) wave stripping theory [76] droplets are continuously shed from a deformed parent droplet based on perturbations caused by the most unstable KH wavelength on its surface,

$$\Lambda_{\mathrm{KH}} = \frac{9.02D_o\,(1+0.45\mathrm{Oh})\left(1+0.4\mathrm{Ta}^{0.7}\right)}{2\left(1+0.865\mathrm{We}^{1.67}\right)^{0.6}} \tag{36}$$

with corresponding growth rate,

$$\Omega_{\mathrm{KH}} = \sqrt{\frac{8\sigma}{\rho_l D_o^3}}\frac{0.34+0.38\mathrm{We}}{(1+\mathrm{Oh})\left(1+1.4\mathrm{Ta}^{0.6}\right)}, \tag{37}$$

where the Taylor number is defined as $\mathrm{Ta} = \mathrm{Oh}\sqrt{\mathrm{We}}$ and We and Oh are defined based on the droplet radius. The child droplet fragment mass shed from the parent droplet, m_f, is assumed to vary continuously according to

$$\frac{\mathrm{d}m_f}{\mathrm{d}t} = -\frac{4\pi\rho_l r_o^2 (r_o - r_c)}{\tau_{\mathrm{KH}}} \tag{38}$$

where $r_o = D_o/2$ is the radius of the parent droplet, $r_c = B_0\Lambda_{\mathrm{KH}}$ is the radius of the child droplets, and $\tau_{\mathrm{KH}} = 3.726 B_1 r_o/\Omega_{\mathrm{KH}}\Lambda_{\mathrm{KH}}$ is the time constant associated with fragmentation. In our implementation of the model, parcels of child droplets are released from the parent droplet when the collected mass exceeds 2% of the parent mass.

Rayleigh Taylor (RT): The Rayleigh-Taylor (RT) breakup model assumes that the growth of RT waves on the surface of the droplet will eventually lead to breakup [77]. The growth rate of the fastest growing wavelength is,

$$\Omega_{\mathrm{RT}} = \sqrt{\frac{2}{3\sqrt{3\sigma}} \frac{[a(\rho_l - \rho)]^{3/2}}{\rho_l + \rho}}, \tag{39}$$

where a is the magnitude of the droplet acceleration tangent to the droplet trajectory. The corresponding wavenumber and wavelength are

$$K_{\mathrm{RT}} = \sqrt{\frac{a(\rho_l - \rho)}{3\sigma}}, \tag{40}$$

$$\Lambda_{\mathrm{RT}} = \frac{2\pi C_{\mathrm{RT}}}{K}, \tag{41}$$

respectively. Breakup is assumed to begin when the dominant wavelength, Λ_{RT} is less than the droplet diameter. After a period of,

$$\tau_{\mathrm{RT}} = \frac{C_\tau}{\Omega_{\mathrm{RT}}}, \tag{42}$$

the parent droplet completely breaks up into parcels of child droplets. The mean child droplet radius is determined using the correlation,

$$r_c = \frac{\pi C_{\mathrm{RT}}}{K_{\mathrm{RT}}}. \tag{43}$$

Both model constants are adjustable but are generally set to be, $C_\tau = 0.1$ and $C_{\mathrm{RT}} = 0.1$.

Kelvin-Helmholtz Rayleigh-Taylor (KH-RT): The hybrid Kelvin-Helmholtz Rayleigh-Taylor (KH-RT) model assumes that unstable growth of both KH and RT waves may occur simultaneously on the droplet surface. [65] In essence, both the KH and RT models described above are employed in tandem with the KH model predicting the continuous shedding of child droplets between the complete breakup events predicted by the RT model. Since we are focusing on pre-dispersed atmospheric droplets we neglect to include concepts such as initial breakup length and time which are only applicable to phenomena such as jets and sprays.

Droplet Vaporization

Droplet vaporization is modeled using the classical rapid mixing model [78], in which the liquid temperature, T_i, is assumed to be uniform throughout the droplet. Using this model, the droplet mass m_i and T_i are governed by

$$\frac{dT_i}{dt} = \frac{\mathrm{Nu}_i}{3\mathrm{Pr}} \frac{\theta}{\tau_i} (T - T_i) + \frac{L}{C_{p,l}} \frac{\dot{m}_i}{m_i}, \tag{44}$$

$$\dot{m}_i \equiv \frac{dm_i}{dt} = -\frac{\mathrm{Sh}_i}{3\mathrm{Sc}} \left(\frac{m_i}{\tau_i} \right) \ln(1 + B_{Mi}), \tag{45}$$

where $\theta = C_p/C_{p,l}$ is the ratio of specific heats of the background gas to the droplet liquid, $\tau_i = \rho_l d_i^2/(18\mu)$ is the Stokes time constant for the droplet, and L is the latent heat of evaporation. The droplet Nusselt Nu_i and Sherwood Sh_i numbers follow the Ranz and Marshall correlations for heat and mass transfer: $\mathrm{Nu}_i = 2 + 0.552\mathrm{Re}_i^{1/2}\mathrm{Pr}^{1/3}$ and $\mathrm{Sh}_i = 2 + 0.552\mathrm{Re}_i^{1/2}\mathrm{Sc}^{1/3}$ based on the droplet Reynolds number and the gas-phase Prandtl and Schmidt numbers. The Spalding mass transfer number $B_{Mi} = (Y_s - Y_v)/(1 - Y_s)$ relates the vapor mass fraction at the droplet surface Y_s to the vapor mass fraction in the background gas Y_v. We assume local thermodynamic equilibrium and compute Y_s based on the partial pressure of the liquid, such that

$$Y_s = \frac{P_{l,\mathrm{sat}}}{P} \frac{W_i}{\overline{W}} \tag{46}$$

where P is the local gas pressure, W_i is the molecular weight of the vaporizing species (in this case, water), $\overline{W}$ is the molecular weight of the gas mixture, and $P_{l,\mathrm{sat}}$ is the saturation pressure at the surface temperature. To control stability of the time integration, we impose a minimum mass on the droplets equivalent to a 1 micron diameter water droplet. Droplets that fall below this threshold are considered to be completely vaporized and their mass is transferred to the vapor phase over the course of a single time step.

When two-way coupling between the fluid (Equations (19) – (21)) and droplet equations is required, this is achieved using a simple cell-based averaging technique in which a filter is used to obtain smooth volume-averaged drag, thermal energy transfer, and vapor mass transfer data at each degree-of-freedom in the Eulerian finite-element mesh,

$$S_Q = \frac{1}{\delta t} \int_t^{t+\delta t} (-QK(\mathbf{x} - \mathbf{X}_i))\, dt \tag{47}$$

for $Q = \{\dot{m}, \mathbf{F}_d, dT_i/dt\}$ where K is a kernel function, taken to be unity in this work. We note that more complex smoothing functions can be used to improve the spatial distribution of the source, and future versions of this flow solver will incorporate these kernels.

4.1.3 Numerical Method

We use an Eulerian-Lagrangian approach to solve the two-phase flow problem in which the primary and dispersed phases dynamics are computed via a transient time-split phase coupling procedure in which the governing equations are solved by alternately advancing the primary and secondary phase equations over some finite time interval Δt.

The continuous gas-phase governing equations (Equations (19) – (21)) are discretized in space using a discontinuous Galerkin (DG) finite element method similar to that described by Hartmann [79]. In this formulation, an approximate Riemann solver (e.g., HLLC, Roe, Lax-Wendroff, etc.) is used to compute the numerical flux across adjacent element faces. The symmetric interior penalty method is used discretize the viscous fluxes, and time integration is done explicitly using a strong stability-preserving Runge-Kutta method. This formulation allows the use of high-order polynomial basis functions, which can increase the formal order of accuracy of the method above second order.

The dispersed phase ordinary differential equations are integrated utilizing using an explicit three-stage Runge-Kutta method. The size of the primary time step, Δt, is chosen to ensure numerical stability of the gas-phase governing equations with a CFL number equal to 0.05. For the smallest droplets in the system, the time step for the dispersed phase equations can be subcycled so as to provide enhanced numerical stability.

4.1.4 Physical Model

A typical hypersonic platform consists of a blunted nose cone or leading edge followed by a tapered forebody and an afterbody that houses the vehicle control surfaces. The flow environment in the vicinity of the leading edge can be quite severe and is likely to be reasonably approximated using the breakup time models discussed in Chapter 2. The interaction of droplets with the vehicle forebody and, potentially, with control surfaces downstream is less likely to be consistent with these correlations that were developed based on normal shock-droplet interactions. To illustrate this point, we investigate droplet-shock interaction around an idealized model of the a typical forebody: a 10° wedge. The conditions correspond to a wedge traveling at M=3 through quiescent air at 3 km altitude that encounters droplets in the range of 0.1-1mm in diameter. Figure 25 shows the temperature profile for the oblique shock over the wedge where the shock can be noted by the temperature jump running diagonally through the domain. After passing through this oblique shock, the droplets encounter a variable flow environment in which the choice of the drag models and the aerodynamic breakup models will have a significant impact on their likelihood of surface impact.

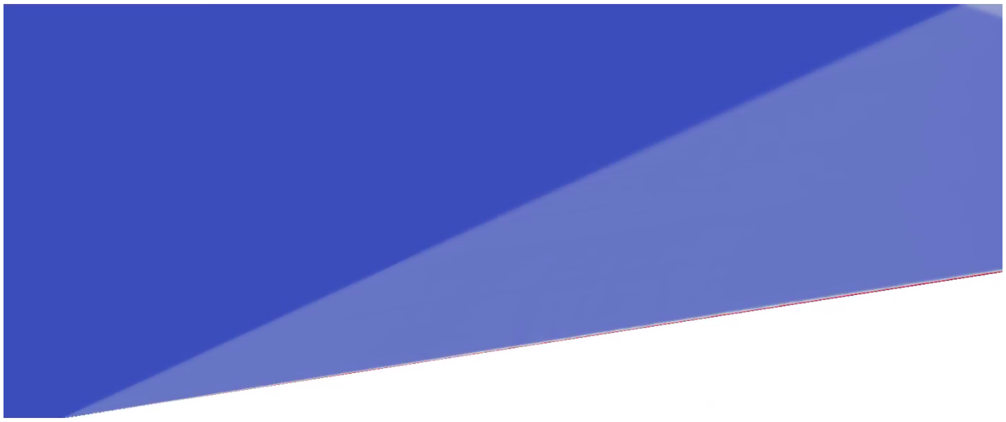

Fig. 25—Temperature profile for a 10° oblique wedge moving through quiescent air at 3 km altitude at M = 3. The temperature range is 268 K (blue) to 750 K (red, at the wedge surface).

4.2 Results

4.2.1 Drag Model Comparison

We begin with a comparison of a variety of droplet drag models with a droplet that does not undergo breakup. We selected four different drag models, three of which account for the effect of droplet deformation along with a rigid sphere model. In Figure 26, droplets 100μm in diameter are introduced upstream at a height of 0.1m. The necessity of including deformation effects is clearly apparent as the droplet using rigid sphere drag, denoted by the blue line, strikes and rebounds off the surface with little deviation from its initial trajectory. In contrast, all three models that account for deformation show the droplet trajectory turning significantly to match the flow in post shock region which runs parallel to the surface. Each of these models predicts a slightly different amount of deflection but in this case, all three predict that the droplet will not strike the wedge surface within our 1m test length. We note that we have not considered any impact damage models in this formulation, and any post-impact trajectories presented in this work are not physically meaningful.

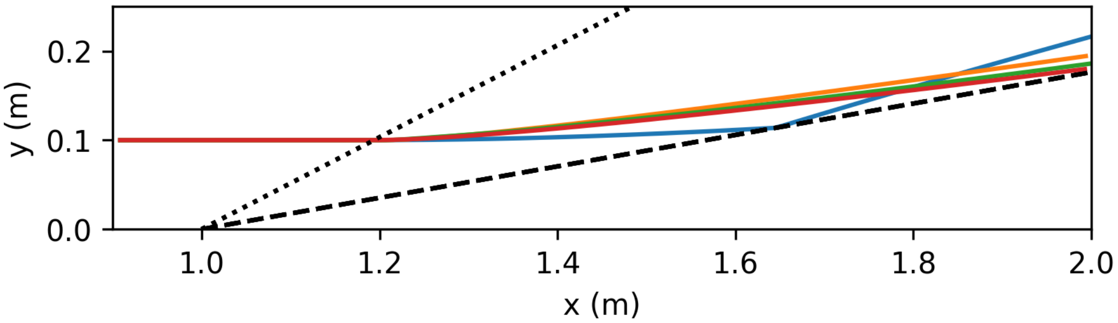

Fig. 26—Comparison of 100μm droplet trajectories in an oblique shock for varying drag models, no breakup: rigid sphere (blue), TAB (orange), NTAB (green), and Wiegand (red). The dashed line denotes the solid surface and the dotted line denotes the oblique shock.

In Figure 27, we plot the velocity magnitude of each droplet as it passes through the test region with the effect of each model becoming even more apparent. With the rigid sphere drag model, the droplet velocity changes relatively slowly before suddenly dropping just before $t = 0.8$ms. At this point, the droplet encounters the boundary layer and experiences a significant increase in drag forces as the relative velocity spikes. Conversely, the deformation-based models predict a sudden drop in particle velocity after encountering the shock. This is due to the large relative velocity and thus Weber number driving the particle to flatten into an oblate shape with a higher frontal surface area and drag coefficient, C_D. As such the droplets experience relatively high drag forces and their trajectories more quickly adjust to match the post shock flow. The end result is that they turn soon enough to avoid impacting the wedge surface. As the relative velocity decreases, the droplets return to a more spherical shape with a lower drag coefficient similar to that used in the rigid sphere drag model.

The increased drag, even if only significant shortly after the shock, is sufficient to prevent the impact predicted for the rigid sphere as evidenced in Figure 28. Here we plot the trajectory of droplets with a range of starting heights from $y = 0$ to 0.15m for each of the drag models. Using the rigid sphere drag model,

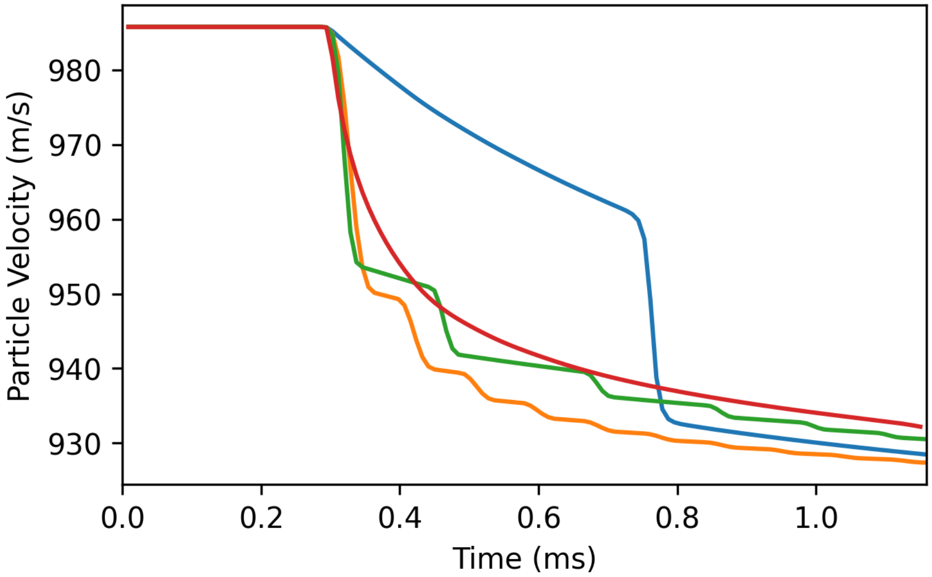

Fig. 27—Comparison of 100μm droplet velocities in an oblique shock for varying drag models, no breakup: rigid sphere (blue), TAB (orange), NTAB (green), and Wiegand (red).

all of the droplets strike the surface and, due to the weak deflection by the flow field, they do so at with a relatively small angle of incidence. The deformation based models lead to most of the droplets in the upper half of the range missing the surface entirely. The droplets that do impact the surface do so with a larger angle of incidence than the rigid drag droplets. This will directly affect the amount of surface erosion caused by a droplet, which will be proportional to the impact velocity normal to the surface.

4.2.2 Breakup Model Comparison

We next compare the effect of the choice of breakup model on the droplet behavior. For this series of simulations, we use a common drag model: the correlation-based Wiegand model. Droplet trajectories and diameters are shown in Figure 29 and Figure 30, respectively. All cases show the behavior of a 1mm droplet introduced into the domain at a height of $y = 0.1m$. This larger initial droplet diameter is characteristic of a rain droplet and, importantly, it allows more significant breakup events to occur and thus better illustrates the differences between the various models.

The TAB and NTAB models produce similar results, varying only in breakup timing and the size of the child droplets produced. By design, both models predict complete breakup of the parent droplet which can be noted by the small gap in the trajectory plots and the discrete cutoff of the parent droplet line in the diameter plots. On breakup the mass of the parent droplet is equally divided among two or more parcels of child droplets that are placed at a randomized position near the breakup point. The TAB model predicts later breakup and larger child droplet sizes but are overall very similar and prove difficult to compare in the absence of experimental data.

The KH model produces qualitatively different breakup behavior. In this model, the parent droplet does not completely breakup but instead continuously sheds child droplets as they are stripped from the surface while the droplet Weber number remains above some critical value. This tends to result in the production of a large number of relatively small child droplets and a more continuous loss of mass by the initial parent droplet.

The RT model, on the other hand, predicts sudden, complete breakup of the parent droplet similar to the behavior of the TAB and NTAB models. However, this breakup process is instead driven by the magnitude of acceleration tangent to the droplet's trajectory. Breakup under the TAB and NTAB models depends only on the relative velocity of the droplet. For this oblique shock interaction, the acceleration peaks as the droplet first encounters the shock and RT breakup is predicted to occur shortly thereafter. Compared to the TAB and NTAB models, RT breakup takes place much sooner and we believe that for our purposes it is akin to a catastrophic breakup mechanism.

Finally, the KHRT model uses the KH model in conjunction with the RT model in an attempt to capture both the shear stripping and catastrophic phenomena expected in high We regimes. From the diameter plot we see that after encountering the shock the initial parent droplet undergoes a few rounds of KH breakup before suffering complete RT breakup. Then the child droplets undergo more KH breakup until they drop below the critical We threshold. This end result captures both expected types of phenomena that we expect to see in a controllable fashion making this a strong candidate model for continued investigations.

4.2.3 KHRT

Here, we provide further investigation of the KHRT breakup model by considering its behavior with respect to varying drag models and a selection of model parameters.

Most notably, we see a pronounced effect on the RT breakup time using the various drag models, which predict markedly different post-shock acceleration of the droplet. From top to bottom in Figure 31 and Figure 32, the peak acceleration predicted after the shock increases leading to shorter RT breakup times and smaller RT child droplets. Since KH breakup is allowed to occur during the RT breakup process, more KH child parcels are produced in the cases with slower RT breakup. This leads to wide array of possible droplet size distributions and trajectories just by changing the drag model. So here it is apparent that the drag model is not only important in determining the droplet trajectory but also significantly influences the breakup behavior.

Finally, we demonstrate the combined effect of droplet deformation and breakup of an array of smaller 100 μm droplets in Figure 33. With the KHRT breakup model active, none of the droplets strike the wedge's surface. The child droplets produced by breakup are able to more quickly turn to match the flow conditions due to their smaller size and lower Stokes number.

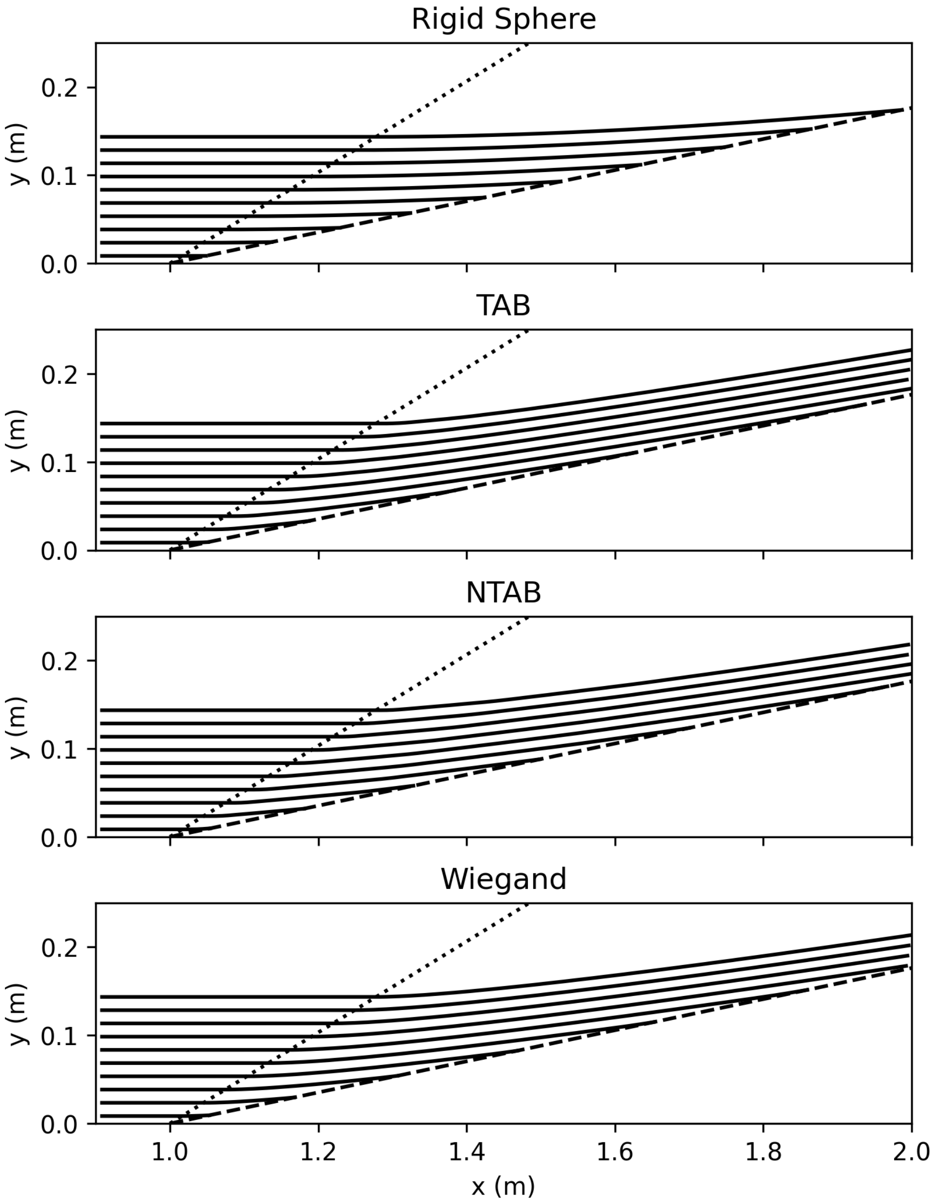

Fig. 28—Comparison of 100μm droplet trajectories for a selection of starting heights ranging from $y = 0$ to 0.15m in an oblique shock for varying drag models, no breakup. The dashed line denotes the solid surface and the dotted line denotes the oblique shock.

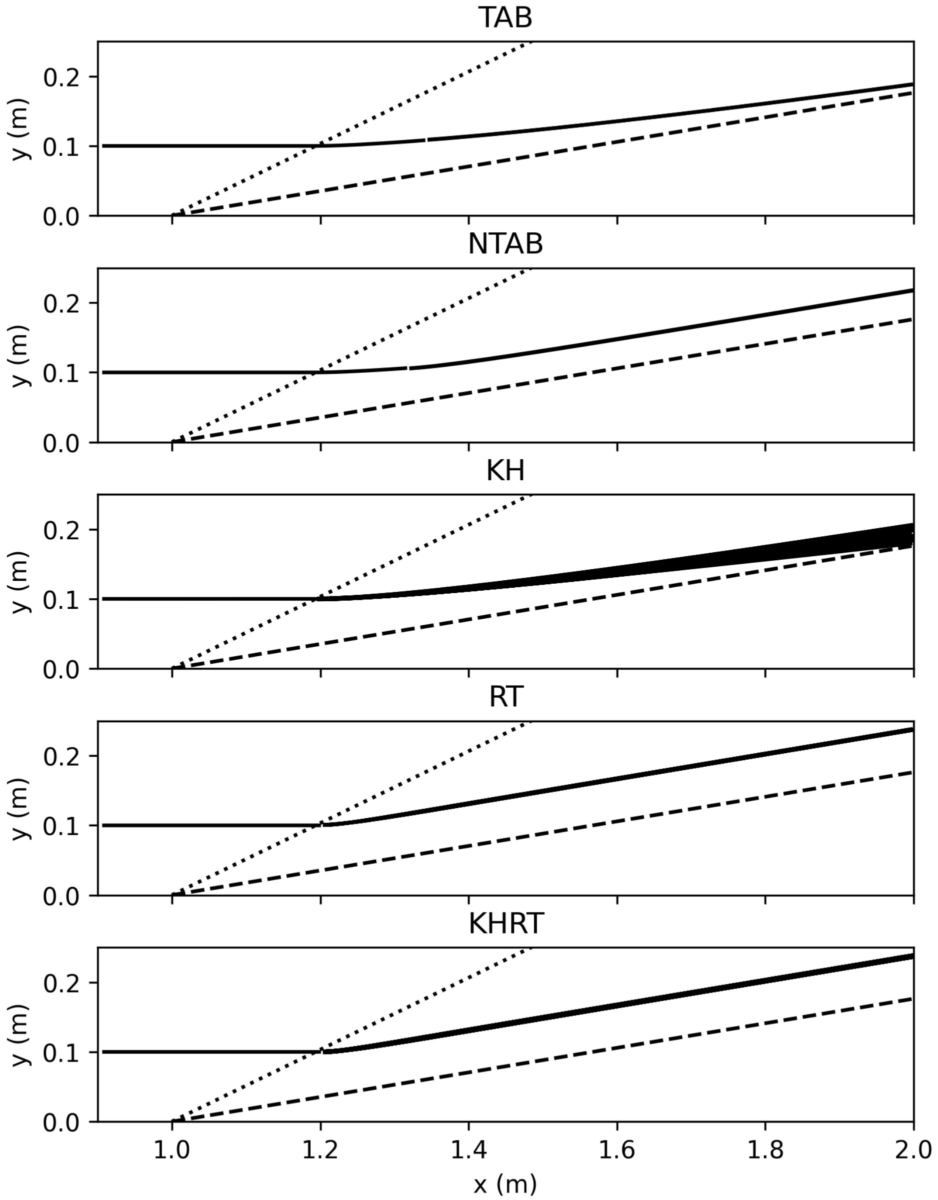

Fig. 29—Comparison of 1mm droplet trajectories for various breakup models in an oblique shock with the Wiegand drag model. The dashed line denotes the solid surface and the dotted line denotes the oblique shock.

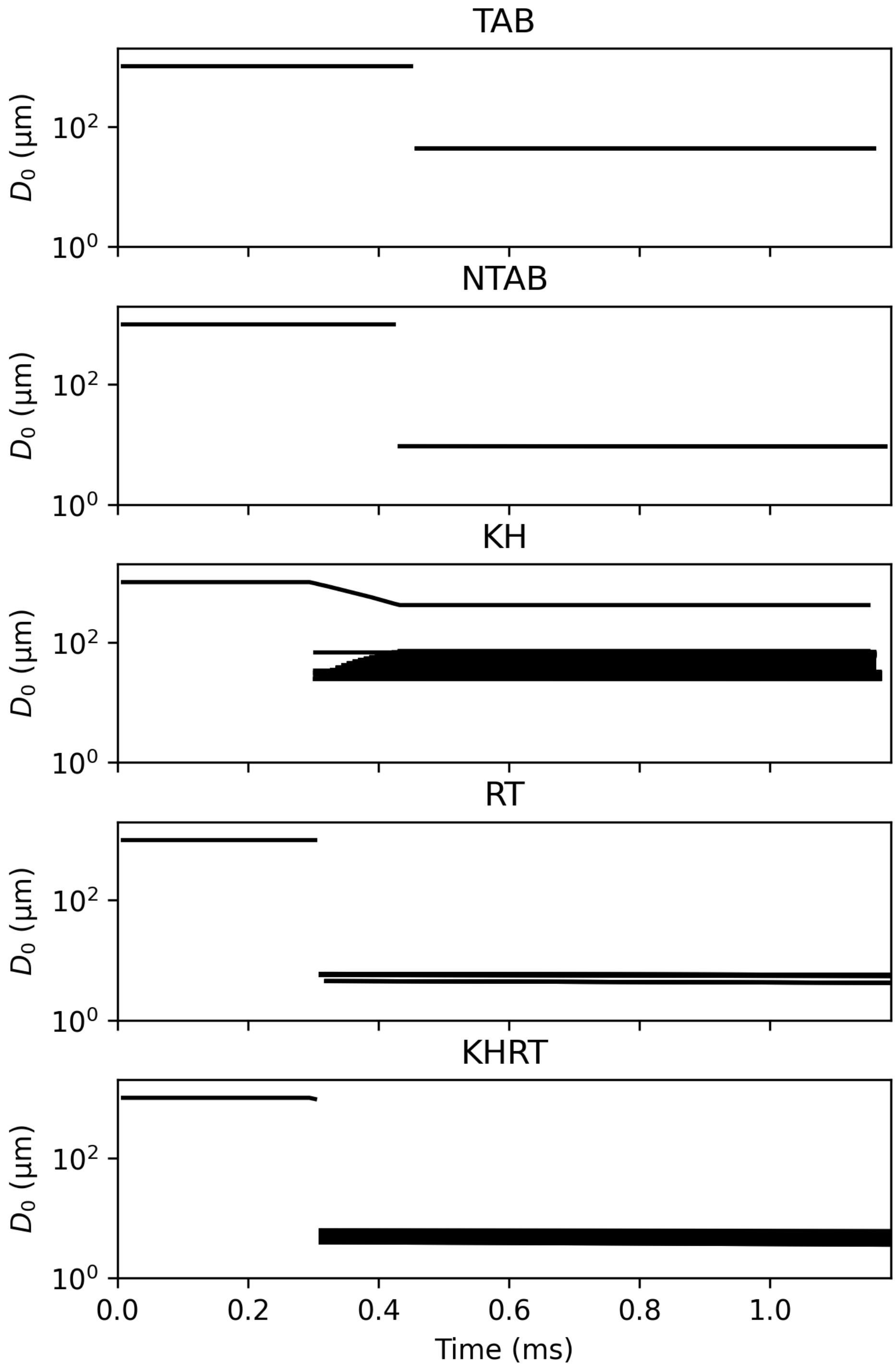

Fig. 30—Comparison of 1mm droplet diameters for various breakup models in an oblique shock with the Wiegand drag model.

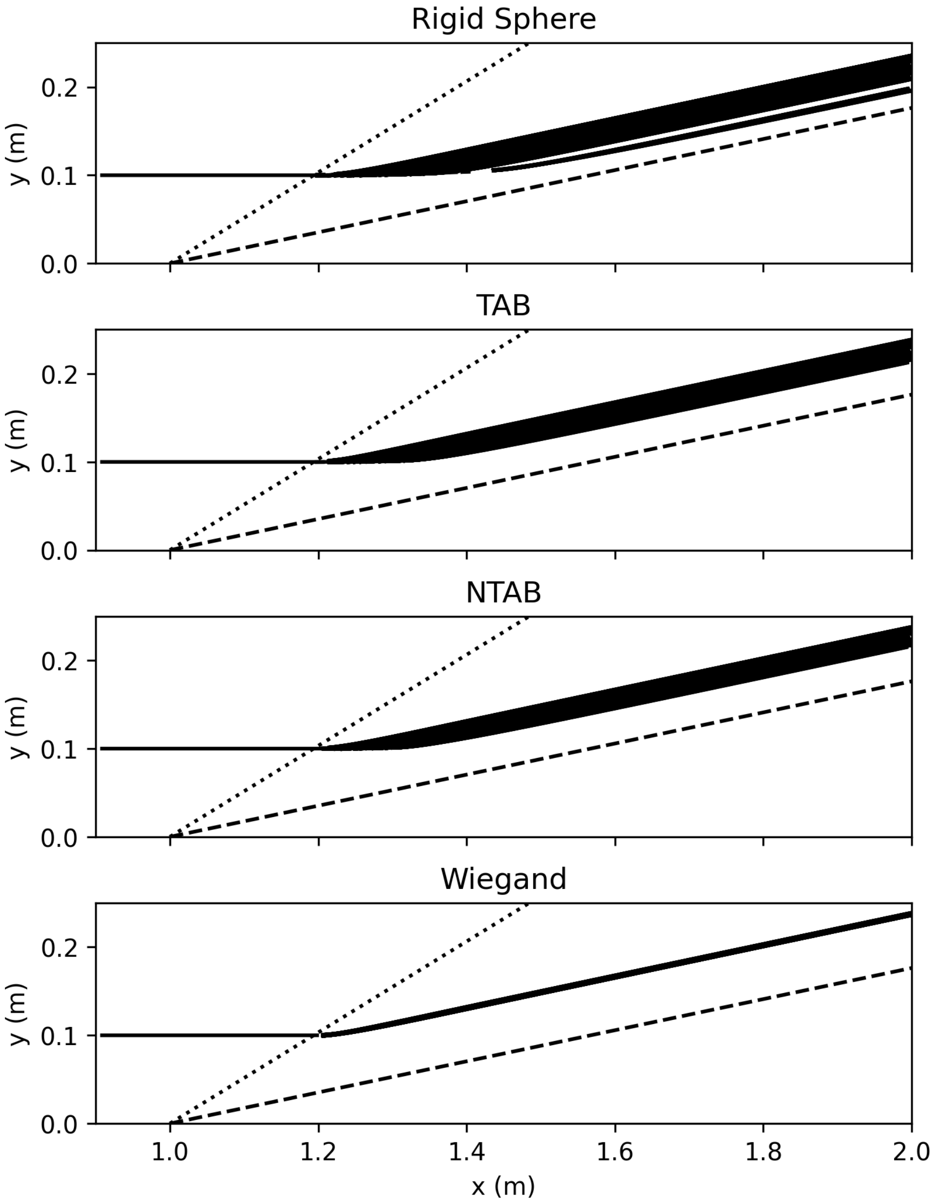

Fig. 31—Comparison of 1mm droplet trajectories for KHRT breakup with various drag models in an oblique shock. The dashed line denotes the solid surface and the dotted line denotes the oblique shock.

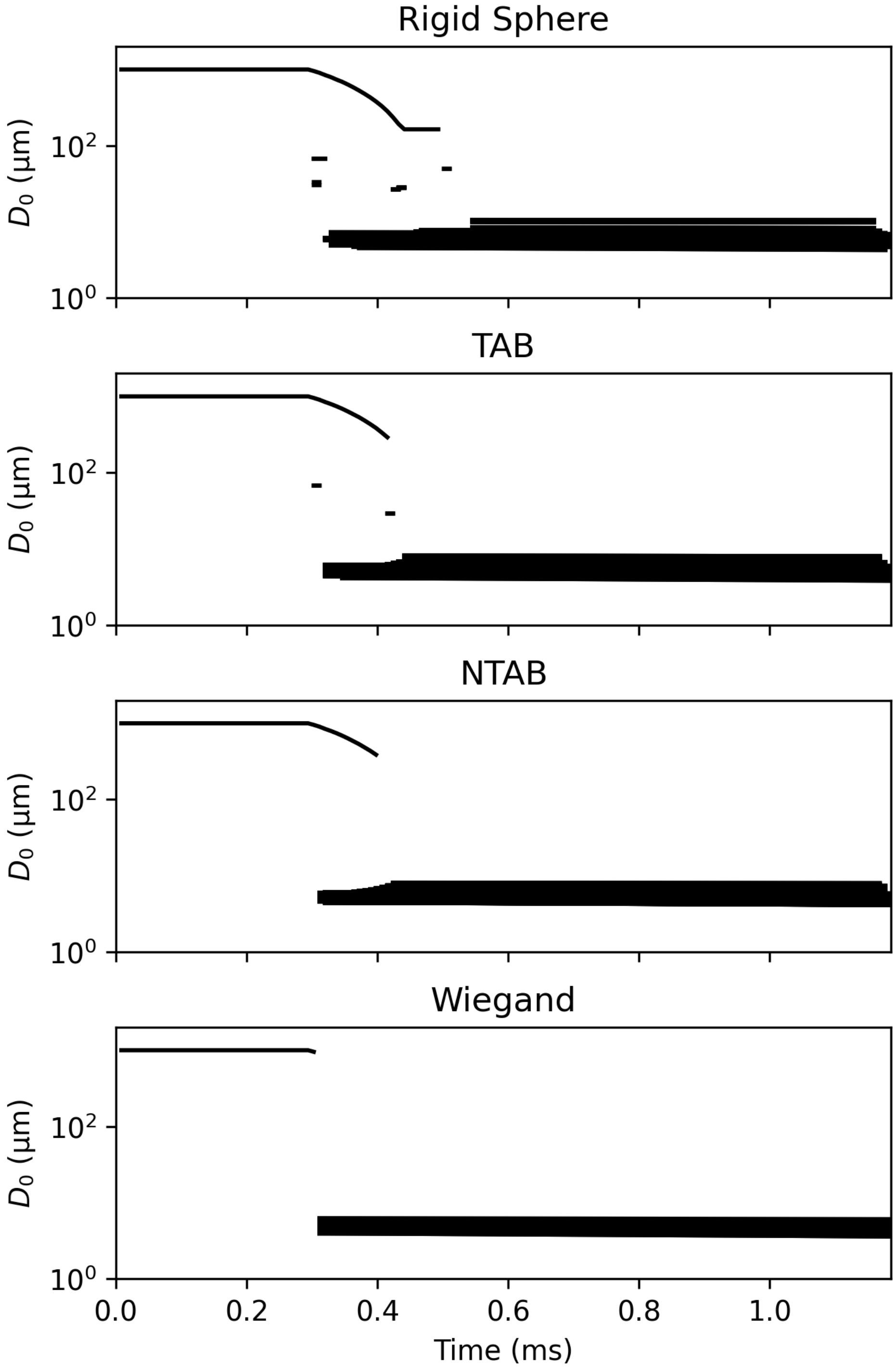

Fig. 32—Comparison of 1mm droplet diameters for KHRT breakup with various drag models in an oblique shock.

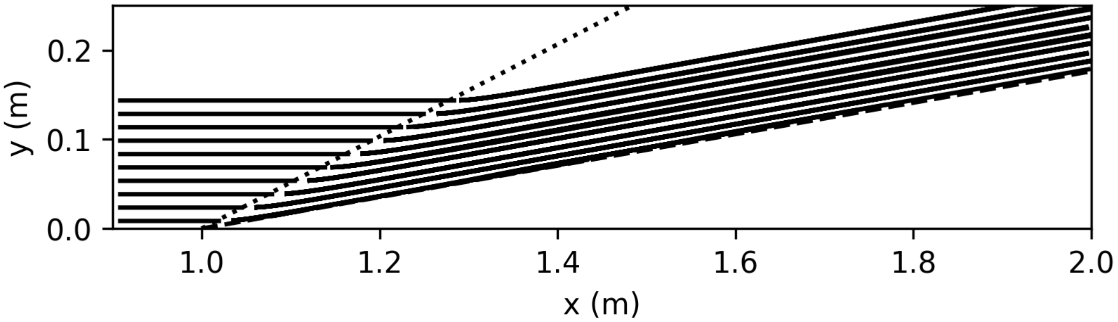

Fig. 33—KHRT 100μm droplet trajectories for a selection of starting heights in an oblique shock with the Wiegand drag model. The dashed line denotes the solid surface and the dotted line denotes the oblique shock.

4.3 Implications

The erosion potential of liquid droplets can vary markedly depending on which underlying drag and breakup models are used, from predicting 100% impact (Figure 28) to 0% impact (Figure 33). The fundamental question that remains is which of these models are most appropriate for this particular flow regime. Experimental data and direct numerical simulations of droplet behavior in this regime are sparse throughout the scientific literature. Thus, a clear need exists to develop a comprehensive catalog of droplet acceleration and demise data in vehicle-relevant flow fields. The remainder of this report (Chapters 5-8) summarizes NRL's contributions to such an effort.

5. DROPLET INTERACTION WITH A BLAST WAVE

As a first attempt to characterize the interaction of a droplet with a curved shock wave, a short set of experiments were conducted using a linear model detonation engine (LMDE) at the University of Maryland's Propulsion Research Laboratory. The purpose of these tests was to gather high-quality images of the initial stages of droplet breakup that could be used to validate CFD model predictions of droplet deformation. This chapter describes the experimental approach used for the experiments and summarizes the key results obtained.

5.1 Facility Description

The LMDE test facility is a laboratory scale Rotating Detonation Engine (RDE) unwrapped into a linear channel that allows optical access for the study of the structure and propagation of detonation waves. The LMDE consists of a Pulse Detonation Engine (PDE) which generates a hydrogen/oxygen detonation that propagates into a narrow channel with side windows (test section). The channel has a row of injection ports that spans the bottom wall length but has no top boundary (open to ambient) to allow free expansion of waves and avoid undesired reflections. Figure 34 shows photographs of the LMDE setup with detailed views of the PDE, the optical access, and the narrow test section channel.

Under normal operation of the LMDE facility, the detonation generated by the PDE enters into the test section and is sustained through combustion of gaseous fuel injected through the bottom wall ports. For the experiments performed under this research program, the regular operation of the LMDE facility was significantly modified in order to generate a completely different flowfield where the interaction of a moving shock wave and a stationary droplet could be studied.

To that end, the operating condition of the PDE was changed to generate a *blast wave* instead of a *detonation wave* propagating into quiescent air in the test section.[15]In that flowfield, the moving blast wave simulates the leading edge shock of a supersonic vehicle. A flat-tip straight needle connected to a syringe shown in Figure 35 was also integrated to the top of the test section to insert a water droplet into the path of the propagating blast wave. Finally, no fuel injection through the bottom wall of the channel was performed as any fluid injection would disturb blast wave propagation.

---

[15] A detonation wave is a high speed propagating shock with an attached reaction zone. In contrast, a blast wave is a much lower propagating shock with a detached reaction zone behind it.

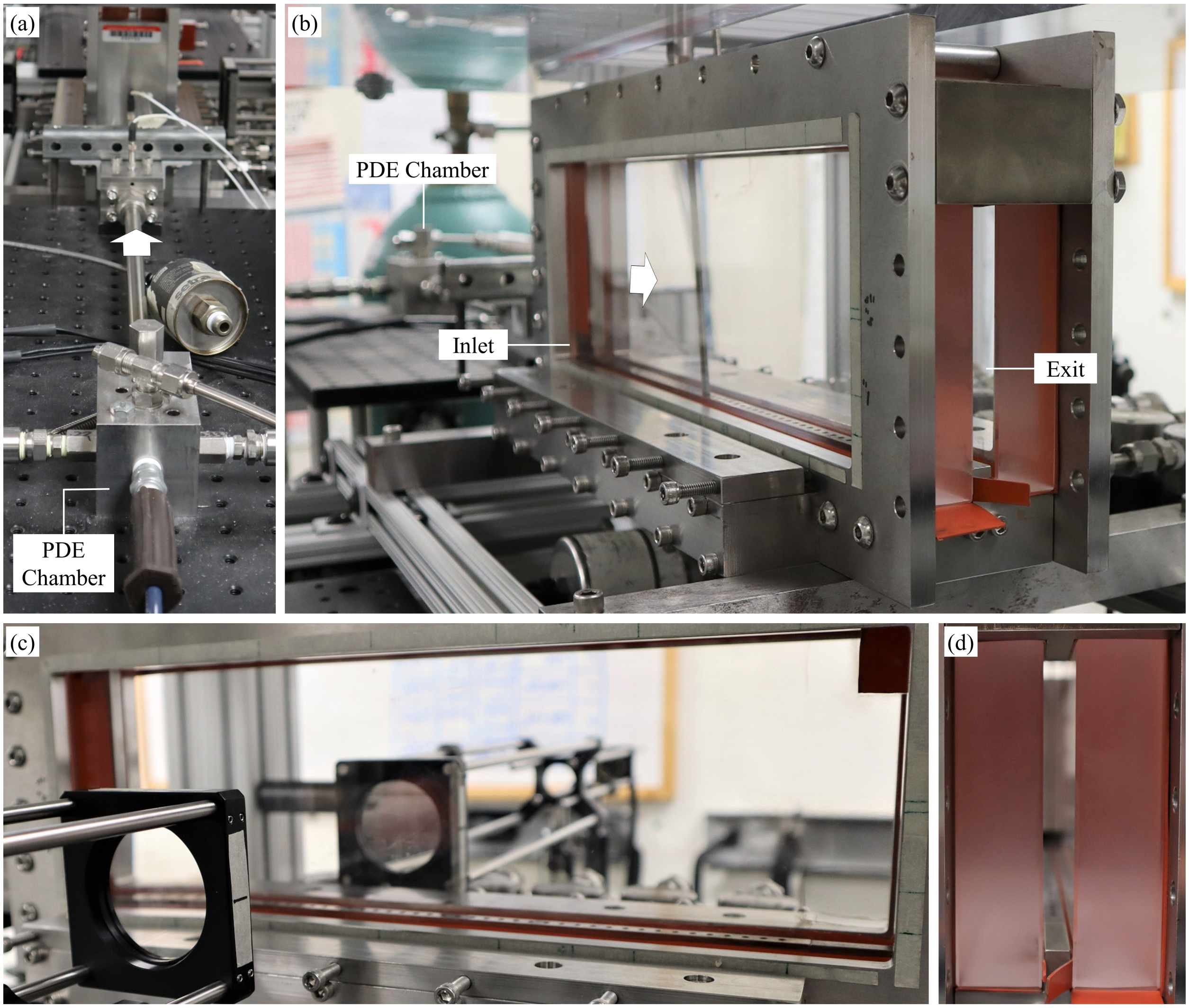

Fig. 34—LMDE facility and optical diagnostics setup: (a) PDE ignition chamber and tube with detonation propagation direction arrow, (b) Isometric view of test section, (c) 2-in lens optical setup to capture shadowgraph visualizations, (d) View of test section rectangular channel from exit side.

Fig. 35—Stainless steel, flat-tip, 30-gauge needle with syringe used to generate droplets for the experiments.

5.2 Optical Diagnostics

The primary flow diagnostic used for the experiments was high-speed shadowgraphy. An optical setup using 6-in mirrors was used to capture large field of view shadowgraphs of the blast wave flowfield. Additionally, a 2-in lens setup was used to obtain complementary high resolution zoomed-in views of the droplet/blast wave interaction (see Figure 34c). A Phantom v2512 camera captured images at a rate of 250,000 frames per second with a resolution of 384 by 160 pixels. The timing and synchronization of the experiment was performed using an NI/LabView based control system.

Figure 36 shows a cross-sectional view of the LMDE facility and highlights the approximate location of the 6-in shadowgraph field of view with respect to the overall length of the LMDE test section. A representative photograph of the blast wave flowfield generated by the PDE and propagating through the narrow test section channel from left to right is also shown. From this image, note how the curved shock wave travels upstream of the reaction front and combustion products exiting the PDE. In this flowfield, the test window to study droplet breakup is constrained to the short period of time between a droplet encountering the shock and the time the reaction front and combustion products reach it.

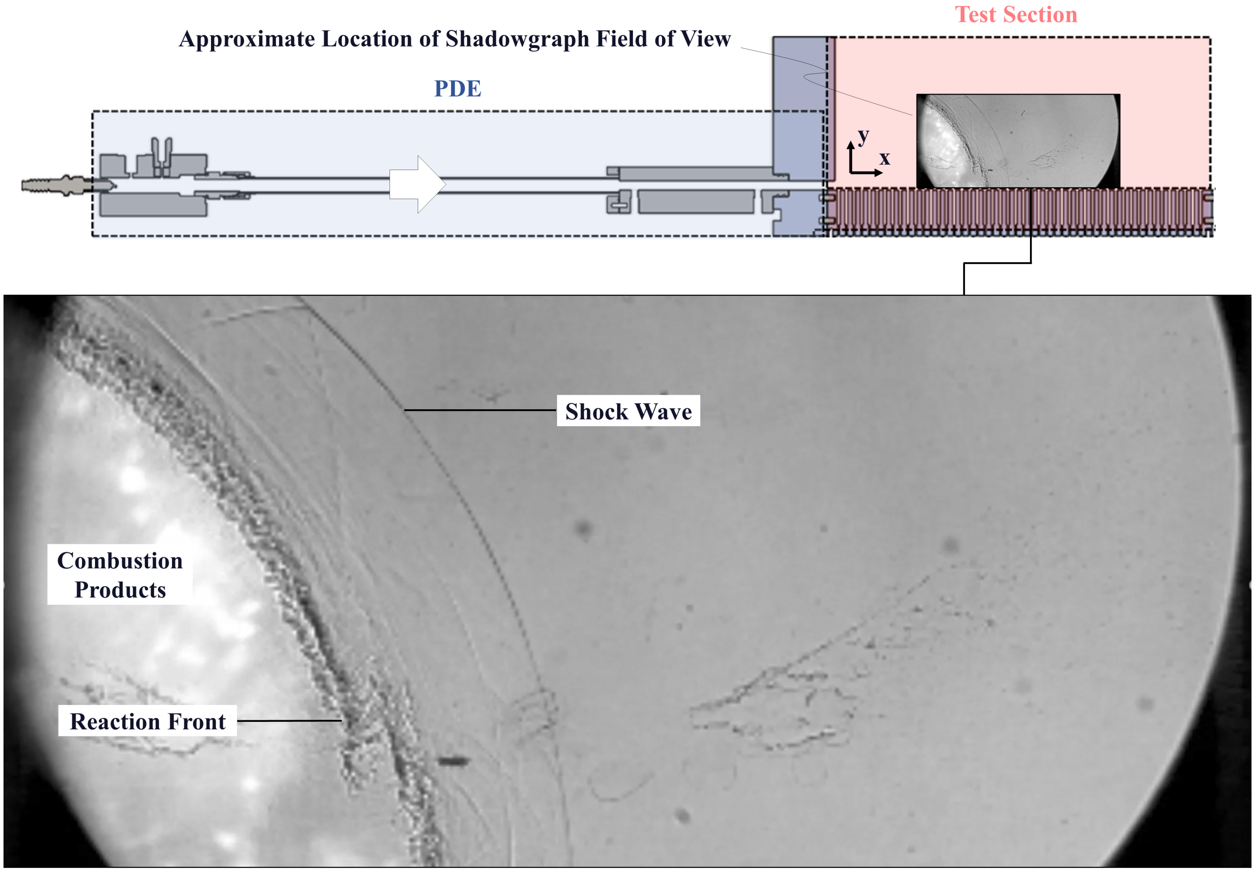

Fig. 36—Cross-sectional view of LMDE flowpath with sample shadowgraph image in test section highlighting approximate location of camera field of view *(top)*. Full-scale sample shadowgraph image of blast wave flowfield *(bottom)*. Note curved shock detached from reaction zone (blast wave flowfield signature). No needle inserted. LDME schematic modified from [80].

5.3 Test Conditions

Water droplets were generated at the tip of the needle by filling up the syringe and gently tapping the plunger before each test.[16] Unfortunately, no control over the size of the droplets was possible by using this method. Droplets hanging from the needle tip had either a "one-sided" or "symmetric" shape depending on whether the liquid attached itself to one side of the needle exclusively or surrounded its tip (see Figure 37). Similar to droplet size, there was no way of consistently producing a specific droplet shape before each test.

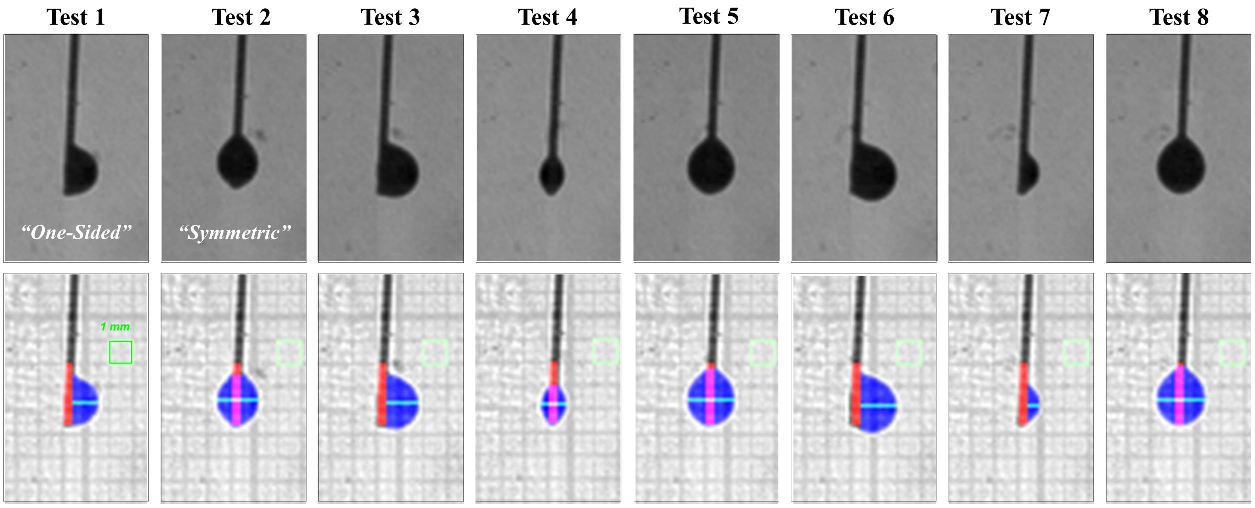

	Test 1	Test 2	Test 3	Test 4	Test 5	Test 6	Test 7	Test 8
W (mm)	1.13	1.75	1.38	1.25	2.00	1.63	0.50	2.25
D_{eq} (mm)	-	1.99	-	1.45	2.24	-	-	2.32

Fig. 37—Shadowgraph images of droplets suspended from needle tip for tests performed *(top)*. Processed and calibrated images used to estimate droplet size *(bottom)*. Segmented needle tip is colored red, droplet colored blue, measured droplet width shown by cyan line, and 1-mm sizing square shown in green.

A total number of eight tests were performed for this study. Figure 37 shows raw images of the droplets captured before each test together with a set of corresponding processed images that were calibrated using a background grid to estimate droplet size. For the "one-sided" droplets, the measured width was the metric used to characterize droplet size. For the "symmetric" droplets, an equivalent diameter was determined using the measured droplet area from the images. As shown in Figure 37, droplet width for the eight droplets tested ranged from 0.5 to 2.25 *mm* while equivalent diameter ranged from 1.45 to 2.32 *mm*.

To limit the parameter space to be tested and focus mainly on droplet size, a single blast wave condition and droplet location were used throughout the experimental campaign. The vertical (y-coordinate) and axial (x-coordinate) position of the needle selected was based on guidance from the Propulsion Research Laboratory graduate student who operates the facility on a regular basis (roughly between 0.6 and 1" away from the channel floor).

The blast wave Mach number for each test was determined by calculating the radial velocity of the shock at the droplet height and using the laboratory ambient speed of sound. This was done by first superimposing 3-4 images of the blast wave prior to the encounter with the droplet and using this overlay to calculate the axial shock displacement. Then, the shock angle at the droplet height was measured using the last image

---

[16] For physical constraints associated with the setup itself, this was the only method of generating a droplet.

recorded of the blast wave before the interaction. With this angle, which was consistently between 70-73 °, the component of the displacement perpendicular to shock front was determined. Finally, with the known time interval of 4 μm between frames, the radial velocity was obtained. Figure 38 graphically shows the details of these calculations. For the eight tests conducted, the average blast wave velocity and average blast wave Mach number were 841 m/s and 2.44, respectively.

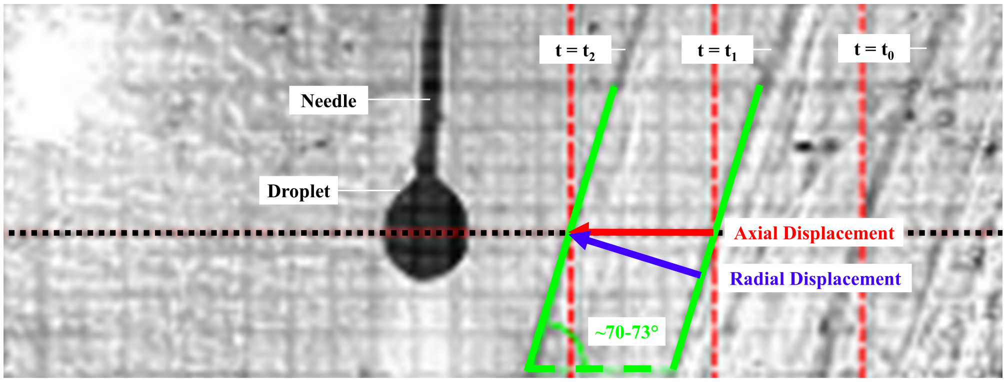

Fig. 38—Overlay of three consecutive shadowgraphs used to calculate blast wave velocity based on shock wave displacement and angle measurements. Red vertical lines highlight shock position at $t = t_0$, t_1, and t_2 using droplet center line as a reference. Green lines superimposed on shock at $t = t_1$ and t_2 were used to measure shock angle for radial displacement calculation.

5.4 Results and Discussion

Figure 39 shows sample time sequences of droplet interaction with a blast wave for two droplet sizes with a “symmetric” shape. Upon encounter with the blast wave, the appearance of a shock in front of the droplet is an unequivocal indicator of a supersonic flow interaction. Once fully inside the shocked flow, there is a noticeable shape change that occurs, with both droplets beginning to flatten and develop a “cupcake-like” appearance (t = 4 μs for Test 4 and t = 8 μs for Test 5). Following this initial shape change, gradual droplet flattening continues to occur but apparent mass stripping becomes the outstanding droplet break-up feature. The images captured for these two tests show how the needle changed the shape of the droplet-induced shock, but there is no clear indication that it affected the breakup behavior.

Given the extremely short test time available in these experiments ($\approx 16\mu s$), the results shown in Figure 39 only provide a glimpse into the initial stages of droplet breakup when exposed to a supersonic flow behind a moving shock. Despite this, it is important to note that the mass stripping observed in the images closely resembles the behavior reported by Joseph [38] for a 2.5 *mm* droplet exposed to the flow behind a Mach 3 normal shock as shown in Figure 40. Qualitatively, in both break-up sequences, the flat windward surface of the droplet appears to be parallel to the shock wave front that just traversed it. Similarly, the contrail that appears due to water stripping is perpendicular to the shock front. Finally, given the relatively steep blast wave shock angle (70-73°) and limited time for droplet breakup to advance, the results shown in Figure 39 can be representative of the short-lived interaction between a raindrop an the leading edge shock of a blunt supersonic body prior to surface impact.

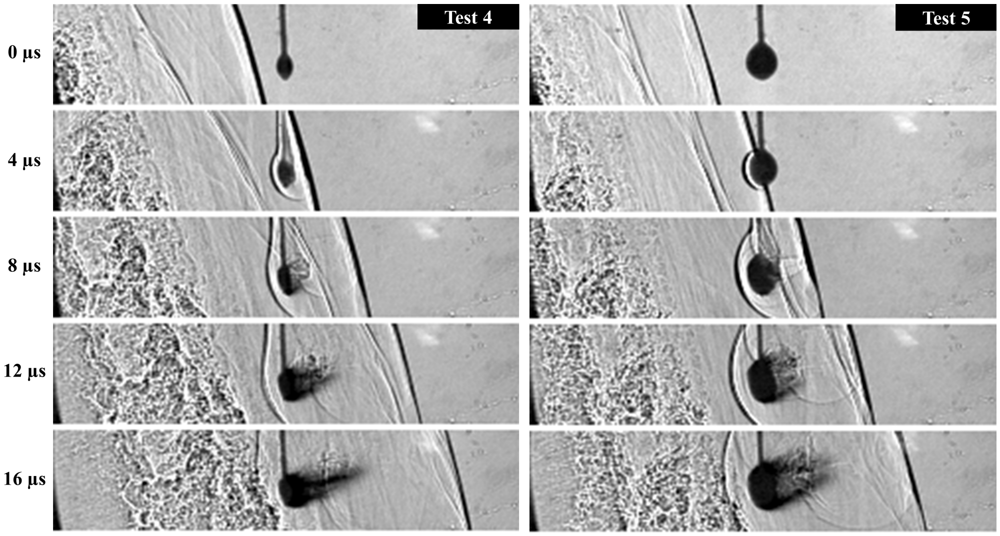

Fig. 39—Sample sequences of water droplet interaction with a Mach 2.44 blast wave. Equivalent droplet diameters determined from images captured before the encounter were 1.45 *mm* for Test 4 and 2.24 *mm* to Test 5. Test window for droplet breakup ends upon interaction of reaction front from PDE exhaust with droplet-induced shock.

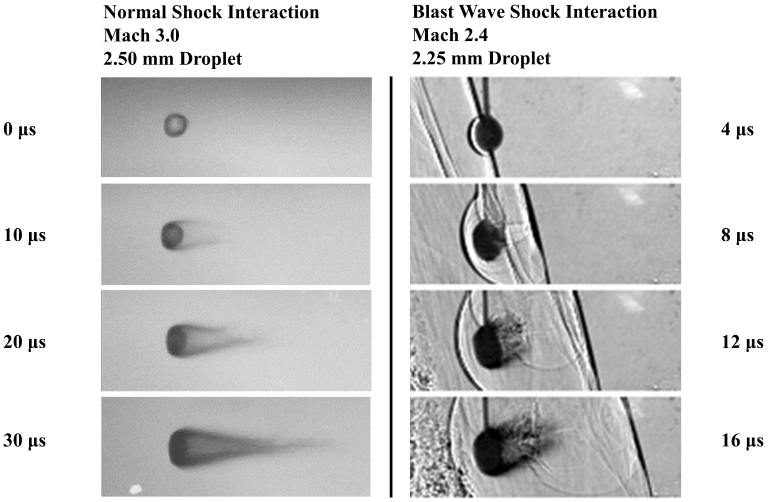

Fig. 40—Onset of droplet breakup due to interaction with flow behind a normal shock by Joseph [38] compared against breakup behavior observed due to interaction with flow behind a blast wave in this study.

6. DROPLET INTERACTION WITH SUPERSONIC PROJECTILES

A final set of tests were performed in a ballistic range at the Southwest Research Institute (SwRI) in San Antonio, TX. The goal of these experiments was to collect droplet demise data to expand and improve the results obtained at the University of Maryland with the LMDE. We note that the data presented in this chapter only represent a subset of the full results obtained. A future journal publication planned for the program will include the material and results not presented here after final analysis and processing are completed.

6.1 Motivation

A large body of research on droplet encounters with hypersonic vehicles has looked at nosetip or leading edge collisions [41] [42]. That is not surprising given how any shape change or material loss occurring at those surfaces will have a significant detrimental effect on vehicle aerodynamics in terms of drag and may induce undesirable localized heating through the increase of surface roughness or hot spot generation.

At those stagnation regions, despite the large gradients favorable to droplet break-up, the shock standoff distance is so small that droplet transit times are extremely short for any significant mass stripping and breakup to occur before impact. [40] Therefore, for a droplet size above a critical value, it is safe to assume that the interaction with the normal shock does not change the droplet impact conditions and a prediction of surface damage may be done by using the kinetic energy of the collision.

That is not the case however for droplet encounters with other vehicle regions. Droplets reaching the planform or a downstream control surface will have crossed a post-shock region with significantly lower gradients in comparison to the gas behind a planar shock at a stagnation point. Lower gradients weaken breakup mechanisms such as mass stripping and deformation which is undesirable, but droplets will have much longer transit times through those post-shock regions which allow the droplet breakup process to advance.

Understanding droplet behavior across that shock layer and ultimately the conditions of the droplet prior to impact on a surface downstream of the leading edge is critical for any type of surface erosion modeling that is performed. This is particularly important if one considers how for a hypersonic vehicle flying through a cloud or rain field, the vast majority of droplet encounters will occur along its planform and rear control surfaces, and any increase in frictional drag or loss of control authority induced by droplet encounters can also put the success of a mission at risk. For these reasons, the experimental study described in this chapter focused mainly on the interaction of droplets with the conical shock away from the stagnation region.

6.2 Experimental Setup and Diagnostics

The tests were performed in an indoor ballistics facility at SwRI using a 20-mm caliber gun which launched projectiles at different speeds through a column of falling droplets. A total number of 53 shots were fired using two projectile designs, a blunted cylinder and a 10° cone. Each projectile consisted of a polycarbonate body for barrel wall engagement attached to a leading edge nose tip. Different tip materials including brass, tungsten, and a combination of aluminum and tungsten were used for the tips to change the overall projectile mass and in doing so achieve different flight speeds. The purpose of using two projectile designs and launching them at multiple speeds was creating a wide range of bow shock geometries with different post-shock conditions to study droplet interaction. Figure 41 shows a picture of the four projectiles used in the experiments highlighting their metallic tips.

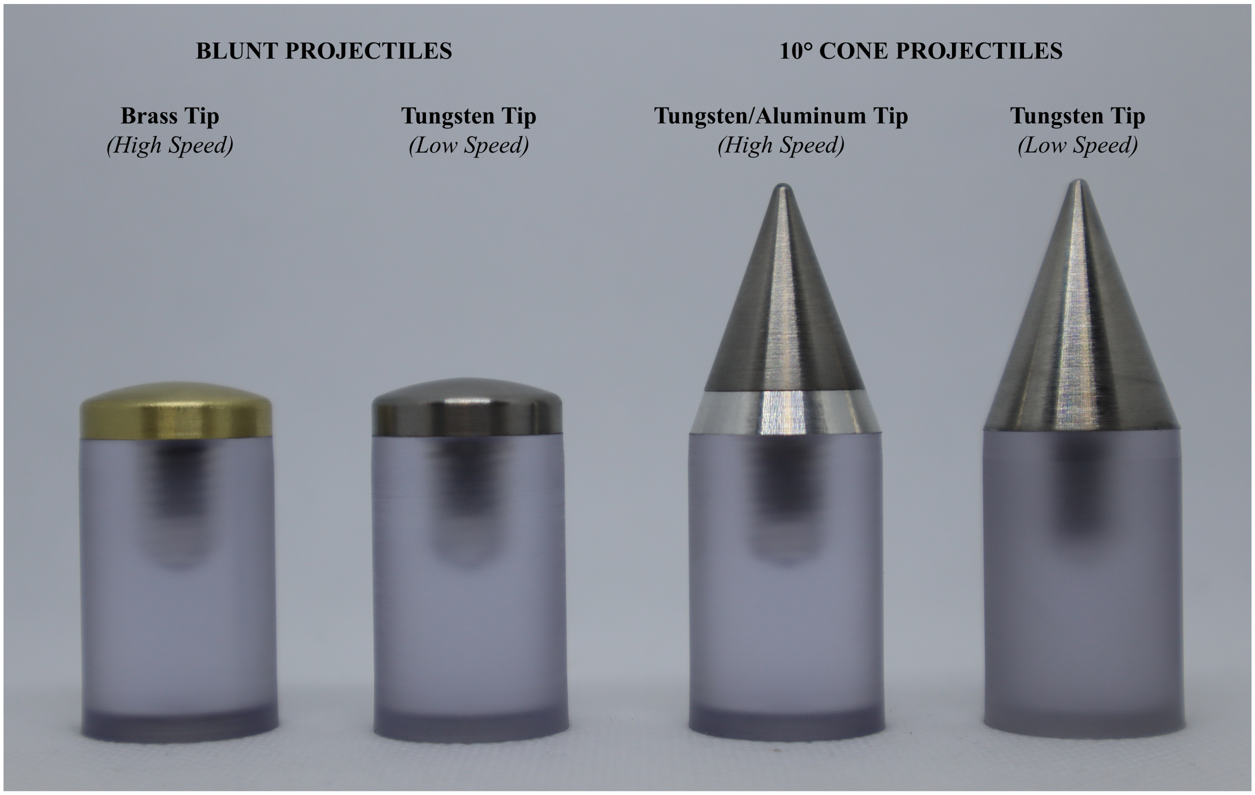

Fig. 41—Blunted cylinder and 10° cone projectiles used in the experiments.

Falling water droplets for the experiments were generated using a dripper system which consisted of a Microfab pneumatic pressure controller connected remotely to a Nordson EFD syringe barrel with a stainless steel dispensing needle. The pneumatic controller was used to adjust the back pressure of the syringe before each test and push a water jet out of the needle which would break into multiple droplets through the Plateau-Rayleigh instability. Three nominal droplet sizes referred to as small, medium, and large were generated in the experiments by changing the needle size. Actual droplet sizes were determined post-test and were found to be as small as 198 μm and as large as 1835 μm.

Droplet-shock interactions were experimentally characterized using synchronized ultra-high speed shadowgraphy and high-speed photography. Figure 42 shows a schematic of the optical diagnostics arrangement used, which included a total of four cameras to visualize the droplet break-up process from multiple angles. A Kirana 5M camera was used to capture high spatial and ultra-high temporal resolution shadowgraphs of the droplets interacting with the shocked flowfield (924 x 768 pixels at 1 MHz frame rate). Two Phantom V2012 cameras were used to record stereo views of the droplets from an uprange and downrange position (256 x 224 pixels, 200 kHz frame rate). A Phantom V711 was used with a mirror in a plane below the shot line to capture bottom views that allowed tracking the radial impact location for each test (256 x 224 pixels, 100 kHz frame rate). Finally, a second Phantom V711 was used closer to the exit of the gun barrel with a calibration target in the background to photograph the projectile in flight from the side view and determine its flight speed for each test (352 x 128 pixels, 110 kHz framing rate).

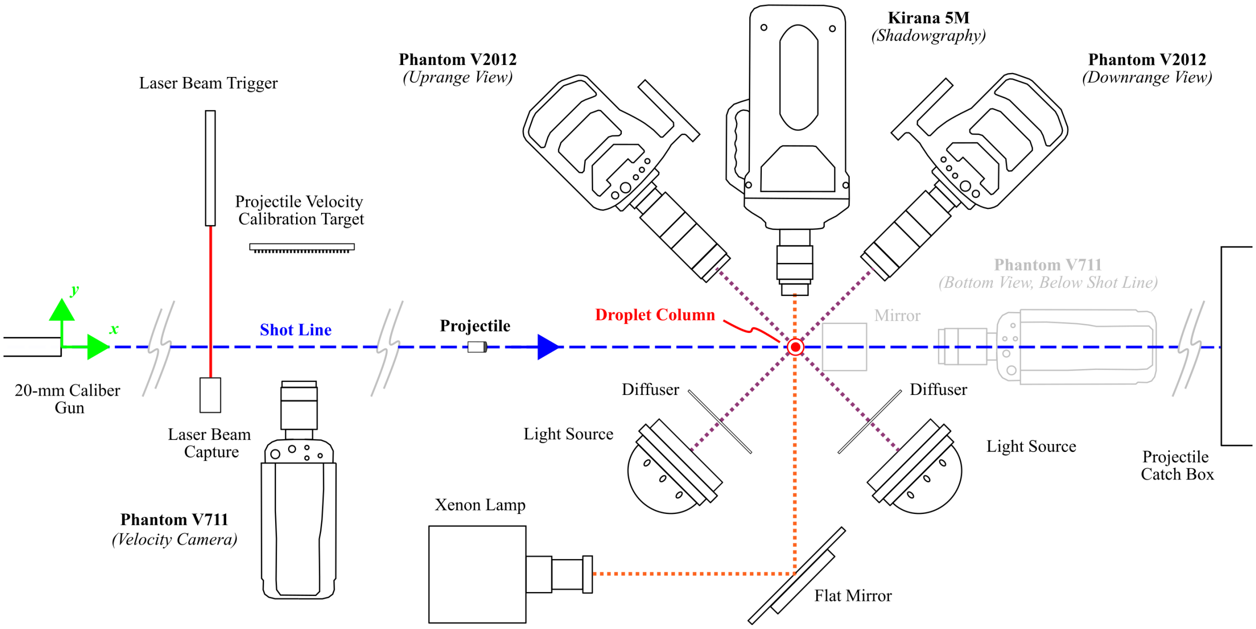

Fig. 42—Optical diagnostics arrangement highlighting shot line in blue with projectile flying from left to right. Every component shown is at the same y-x plane except for one of the Phantom V711s which was placed on a parallel plane below to capture bottom views of the projectile colliding with the droplet column.

6.3 Test Procedure and Conditions

The first step in the experimental setup was establishing a shot line using a laser aligned with the center line of the gun barrel. The dripper was then installed on an optical table and positioned to generate a droplet column intersecting the shot line. With a droplet size range selected, the appropriate dripper needle was installed and the syringe filled. The back pressure of the syringe barrel was then manually adjusted with the pneumatic controller to vary the spacing between droplets. Having fixed the droplet conditions, each one of the five cameras described earlier was installed and aligned as shown in Figure 42. A concentric square calibration target was used to obtain overlapping fields of view for the Kirana 5M and Phantom V2012s and provide an image resolution reference for post-test droplet sizing.

The speed of each projectile fired was controlled by the amount of gun powder used. For a given target speed, the amount of gun powder required was determined for each test by using the projectile's mass together with a powder load curve established by SwRI through extensive previous experimentation. Once the required amount of gun powder had been loaded and the gun fully prepared for firing, the dripper would be started remotely from a test room and a signal would be given to the gun operator to fire the projectile. A laser beam trigger was used to consistently initiate and synchronize the recording of the five cameras shown in Figure 42 for the tests.

One of the main challenges faced when running these experiments was successfully impacting the droplet column in each test. Even though the shot line had been carefully setup using an alignment laser and the dripper was positioned to have falling droplets intersect that line, the projectiles consistently deviated a small amount from their planned flight path. Depending on droplet size, the target column was also susceptible to swaying due to drafts in the laboratory and was never perfectly steady. These two factors combined caused the projectiles to graze the droplets sometimes or completely miss them a few times. Between both projectile designs, the conical one was significantly less reliable and had a 49% impact success in comparison to 94% of the blunt design. Since most of the useful experimental data collected was for the blunt design, only test results obtained with that projectile are discussed here.

Table 4 summarizes the test conditions for six exemplar tests performed with the blunt projectile. Nominal Mach 3 and Mach 5 flight conditions were targeted for these tests. The droplet sizes reported were obtained by averaging the measured horizontal and vertical diameters of all the droplets captured in the field of view an instant before interacting with the shock of the projectile (3 to 24 droplets). The uncertainty of the droplet size was determined based on the accuracy of the droplet diameter measurements (1-2 pixels). The impact location in the table describes the distance *r* between the center plane of the projectile and the droplet column plane, normalized by the projectile radius r_p as shown in the schematic in Figure 43. A sample bottom view of the projectile impacting the droplet column obtained in the experiments used to determine r/r_p is also included in the figure.

Table 4—Experimental conditions for selected test cases.

	Projectile Conditions			**Droplet Column Conditions**		
	Mach Number		**Speed**	**Droplet Size**		**Impact Location,** r/r_p
Case	Nominal	Actual	m/s	Nominal	Measured, μm	-
M3-S	3	3.1	1093	Small	228 ± 81	0.45
M3-M	3	3.0	1055	Medium	488 ± 65	0.35
M3-L	3	3.1	1077	Large	1418 ± 161	0.41
M5-S	5	5.2	1802	Small	315 ± 65	0.32
M5-M	5	5.0	1725	Medium	465 ± 61	0.54
M5-L	5	5.1	1765	Large	1565 ± 531	0.36

6.4 Shadowgraph Results

Figure 44 and Figure 45 show composite shadowgraph visualizations of droplets with three different sizes interacting with the shock flowfields generated by the projectiles listed in Table 4. These processed images were created by stitching together cropped sections of sequential frames captured with the ultra-high speed Kirana 5M. For the Mach 3 tests in Figure 44, frames captured every 2 μs were used to generate the sequences. For the Mach 5 results in Figure 45, frames captured every 1 μs where used but a few frames were skipped to preserve the same image size and scale of the Mach 3 sequences.

Several observations can be made from the artificial rain fields in Figures 44 and Figure 45 with regards to droplet breakup, but they all support one overarching fundamental result. In this study, droplet demise was characterized by mass stripping and shape deformation, but the degree to which those breakup mechanisms occurred for individual droplets was unique and dictated by local post-shock conditions and droplet size.

Droplets grazing the outer surface of the projectile had a very different breakup behavior in comparison to those crossing the conical shock away from it. Near the surface, where large velocity and density gradients

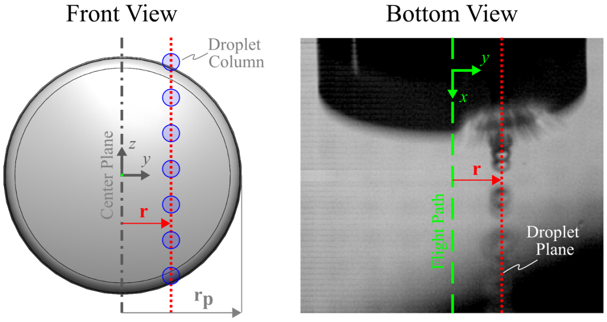

Fig. 43—Front view schematic of projectile and droplet column prior to impact illustrating reference distance r between projectile center plane and droplet column plane (*left*). Sample bottom view of projectile colliding with droplet column used to measure r (*right*).

occur within the shocked flow, distinct mass stripping was observed across all droplet sizes. Away from the surface, the amount of mass stripping decreased sharply and at some point far away enough from the projectile, did not occur.

Droplet flattening was a universal behavior observed after entering the shock layer for every droplet size and projectile Mach number tested, however, the speed at which this process advanced was droplet specific. For same sized droplets, faster flattening was observed closer to the surface than away from it. At the same radial distance, smaller droplets were flattened much earlier in comparison to larger droplets.

The amount of mass stripping and droplet deformation rate were different for every droplet in a given rain field, however, there were two behaviors consistently observed in every test. First, droplet deformation was oriented parallel to the local inclination of the shock front traversed. Droplets closest to the projectile surface developed a flat shape with an upright orientation close to vertical as a result of crossing a nearly normal shock front. At large radial distances, droplet flattening had a tilted orientation as a consequence of penetrating an oblique shock front. Second, through the flattening process, similar morphological changes were observed regardless of droplet size. Droplets first developed a lenticular shape characterized by a hemispherical windward surface and a flat leeward surface before becoming thin flat disks.

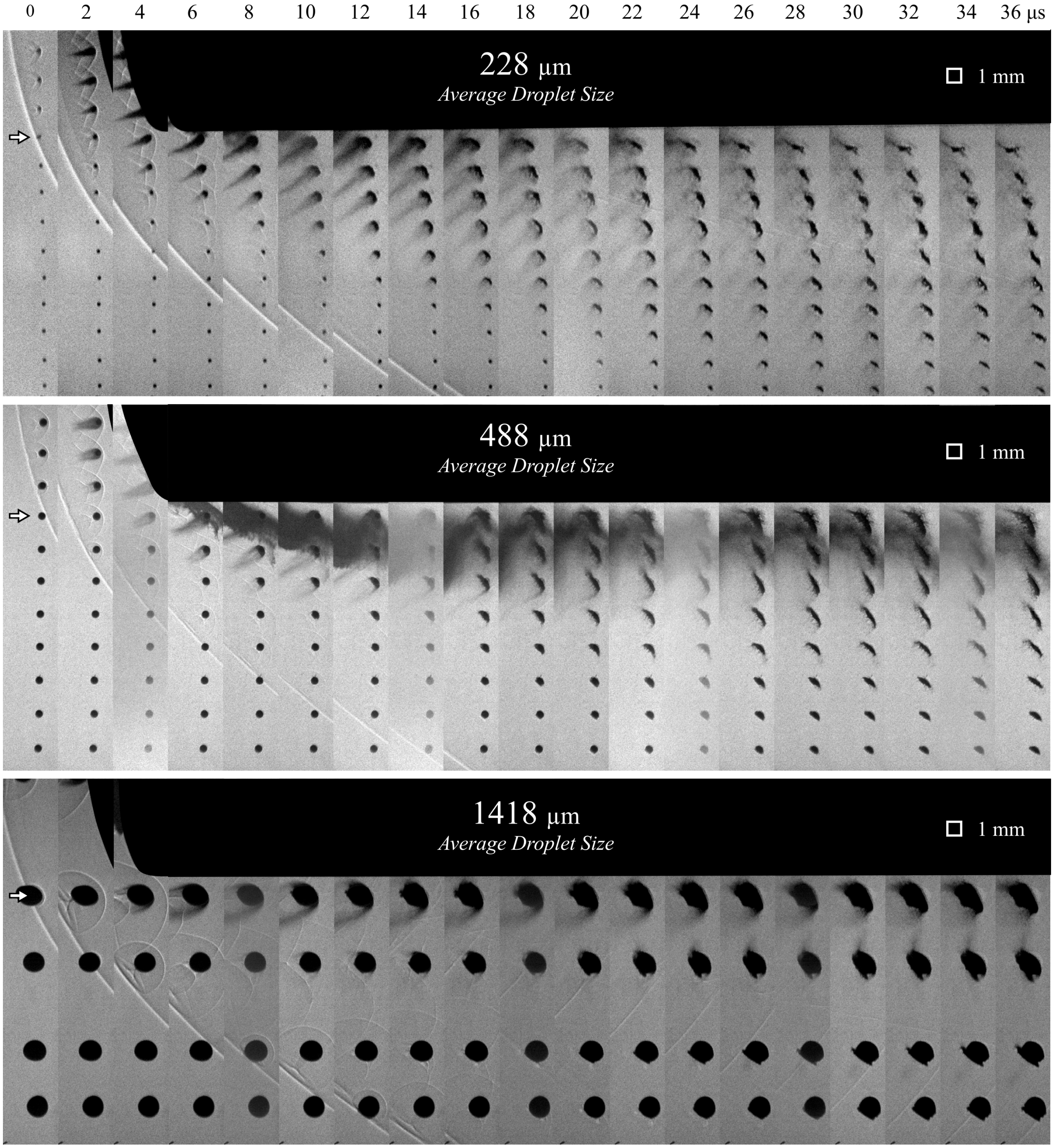

Fig. 44—Composite shadowgraph visualizations of droplet interaction with shock flowfield generated by a Mach 3.1 blunt projectile.

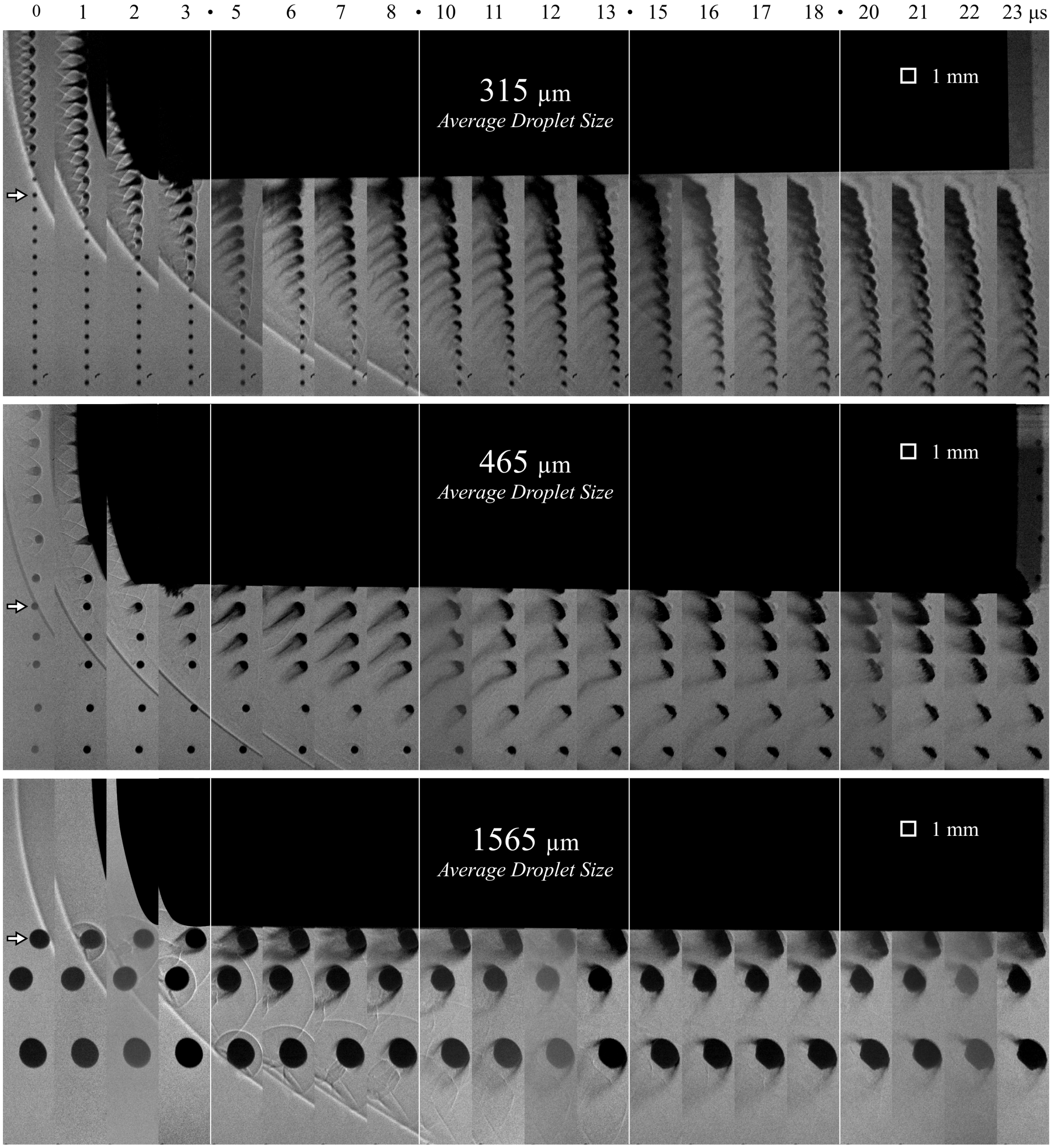

Fig. 45—Composite shadowgraph visualizations of droplet interaction with shock flowfield generated by a Mach 5.1 blunt projectile. The vertical white lines in the rain fields presented indicate a missing frame in the sequence.

6.5 Practical Implications

From the results in this study, it can be inferred that droplet breakup across a conical shock is a complex process that is mainly governed by the location of shock penetration and droplet size. Breakup is fastest for small droplets crossing a steep shock-front near a stagnation region. In contrast, breakup speed is significantly reduced for larger droplets interacting with the post-shock gas behind an oblique front. Shock layer transit time however also plays an important role in droplet breakup. Long transit times favor breakup because they allow mass stripping, flattening, and fragmenting to advance prior to impact.

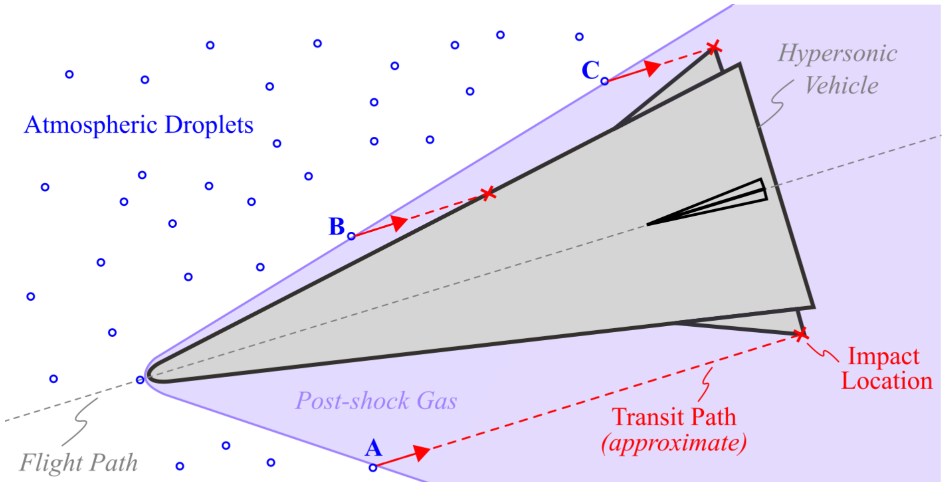

Fig. 46—Schematic of hypersonic vehicle flying through weather in terminal dive phase illustrating transit paths for different droplets.

These results have a key implication for a hypersonic vehicle flying through weather in its terminal dive phase as shown schematically in Figure 6. In the expected pitched-down position for that final flight segment, the leading edge shock is particularly asymmetric and is much closer to the vehicle on its windward side than on its leeward side. As a result, shock layer transit times before reaching a surface are substantially reduced for a droplet such as B in comparison to a droplet such as A. Shorter transit times cause droplet breakup to advance less, which increases the potential for vehicle damage to occur. As shown in the experimental results of this study, breakup speed is inversely proportional to droplet size, so large droplets with short transit times are particularly concerning, more so if they impact a control surface such as a back fin (droplet C). Note also that as a consequence of the asymmetric leading edge shock and shorter droplet transit times through it, increased surface damage is expected to occur along one side of the vehicle. Asymmetric surface damage along the vehicle planform is also undesirable if it affects vehicle aerodynamics and flight control.

Finally, the experimental results shown in this study also demonstrated how droplet flattening was orientated parallel to the local shock front penetrated. In a practical scenario and for large enough droplets that don't fully disintegrate before reaching the vehicle, surface impacts will occur with disk-shaped droplets that are not aligned with the collision surface. This will affect how droplet fluid spreads along the impact surface and therefore the normal and shear stress exerted. Future experiments investigating surface erosion of hypersonic vehicles due to weather encounters should therefore attempt to characterize the impact physics of flattened droplets.

7. HIGH-FIDELITY SIMULATIONS OF DROPLET-BOW SHOCK INTERACTIONS

Significant amounts of information about the interaction of droplets with normal shocks can be found in existing literature, both computational and experimental. The flow around a hypersonic vehicle is more complex than a normal shock, containing oblique shocks, curved shocks, boundary layers, and other nonuniform flow patterns. Experimental data on the interaction of droplets with these types of super/hypersonic flows is difficult to obtain, and thus a role exists for high-fidelity numerical simulations to augment and improve the available data sets. In pursuant to this goal, a set of resolved Eulerian-Eulerian droplet simulations were executed to gain a qualitative understanding of the interactions of typical atmospheric droplets with a vehicle-generated curved bow shock. This chapter presents the resulting conclusions about the effect of droplet diameter and freestream Mach number on a droplet's structural integrity upon impact.

7.1 Numerical Method

We use an Eulerian-Eulerian approach by employing the compressibleInterFoam solver implemented in OpenFOAM [81]. This solver models compressible two-phase flow problems using a pressure based, immiscible volume of fluid (VoF) method via finite volume discretization. A single set of governing equations define the behavior of the mixture, the properties of which are calculated as a phase fraction weighted average of the properties of component fluids. Here the phase fraction, denoted α, is defined such that cells containing entirely liquid water have a value of 1 and cells that are entirely air have a value of 0. Cells in the interface region have an intermediate value that corresponds to the volume fraction of liquid water contained in the cell. This defines the interface in a diffuse manner while the physical liquid-gas interface would be sharp. Thus for analysis we consider the physical interface to exist at the contour where $\alpha = 0.5$.

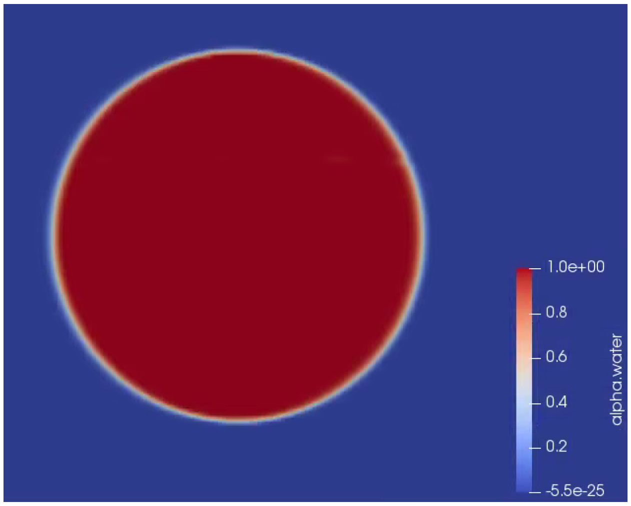

Fig. 47—2D cut plane of the phase fraction field, α, showing the initial condition of a water droplet. $\alpha = 1$ inside the liquid droplet, $\alpha = 0$ in the surrounding gas phase, and $0 < \alpha < 1$ in the interface region.

The range of scales in the system represents a major difficulty in simulating atmospheric droplets ($< 10^{-3}$m) interacting with complex, vehicle scale flows ($> 10^{-2}$m). Based on previous works such as that by Meng & Colonius [82], we consider $d_{drop}/100$ to be the maximum cell size that will reasonably capture the transport and general breakup of a droplet. For droplets in our target range of 100 - 1000μm, this works out at the low end to a 1μm cell size which if applied uniformly to a vehicle scale domain would generate cell counts that are simply impossible to compute. To loosen this restriction we elect to use adaptive mesh refine (AMR) with dynamic load balancing which is natively supported by OpenFOAM. This allows us to resolve the bulk of the domain to a level that is sufficient for the background flow but still too coarse for the droplet. Cells in and around the droplet are then iteratively subdivided to achieve the cell size necessary to resolve the droplet. Since we are investigating the interaction of droplets with shocks, we also refine the shock to the same resolution as the droplet. It should be noted that while we expect this level of resolution to capture the macro scale evolution of the droplets, it is not sufficient to capture the finer details of the breakup process. At this stage we are only concerned with predicting the effects of the bow shock interaction on the parent droplets and if said effects will be enough to significantly affect the impact event. So we deem the cost savings from the relatively coarse resolution worth the loss in accuracy.

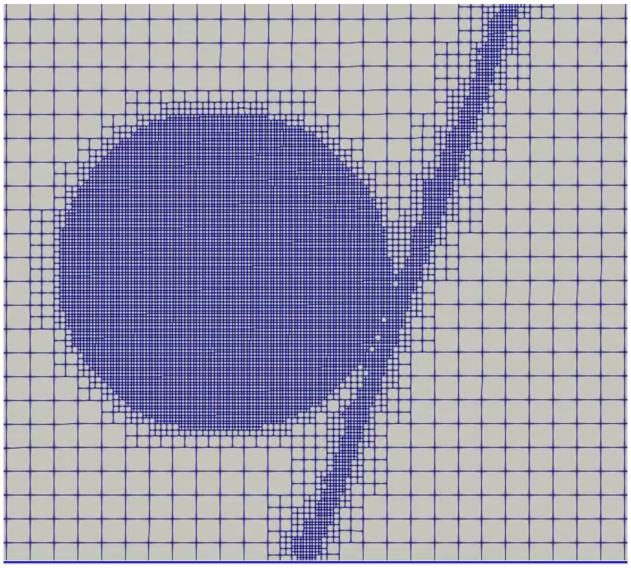

Fig. 48—2D cut plane demonstrating the mesh refinement as a droplet approaches a shock from the left.

We use two conditions based on scalar metrics to determine if a cell should be refined. The metrics are updated and conditions reevaluated at every time step and if any are met, the given cell is refined. If none of the conditions are met, the cell is marked for unrefinement. The first condition resolves the droplet by refining any cell with of $\alpha > 0.001$. The second condition resolves the shock by refining any cell where the relative pressure change across the cell exceeds a specified threshold which we set at 0.1, $\Delta p/p > 0.1$.

7.2 Physical Model

Our investigation focuses on singular droplets that collide with the bow shock generated by a cylindrical blunt body. The droplets are made of water and in a background gas of air with farfield conditions assumed to be equal to standard atmospheric values at an altitude of 3 kilometers. This altitude was chosen as it overlaps both where suspended water droplets can be found and where a vehicle could be expected to travel at hypersonic speeds. For comparison we vary the droplet diameter and freestream mach number.

For the purpose of limiting computational cost, we assume that the flow is symmetrical across the stagnation line and the effect of downstream and wake structures are negligible for our current investigation.

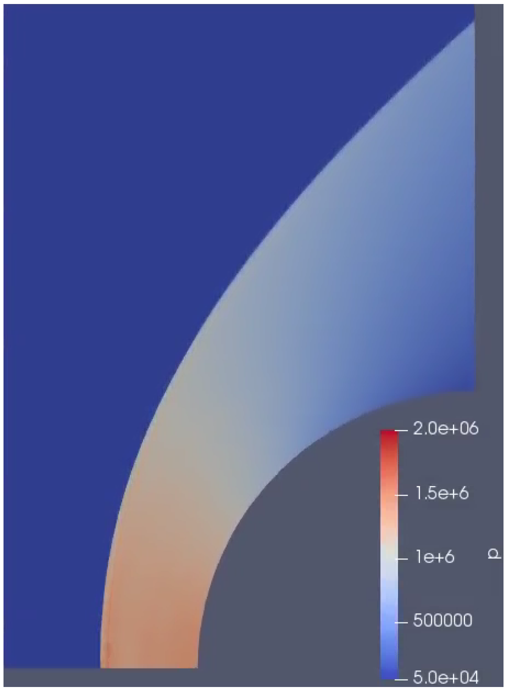

Fig. 49—2D cut plane of the pressure field generated ahead of a 1cm diameter cylinder in Mach 4 flow.

As such we limit the initial offset of the droplets from the symmetry line to between $r_{cyl}/4$ to r_{cyl} to avoid approaching these boundary regions. The width of the domain along the cylinder's axis is sized to be at least $6d_{drop}$ which, while insufficient to entirely avoid boundary effects, is enough to prevent direct interactions with the droplet generated shock and wake fields.

Figure 49 shows the pressure field ahead of a 1cm, adiabatic, no-slip, cylindrical wall in Mach 4 conditions. We generate the bow shock for each set of flow conditions by simulating the pure gas phase flow without AMR. Once an acceptably steady state has been reached, we use this solution as the initial state of the gas phase for each droplet simulation. We then activate the AMR with settings relevant to the size of the droplet to be simulated. This leads to a sudden and significant refinement of the shock as previously discussed, which generates numerical noise. The simulation is again run until this noise has cleared and an acceptably steady state is achieved. Then the droplet is inserted by modifying the phase fraction field in the desired starting location upstream of the shock. The simulation is then run until the droplet or its remnants reach the cylinder's surface.

7.3 Results

Our previous work, [83] led us to question the validity of traditional Lagrangian droplet breakup models, such as Kelvin-Helmholtz Rayleigh-Taylor (KHRT), when shocks and highly variable flow fields are involved. In particular, we saw indications that such models tended to predict near instantaneous, catastrophic breakup in the bow shock region. The highly restrictive nature of these models and limited existing experimental data involving non-normal shocks led us to believe these predictions may be questionable. Thus we set out to verify the validity of such models through resolved Eulerian-Eulerian simulation of droplet-bow shock interactions.

Here we investigate the droplet-shock interaction with a cylinder generated bow shock involving multiple droplet sizes (100-1000μm) and freestream Mach numbers (2-4). We selected a cylinder diameter of 1 cm to represent a small but still macro scale leading edge that could be expected to be present on a flight vehicle. For bow shocks in our desired range, a straight line trajectory between the bow shock and cylinder surface has a corresponding minimum travel time of a few μs. This leaves a narrow window for a droplet to deform, breakup, and/or divert before impact. Generally, droplet breakup time scales proportionally to the droplet diameter. So we expect there to be three general regimes corresponding to droplet size and the other listed factors where the droplet will be intact, highly deformed/reduced, or completely broken up before impact. We seek to understand where these regimes lie and the best way to define them based on the relevant factors.

7.3.1 Eulerian-Eulerian Simulations

After generating a sufficient steady base flow, like that shown in Fig. 49, the droplets are introduced directly in front of the bow shock with an offset of 3.75mm (0.75 R_{cyl}) from the symmetry plane. This aligns them with the highly complex and variable region of the bow shock that can neither be described by normal shock or oblique shock relations. As such it represents a significant unknown in regards to predicting how the droplet will behave. In Fig. 50 we present a 250μm water droplet interacting with the post shock flow Mach 4 bow shock. The flow surrounding the droplet is complex and asymmetric as the droplet and gas velocity vectors are not collinear. The droplet itself is deforming and losing mass to shear stripping. In Fig. 51 the droplet approaches the cylinder's surface. It has deformed into an oblate profile and while having experienced a moderate amount of breakup, still retains a large amount of its core mass. As such, the exact nature of the impact and the potential for damage may be noticeably different than if retained its base spherical state. We define this state to be the middle or transitory regime.

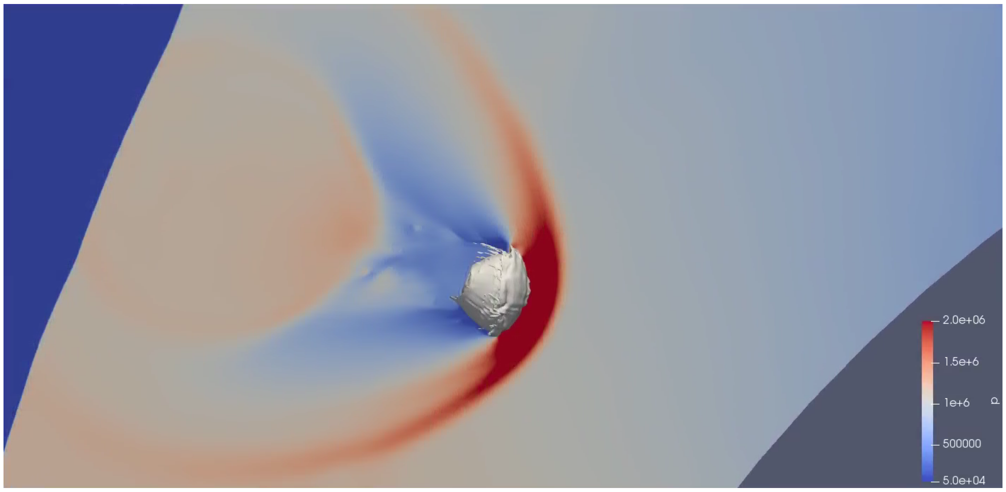

Fig. 50—250μm droplet in the bow shock of a 1cm cylinder in Mach 4 conditions and starting from a height of 3.75mm from the symmetry plane. The background is a 2D cut plane of the pressure field of the surrounding air. The isosurface is calculated from the phase fraction at $\alpha = 0.5$, corresponding to the surface of the liquid phase droplet.

In Figs. 52 – 53 we visualize the breakup process for some of the droplets we simulated. The samples at evenly spaced time intervals from the droplets introduction in front of the bow shock to just before impact

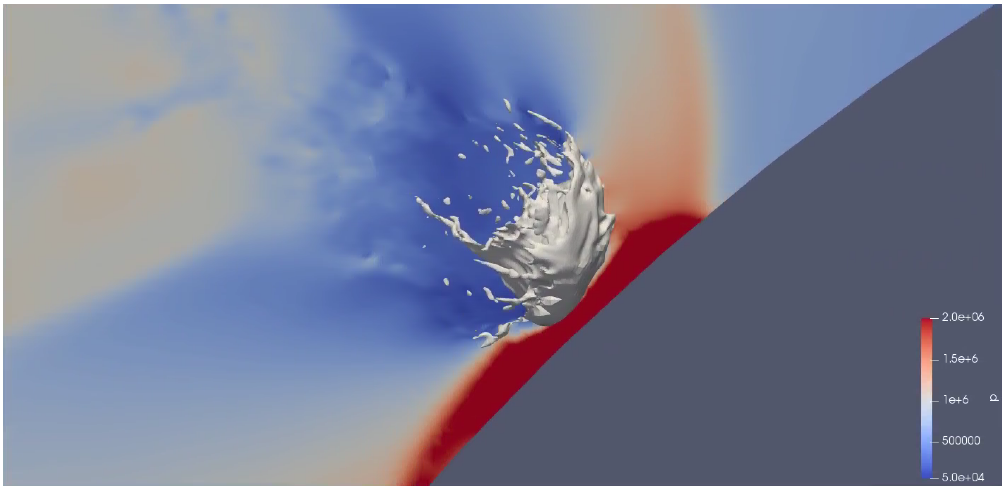

Fig. 51—The same droplet in Fig. 50 shortly before impact with the cylinder surface.

with the surface. Note that scaling between sets is not strictly maintained. Within the current scope, we draw our main conclusions from the state of the droplet directly before impact (right side of plots). Thus referring to Fig. 52, (a) demonstrates what we believe to be nearly complete breakup state, (b) demonstrates the intermediate state, and (c) demonstrates the effectively intact state.

7.3.2 Theoretical Analysis

To build a basis to tie our simulation results back to known theory, we begin by employing the work of Sinclair and Cui [84]. They developed theoretical models to predict the bow shock standoff distance (δ) for cylinders with CFD and experimental validation. Their resulting equations can be summarized as follows:

$$\frac{\delta}{D_{cyl}} = \frac{\beta_s^2}{\theta_s^2 \cos\beta_s} \sqrt{\frac{2+(\gamma-1)M_\infty^2}{2\gamma M_\infty^2 - \gamma + 1}}, \tag{48}$$

and

$$\frac{\delta}{D_{cyl}} = \frac{\beta_s^2}{\theta_s^2 \cos\beta_s} \frac{2+(\gamma-1)M_\infty^2}{(\gamma+1)M_\infty^2}. \tag{49}$$

Each model uses a different assumption for closure. Equation (48) assumes linear variation of Mach number between the shock and body while Eq. (49) assumes linear variation of density instead. The former is considered more accurate for high Mach numbers so we employ it in our subsequent analysis but present both as the latter is also valid. For completeness we also include the necessary supporting equations for θ_s, β_s, C_{ps}, and $C_{p,max}$. Details of their purpose and derivations can be found in the original work.

$$\theta_s = \frac{\pi}{2} - \beta_s \tag{50}$$

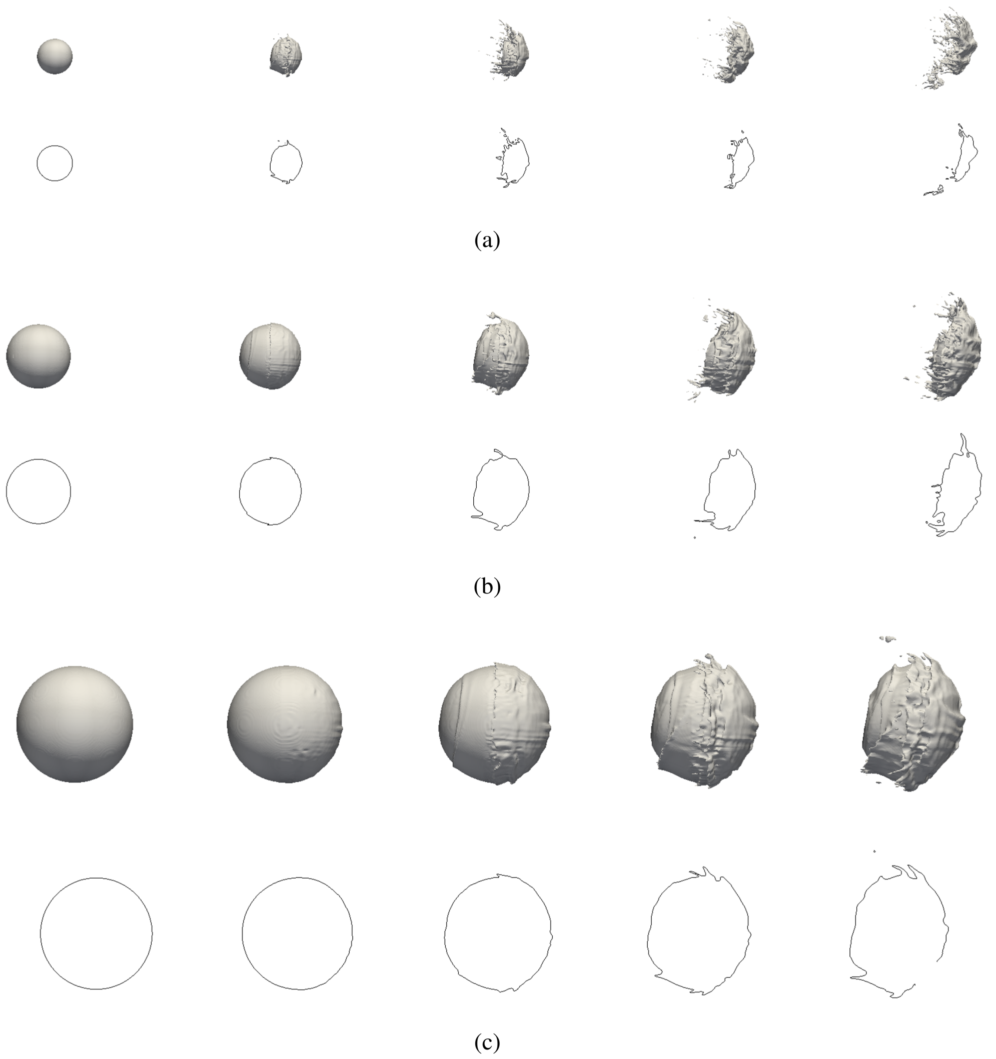

Fig. 52—Progression of the droplet breakup process from initial shock contact (left) to just prior to impact (right) for a Mach 2 bow shock generated by a 1 cm cylinder. Droplets are offset 3.75 mm (0.75 R_{cyl}) from the stagnation line. Both the isosurfaces and contour plots correspond to $\alpha = 0.5$. Droplet diameters: (a) $250\mu m$, (b) $500\mu m$, and (c) $1000\mu m$.

$$\beta_s = \frac{\pi}{2} - \sin^{-1}\sqrt{\frac{C_{ps}}{C_{p,max}}} \tag{51}$$

$$C_{ps} = \frac{2}{\gamma M_\infty^2}\left\{\left(\frac{\gamma+1}{2}\right)^{-\frac{\gamma}{\gamma-1}}\left[\frac{(\gamma+1)^2 M_\infty^2}{4\gamma M_\infty^2 - 2(\gamma-1)}\right]^{\frac{\gamma}{\gamma-1}}\left[\frac{1-\gamma+2\gamma M_\infty^2}{\gamma+1}\right] - 1\right\} \tag{52}$$

$$C_{p,max} = \frac{2}{\gamma M_\infty^2}\left\{\left[\frac{(\gamma+1)^2 M_\infty^2}{4\gamma M_\infty^2 - 2(\gamma-1)}\right]^{\frac{\gamma}{\gamma-1}}\left[\frac{1-\gamma+2\gamma M_\infty^2}{\gamma+1}\right] - 1\right\} \tag{53}$$

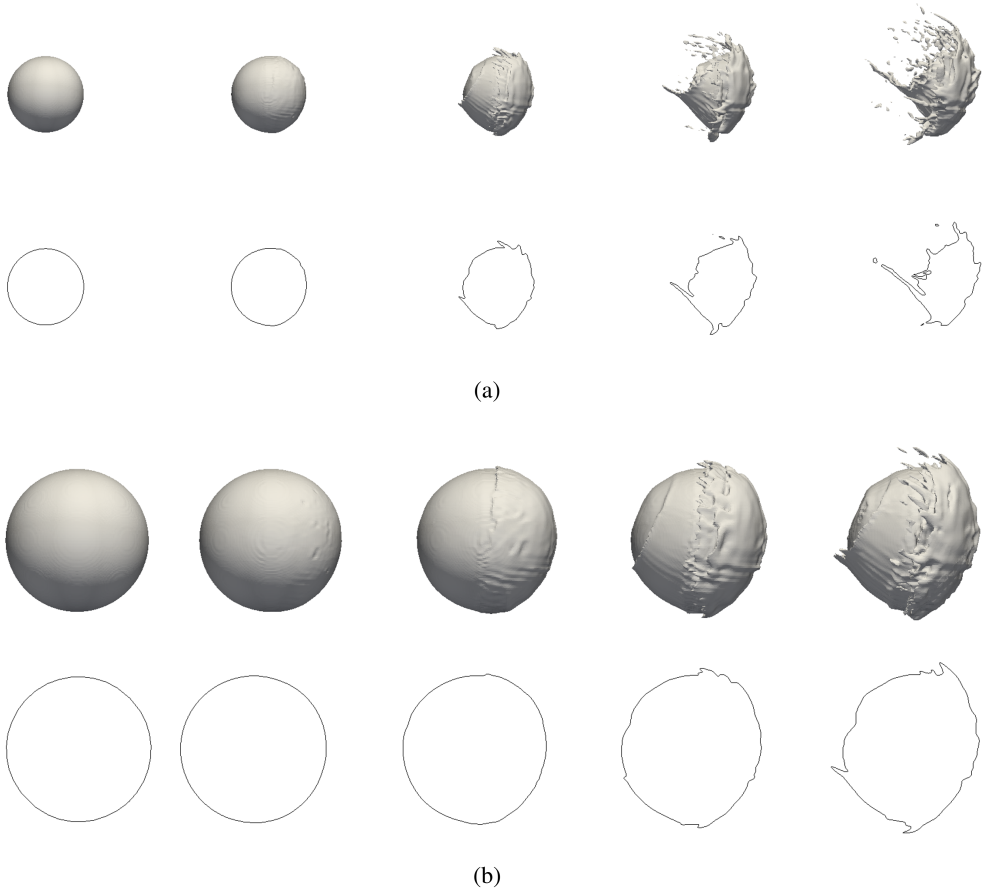
(a)

(b)

Fig. 53—Progression of the droplet breakup process from initial shock contact (left) to just prior to impact (right) for a Mach 4 bow shock generated by a 1 cm cylinder. Droplets are offset 3.75 mm (0.75 R_{cyl}) from the stagnation line. Both the isosurfaces and contour plots correspond to $\alpha = 0.5$. Droplet diameters: (a) $250\mu m$ and (b) $500\mu m$.

We plot both equations, along with our own CFD results in Fig. 54. Our results fall within the envelope of the two models both lending validity to our simulations and implying that we can safely use Eq. (48) for standoff distance predictions.

The minimum transit time from the shock to the surface is proportional to the bow shock standoff distance. Roughly speaking, standoff distance is inversely proportional to freestream Mach number, thus $t_{transit,min} \propto \frac{\delta}{M_\infty} \propto \frac{1}{M_\infty^2}$. Longer transit times increase the likelihood of breakup before impact by allowing the deformation and breakup processes to proceed further. Using Eq. (48) we estimate $t_{transit}$ as $t_{transit} = \frac{\delta}{v_\infty}$.

In Chapter 4, we introduced several breakup models that predict a discrete breakup event: the Taylor Analogy Breakup (TAB) [75], Nonlinear TAB (NTAB) [70], and Rayleigh-Taylor (RT) [77] models. Figure 55 compares the breakup times predicted by these models as they vary with droplet diameter for a fixed freestream Mach number. We estimate the post shock conditions using the normal shock relations for an ideal gas and assuming the post shock velocity is zero so the relative velocity is equal to the freestream velocity. While they obviously produce significantly different predictions, the maximum difference is less than an order of magnitude so in our qualitatively oriented analysis we consider them all equally valid. Note

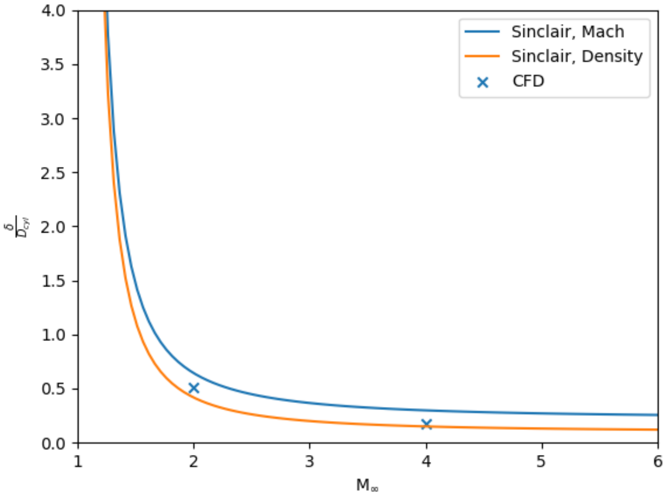

Fig. 54—Non-dimensional standoff distance vs. freestream Mach number. The point data corresponds to our computational results while the lines are models for cylinders developed by Sinclair and Cui [84] and repeated here as Eqs. (48) – (49).

that here we use a standard spherical drag model to calculate the drag forces that drive the RT based breakup. Previously we favored using the time averaged, Wiegand model [74] due to the convenience of not requiring an additional deformation model. However, this time averaged nature leads the Wiegand model to over predict the instantaneous drag forces. Since the RT breakup is driven by the drag force, the over predicted drag forces lead to an over prediction of the RT breakup rate and thus under prediction of breakup time, by roughly two orders of magnitude in our case. The spherical model avoids this issue and in the case of bow shocks, the distance to the surface is short so the droplet remains approximately spherical for a significant portion of the travel time.

The rates of relative mass loss and deformation of a droplet tend to be inversely proportional to droplet diameter. Larger droplets have more mass to lose and inertia to overcome as explained by the square-cube law. Thus the overall breakup time tends to be proportional to droplet diameter in our selected models. In other words, we would expect that for a given set of flow conditions the stability of a droplet decreases with decreasing droplet diameter.

Breakup time is generally inversely proportional to relative velocity. Thus higher freestream Mach numbers would be expected to lead to faster breakup and a lower likelihood of impact. However, since standoff distance also decreases with increasing freestream Mach number, lowering the transit time and increasing the likelihood of impact. These opposing effects make the overall effect of varying Mach number not obviously apparent due to the unknown relative magnitude of each factor.

In Fig. 56 we visually compare the theoretical minimum transit time to the predicted breakup time for our three models over a range of Mach numbers. For additional clarity we include the differentials of $t_{transit}$ and $t_{breakup}$, $\Delta t = t_{transit} - t_{breakup}$. When Δt is positive, breakup is predicted to occur before impact with the opposite occurring it is negative. We propose considering the conditions where $\Delta t = 0$ to be a critical

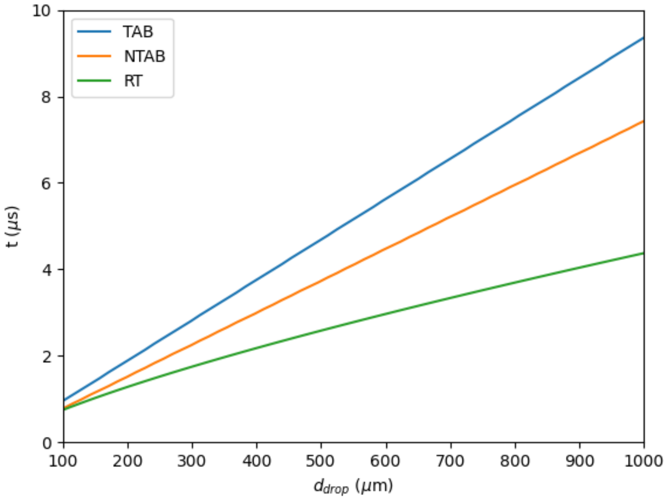

Fig. 55—Droplet breakup time vs droplet diameter as predicted by the TAB, NTAB, and RT breakup models.

point, such that breakup is predicted to occur at the exact time of impact. By plotting these values we can construct a sort of phase diagram that allows us to qualitatively estimate the droplet state at impact for any given combination of freestream Mach number and droplet diameter.

The result of the preceding analysis is Fig. 57. Here we visualize the expected breakup across the Mach number and droplet diameter space. The lines correspond to the analytical predicts derived from our selected theoretical models and the points are from our Eulerian-Eulerian droplet simulations shown in Section 7.3.1. Due to the high costs involved, we only have limited number of datapoints from our simulations. However it is clear that it matches well with the theoretical predictions, especially from TAB and NTAB. Thus we propose it is reasonable to use this theoretical basis for further analysis, including a larger range of parameters such as the effect of cylinder diameter, gas properties, and droplet material properties. Carefully employing more expensive computational and experimental resources for targeted validation instead of blanket studies.

Interpreting these results, conditions lying sufficiently up and to the right of the critical curves imply the droplet is likely to undergo minimal deformation and breakup. Meaning that it may be safe to apply the assumption that the droplet will be spherical upon impact when preparing models or experiments for surface erosion. For conditions on and near the critical curves, the droplet will be highly deformed but potentially still have a relatively intact core. Thus making predictions of deformation and breakup necessary, limiting the possible range of simplifying assumptions. Finally, if the conditions are sufficiently left and below the critical curves, the droplet will likely have undergone a significant amount of breakup where the core of the parent droplet has completely disintegrated. For sufficiently small child droplets and including the effects of evaporation, it may become reasonable to make significant assumptions. One possibility being to assume the droplet has completely evaporated and thus gas phase only modeling based on mass flow rates can be used.

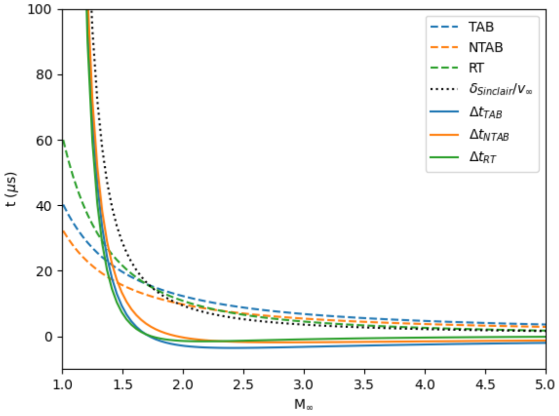

Fig. 56—Comparison of modeled breakup times to minimum transit time for varying Mach with a fixed droplet diameter, $d_{drop} = 500\mu m$. The curves labeled Δt correspond to $\Delta t = t_{transit} - t_{breakup}$, for the respective model. Positive values of Δt indicate breakup is expected to complete before impact and opposite for negative values.

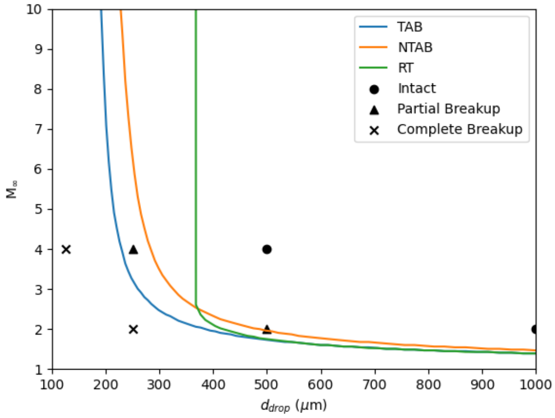

Fig. 57—Phase regimes predicting droplet state upon impact with a 1 cm cylinder. Above curve = impact before breakup. Below curve = breakup before impact.

8. SUMMARY AND CONCLUSIONS

Historically, the prediction of the erosion potential of objects traveling at supersonic and hypersonic speeds through fields of hydrometeors has been performed using models that rely on a set of correlations for droplet demise derived from normal shock-droplet interaction experiments. This condition is likely to be a reasonable approximation of the flow only in the immediate vicinity of leading edge or nosetip of the vehicle. In reality, hydrometeors will encounter a highly non-uniform flow environment under which these correlations are not likely to be valid and may lead to inaccurate erosion predictions on the vehicle forebody and on other important structures such as stabilization fins and control surfaces.

A more complete understanding of the influence of the flow on the hydrometeor fate and transport is therefore necessary. One approach is to directly track individual hydrometeors as they traverse through a pre-computed, vehicle-specific flow field. While this approach has the potential to provide a more physically-realistic assessment of the likelihood of hydrometeor impact, the methodology relies on a different set of modeling assumptions that must ultimately be obtained and validated. The primary motivation behind this approach is that these types of models have the ability to respond to the *local* flow conditions, making them aware of field-induced deformation and breakup behavior. A variety of existing models for droplet deformation-induced drag and aerodynamic breakup were tested in a canonical supersonic flow field, and a wide variety of droplet behaviors were observed resulting in unacceptable levels of uncertainty for the impact potential. Reducing this uncertainty will require a combination of high-fidelity multi-fluid simulations as well new, relevant, experimental studies that allow us to obtain a detailed look at the behavior of hydrometeors under high-Mach-number and high-Weber-number flow environments. In this report, we considered four different approaches for obtaining this data.

The first approach was to inject droplets into a supersonic wind tunnel facility and record their subsequent interaction with the flow field generated by a relevant test article. A number of technical challenges associated with this approach have been identified, including the acceleration of the droplets to the gas velocity, the potential for premature droplet breakup events, the potential for droplet freezing in the wind tunnel throat, and the risk of undesired erosion of the tunnel components. These challenges, along with a preliminary scoping study, were discussed in Chapter 3, with the main conclusion being that such experiments would not reproduce realistic interaction environments in NRL's prototype small-scale tunnel facility. Testing in NRL's new Hypersonic Wind Tunnel facility was not possible during this program, due to a confluence of unforeseen acquisition delays.

The second approach considered the interaction of a droplet with a spherical shock wave created by a propagating detonation. This approach is similar in nature to past shock-tube experiments in which a planar shock wave interacted with a suspended droplet. The change in shock structure from planar to spherical modifies the post-shock flow field, establishing a variable velocity environment through which the droplet must traverse. High-speed shadowgraph imaging was used to provide a time-resolved history of droplet demise. These efforts were discussed in Chapter 5, and provide a limited set of droplet demise data.

The third approach considered the interaction of a stream of droplets with a supersonic projectile. A series of test shots were performed at a ballistic range operated by the Southwest Research Institute using projectile with both blunt and conical forebodies traveling at speeds that varied between Mach 3 and 5 and were discussed in Chapter 6. Simultaneous high-speed photography and shadowgraphy recorded the interaction of precisely-control droplets in free fall with the bow shocks created by these projectiles. High resolution images track the deformation and demise of the droplets, showing the strong influence of the local flow on the droplet behavior.

The fourth approach utilized high-resolution two-fluid simulations to compute the interaction of a water droplet with the bow shock formed around a blunted supersonic body. These simulations, discussed in Chapter 7, provided a detailed view of the droplet deformation under various flow conditions along with the formation of fluid dynamic instabilities on the droplet surface that resulted in mass stripping and, in some cases, complete droplet breakup. The breakup times predicted by these simulations were then compared to those predicted by the TAB and RT breakup models discussed in Chapter 4. This analysis identified a range of Mach number-droplet diameter combinations for which prediction of droplet impact vs demise is likely to be sensitive to the underlying breakup model.

Future efforts will be required to expand the scope of droplet trajectory and demise data beyond the range of conditions considered in this study. A thorough analysis of the data can then be performed to refine droplet deformation and drag models as well as aerodynamic breakup models for the critical flow regimes identified as part of this effort. Incorporation of such improved models into erosion prediction tools and CFD software, such as the JENRE® Multiphysics Framework, will provide a more accurate assessment of hydrometeor-induced erosion potential for hypersonic vehicles.

ACKNOWLEDGEMENTS

This work was supported by the Naval Research Laboratory's 6.2 Base Program. Computational resources were provided by the DoD High Performance Computing Modernization Program, and the authors would like to sincerely express their gratitude for this support. We would also like to acknowledgement support provided by Prof. Kenneth Yu and Minwook Chang from the University of Maryland in setting up the linear model detonation experiments (LDME) discussed in Chapter 5, as well as Prof. Terrence Myers and Brandon W. Yant from Purdue University and Dr. Nicholas Mueschke, Dr. Daniel Portillo, and Joseph Elizondo from the Southwest Research Institute for their assistance in operating the ballistic range experiments described in Chapter 6.

REFERENCES

1. K. Mohanakumar, *Stratosphere Troposphere Interactions, An Introduction* (Springer, 2008).
2. M. D. King, S. Platnick, W. P. Menzel, S. A. Ackerman, and P. A. Hubanks, "Spatial and Temporal Distribution of clouds Observed by MODIS Onboard the Terra and Aqua Satellites," *IEEE Transactions on Geoscience and Remote Sensing* **51**(7), 3826–3852 (2013).
3. N. E. Observatory, *NASA Earth Observatory - Cloud Fraction*, 2020 (accessed May 28, 2020)). URL `https://neo.sci.gsfc.nasa.gov/view.php?datasetId=MYDAL2_M_CLD_FR`.
4. P. K. Wang, *Physics and Dynamics of Clouds and Precipitation* (Cambridge University Press, Cambridge, UK, 2013).
5. "Military Standard Climatic Information to Determine Design and Test Requirements for Military Systems and Equipment," Military Standard MIL-STD-210C, Department of Defense, Washington, DC, 1987.
6. P. Tattelman and P. Willis, "Model Vertical Profiles of Extreme Rainfall Rate, Liquid Water Content, and Drop-Size Distribution," Technical Final Report AFGL-TR-85-0200, AD-A164 424, Air Force Geophysics Laboratory, Hanscom Air Force Base, MA, 1985.
7. D. Brunt, *Physical and Dynamical Meteorology* (Cambridge University Press, 2011).
8. A. Chandrasekar, *Basics of Atmospheric Science* (Phi, 2010).
9. M. Jacobson, *Atmospheric Pollution: History, Science, and Regulation* (Cambridge University Press, 2002).
10. J. Oliver, *Encyclopedia of World Climatology* (Springer, 2005).
11. P. Lax and S. Leonov, "A 1-D Model for Condensation Onset in Hypersonic Wind Tunnels with Gas-Phase Impurities," *AIAA Aviation 2019 Forum,DOI: 10.2514/6.2019-3091* (2019).
12. J. Iribarne and H. Cho, *Atmospheric Physics* (Springer Netherlands, 2012).
13. C. O'Dowd and P. Wagner, *Nucleation and Atmospheric Aerosols: 17th International Conference, Galway, Ireland, 2007* (Springer Netherlands, 2007).
14. P. Hobbs, *Ice Physics* (Oxford University Press, 2010).
15. J. Field, C. Seward, C. Pickles, E. Coad, and M. Watt, "Studies of Rain Erosion Mechanisms in a Range of IR Transmitting Ceramics - Including Coated Samples," University of Cambridge, Cambridge, UK, 1994.
16. K. Saha, *The Earth's Atmosphere: Its Physics and Dynamics* (Springer Berlin Heidelberg, 2008).
17. J. Marshall and W. M. Palmer, "The Distribution of Raindrops with Size," *Journal of Meteorology* **5**, 165–166 (1948).
18. A. Cole, R. Donaldson, R. Dyer, A. Kantor, and R. Skrivanek, "Precipitation and Clouds: A Revision of Chapter 5, Handbook of Geophysics and Space Environments," Air Force Survey in Geophysics AFCRL-69-0487, Air Force Cambridge Research Laboratories, Bedford, Massachusetts, 1969.

19. N. Sissenwine, “Extremes of Hydrometeors at Altitude for MIL-STD-210B,” Scientific Report AFCRL-72-0369, Air Force Cambridge Research Laboratories (LKI), Bedford, MA, 1972.

20. P. Willis and P. Tattelman, “Drop-Size Distributions Associated with Intense Rainfall,” *Journal of Applied Meteorology* **28**(1), 3–15 (1989).

21. D. Jorgensen, *Mesoscale and Convective-Scale Characteristics of Mature Hurricanes*, Phd dissertation (Colorado State University, 1984).

22. E. Szoke, E. Zipser, and D. Jorgensen, “A Radar Study of Convective Cells in Mesoscale Systems in GATE, Part 1: Vertical Profile Statistics and Comparison with Hurricanes,” *Journal of Atmospheric Sciences* **43**(2), 182–198 (1986).

23. J. Urzay, “Supersonic Combustion in Air-Breathing Propulsion Systems for Hypersonic Flight,” *Annual Review of Fluid Mechanics* **50**, 593–627 (2018).

24. J. Maxwell, *Morphing Waveriders for Atmospheric Entry*, PhD dissertation (University of Maryland, College Park, 2019).

25. W. G. Reinecke and G. D. Waldman, “A Study of Drop Breakup Behind Strong Shocks with Applications to Flight,” Technical Final Report SAMSO-TR-70-142, AD871218, Space and Missile Systems Organization, Norton Air Force Base, CA, 1970.

26. O. Engel, “Fragmentation of Waterdrops in the Zone Behind an Air Shock,” *Journal of Research of the National Bureau of Standards* **60**(3), 245–280 (1958).

27. A. Ranger and J. Nicholls, “Aerodynamic Shattering of Liquid Drops,” *AIAA Journal* **7**(2), 285–290 (1969).

28. W. G. Reinecke and W. McKay, “Experiments on Water Drop Breakup Behind Mach 3 to 12 Shocks,” Preliminary Technical Report SC-TR-70-6063, Sandia Corporation, 1969.

29. M. Pilch and C. Erdman, “Use of Breakup Time Data and Velocity History to Predict the Maximum Size of Stable Fragments for Acceleration-Induced Breakup of a Liquid Drop,” *International Journal of Multiphase Flow* **13**(6), 741–757 (1987).

30. T. Theofanous, G. Li, T. Dinh, and C. H. Chang, “Aerobreakup in Disturbed Subsonic and Supersonic Flow Fields,” *J. Fluid Mech* **593**, 131–170 (2007).

31. T. Theofanous, “Aerobreakup of Newtonian and Viscoelastic Liquids,” *Annual Review of Fluid Mechanics* **43**, 661–690 (2011).

32. W. G. Reinecke, G. D. Waldman, and W. L. McKay, “Shock Layer Shattering of Ice Crystals with Applications to Reentry Flight,” Final Report AFML-TR-77-7, AD B019951, Air Force Materials Laboratory, Wright-Patterson Air Force Base, OH, 1977.

33. W. G. Reinecke, G. D. Waldman, W. L. McKay, and M. B. Ziering, “Shock Layer Shattering of Water Drops and Ice Crystals in Reentry Flights,” Technical Final Report AFML-TR-75-71, AD B006836, Air Force Materials Laboratory, Wright-Patterson Air Force Base, OH, 1975.

34. R. Brodkey, *The Phenomena of Fluid Motions* (Addison-Wesley, Reading, Massachusetts, 1969).

35. K. Bergeles, G. Charalampous, Y. Hardalupas, and A. M. Taylor, "Effect of Liquid Viscosity on the Aerodynamic Breakup of Non-Spherical Droplets," *28th Conference on Liquid Atomization and Spray Systems, DOI:10.4995/ILASS2017.2017.4675* (2017).

36. A.Hess, D. Kessler, R. Johnson, C. A. Munoz, J. Sosa, and G. Goodwin, "Evaluation of Droplet Aerodynamic Breakup Models in Supersonic and Hypersonic Flows," *AIAA Scitech 2021 Forum,DOI: 10.2514/6.2021-0751* (2021).

37. A. Hanson, E. Domich, and H. Adams, "Shock Tube Investigation of the Breakup of Drops by Air Blasts," *The Physics of Fluids* **6**(8), 1070–1080 (1963).

38. D. Joseph, J. Belanger, and G. Beavers, "Breakup of a Liquid Drop Suddenly Exposed to a High-Speed Airstream," *International Journal of Multiphase Flow* **25**, 1263–1303 (1999).

39. J. Nicholson, "Drop Breakup by Airstream Impact," Technical Report RAE N68-19401-427, Farnborough, England, 1967.

40. J. Sinclair and X. Cui, "A Theoretical Approximation of the Shock Standoff Distance for Supersonic Flows around a Circular Cylinder," *Phys. Fluids* **29**(026102) (2017).

41. J. P. Barber, H. R. Taylor, E. S. Grood, and A. K. Hopkins, "Water Drop / Bow Shock Interactions," Progress Report AFML-TR-75-165, Air Force Materials Laboratory, Wright-Patterson Air Force Base, OH, 1975.

42. B. Moylan, B. Landrum, and G. Russel, "Investigation of the Physical Phenomena Associated with Rain Impacts on Supersonic and Hypersonic Flight Vehicles," *Procedia Engineering* **58**, 223–231 (2013).

43. K. Daniel, D. Guildenbecher, P. Delgado, G. White, S. Reardon, H. S. III, and S.J.Beresh, "Drop Interaction with a Conical Shock," *AIAA SciTech Forum 2022, DOI: 10.2514/6.2022-1821* (2022).

44. M. Ibrahim and M. Medraj, "Water Droplet Erosion of Wind Turbine Blades: Mechanics, Testing, Modeling and Future Perspectives," *Materials* **13**(157) (2020).

45. F. Heymann, "On the Time Dependence of the Rate of Erosion Due to Impingement or Cavitation, Number DOI: 10.1520/STP46046S, 1967.

46. G. Springer, *Erosion by Liquid Impact* (Scripta Publishing Company, 1976).

47. O. Gohardani, "Impact of Erosion Testing Aspects on Current and Future Flight Conditions," *Progress in Aerospace Sciences* **47**, 280–303 (2011).

48. G. Beitel, "Development of a Rain/Ice Environment in the AEDC Aerothermal Wind Tunnel," Technical Final Report AEDC-TR-86-8, Arnold Engineering Development Center, Arnold Air Force Station, TN, 1986.

49. D. Jenkins and J. Booker, "The Impingement of Water Drops on a Surface Moving at High Speed," Proceedings of the Proceedings of the Aerodynamic Capture of Particles, Oxford, UK (Pergamon Press), 1960.

50. W. Adler, *The Mechanics of Liquid Impact, Vol.16* (Preece, C.M.,Ed.; Academic Press, Cambridge, MA, 1979).

51. T.Sun, F. Alvarez-Novoa, K. Andrade, P. Gutierrez, L. Gordillo, and X. Cheng, “Stress Distribution and Surface Shock Wave of Drop Impact,” *Nature Communications* **13**(1703) (2022).

52. P. Wegener and L. Mack, “Condensation in Supersonic and Hypersonic Wind Tunnels,” *Advances in Applied Mechanics* **5**, 307–447 (1958).

53. P. Hill, “Condensation of Water Vapour During Supersonic Expansion in Nozzles,” *J. Fluid Mech.* **25**(3), 593–620 (1965).

54. Airgas, “Specialty Gases and Equipment Product Reference Guide, Catalogue Web Version 2018,” 2018. URL `https://www.airgas.com/airgascatalog/catalog/index.html`.

55. W. Collie, “Concept for the Implementation of a Rain/Ice Erosion Capability at AEDC,” Final Technical Report AEDC-TMR-84-V2, Arnold Engineering Development Center, Arnold Air Force Station, TN, 1984.

56. C. Crowe, “Drag Coefficient of Particles in a Rocket Nozzle,” *AIAA Journal* **5**(6), 1021–1022 (1967).

57. E.L.Clark, “Hemisphere-Cylinder Pressure Distributions at Supersonic and Hypersonic Mach Numbers,” Technical Report AEDC-TR-66-179, 1966.

58. C. Henderson, “Drag Coefficients of Spheres in Continuum and Rarefied Flows,” *AIAA Journal* **14**(6), 707–708 (1976).

59. E. Loth, “Compressibility and Rarefaction Effects on Drag of a Spherical Particle,” *AIAA Journal* **46**(9), 2219–2228 (2008).

60. J. Anderson, *Hypersonic and High-Temperature Gas Dynamics* (American Institute of Aeronautics and Astronautics, Inc., Reston, VA, 2006).

61. W. G. Reinecke and G. D. Waldman, “A Study of Drop Breakup Behind Strong Shocks with Applications to Flight,” Technical Final Report SAMSO-TR-70-142, AD871218, Space and Missile Systems Organization, Norton Air Force Base, CA, 1970.

62. M. W. Lee, J. J. Park, M. M. Farid, and S. S. Yoon, “Comparison and correction of the drop breakup models for stochastic dilute spray flow,” *Applied Mathematical Modelling* **36**(9), 4512–4520 (2012).

63. D. Hébert, J. L. Rullier, J. M. Chevalier, I. Bertron, E. Lescoute, F. Virot, and H. El-Rabii, “Investigation of mechanisms leading to water drop breakup at Mach 4.4 and Weber numbers above 10 5,” *SN Applied Sciences* **2**(1), 69 (2020).

64. F. Bartz, D. Guildenbecher, R. Schmehl, R. Koch, H. Bauer, and P. Sojka, “Model comparison for single droplet fragmentation under varying accelerations,” Proceedings of the 24th European conference on liquid atomization and spray systems, 2011.

65. J. C. Beale and R. D. Reitz, “Modeling spray atomization with the Kelvin-Helmholtz/Rayleigh-Taylor hybrid model,” *Atomization and sprays* **9**(6) (1999).

66. D. Stefanitsis, G. Strotos, N. Nikolopoulos, E. Kakaras, and M. Gavaises, “Improved droplet breakup models for spray applications,” *International Journal of Heat and Fluid Flow* **76**, 274–286 (2019).

67. L. P. Hsiang and G. Faeth, “Drop deformation and breakup due to shock wave and steady disturbances,” *International Journal of Multiphase Flow* **21**(4), 545–560 (1995).

68. L. Forney, D. Van Dyke, and W. McGregor, "Dynamics of particle—shock interactions: part I: similitude," *Aerosol science and technology* **6**(2), 129–141 (1987).

69. T. Theofanous, G. Li, T. N. Dinh, and C. H. Chang, "Aerobreakup in disturbed subsonic and supersonic flow fields," *Journal of Fluid Mechanics* **593**, 131–170 (2007).

70. R. Schmehl, "Advanced modeling of droplet deformation and breakup for CFD analysis of mixture preparation," *Zaragoza* **9**(11) (2002).

71. C. Wilke, "A viscosity equation for gas mixtures," *Journal of Chemical Physics* **19**, 517–519 (1950).

72. S. Mathur, P. Tondon, and S. Saxena, "Thermal conductivity of binary, ternary and quaternary mixtures of rare gases," *Molecular Physics* **12**, 569–579 (1967).

73. R. Kee, F. Rupley, and J. Miller, "Chemkin-ii: A Fortran chemical kinetics package for the analysis of gas-phase chemical kinetics.

74. H. Wiegand, "Die Einwirkung eines ebenen Strömungsfeldes auf frei bewegliche Tropfen und ihren Widerstandsbeiwert im Reynoldszahlbereich von 50 bis 2000," *Forschung im Ingenieurwesen* **54**(6) (1988).

75. P. O'Rourke and A. Amsden, "The Tab Method for Numerical Calculation of Spray Droplet Breakup," *SAE Technical Paper* **872089** (1987).

76. R. Reitz, "Modeling atomization processes in high-presure vaporization sprays," *Atomization and Spray Technology* **3**, 309–337 (1987).

77. T. Su, M. Patterson, R. D. Reitz, and P. Farrell, "Experimental and numerical studies of high pressure multiple injection sprays," *SAE transactions* pp. 1281–1292 (1996).

78. R. S. Miller, K. Harstad, and J. Bellan, "Evaluation of equilibrium and non-equilibrium evaporation models for many-droplet gas-liquid flow simulations," *International Journal of Multiphase Flow* **24**, 1025–1055 (1998).

79. R. Hartmann and T. Leicht, "Higher order and adaptive DG methods for compressible flows," in H. Deconinck, ed., *VKI LS 2014-03: 37th Advanced VKI CFD Lecture Series: Recent developments in higher order methods and industrial application in aeronautics, Dec. 9-12, 2013*, pp. 1–156 (Von Karman Institute for Fluid Dynamics, Rhode Saint Genèse, Belgium, 2014).

80. J. Burr, *Fundamental Study of Detonation Structure in Rotating Detonation Engine*, Phd dissertation (University of Maryland, College Park, 2020).

81. The OpenFOAM Foundation, "OpenFOAM," 2022. URL `https://openfoam.org`.

82. J. C. Meng and T. Colonius, "Numerical simulation of the aerobreakup of a water droplet," *Journal of Fluid Mechanics* **835**, 1108–1135 (2018).

83. A. Hess, D. A. Kessler, R. F. Johnson, C. Aguilera, J. Sosa, and G. B. Goodwin, "Evaluation of Droplet Aerodynamic Breakup Models in Supersonic and Hypersonic Flows," Proceedings of the AIAA Scitech 2021 Forum, 2021, p. 0751.

84. J. Sinclair and X. Cui, "A theoretical approximation of the shock standoff distance for supersonic flows around a circular cylinder," *Physics of Fluids* **29**(2), 026102 (2017).